ABSTRACT

CHAPMAN, EDWARD MICHAEL: Efficiency and Function: Design and Analysis of Smart Actuators and Systems using Fluidic Artificial Muscles (Under the direction of Dr. Matthew Bryant).

This work is comprised of three distinct contributions to the literature in the modeling and analysis of fluidic artificial muscles (FAMs) and systems which utilize them. First, a fully-coupled electrohydraulic system with single FAMs is used to study design parameter effects on the efficiency of a quadrupedal climbing robot. Its results indicate that increased actuator efficiency does not necessarily lead to increased system efficiency. This indicates that it is necessary to consider the FAM as well as the whole system must both be considered in order to optimize system efficiency. Secondly, the work explores the biomimicry of FAMs by presenting a novel way of controlling the activation of multiple FAM's in parallel 'bundles.' It does so by taking advantage of elastic nonlinearities in FAM bladders to control the pressure at which a specific FAM is recruited; called 'threshold pressure.' Placing multiple FAMs with different threshold pressure under the control of a single throttle valve recruits some muscles before others. This is dubbed passive variable recruitment and is inspired by Henneman's size principle, which governs the activation of mammalian muscle. The study indicates that activating FAMs in this way is advantageous in variable output systems which operate primarily in low-load, low-stroke regimes but require occasional outputs of large stroke and/or force. Lastly, the work explores multiple fully coupled electro-hydraulic systems and addresses the design considerations for increased performance and efficiency of both variable recruitment bundles and a single FAM. We propose an analytic model for predicting the upper-limit of performance of a given FAM bundle recruitment level as a function of load, FAM design parameters, and motor and pump operating characteristics.

Efficiency and Function: Design and Analysis of Smart Actuators and Systems using Fluidic Artificial Muscles

by
Edward Michael Chapman

A dissertation submitted to the Graduate Faculty of
North Carolina State University
in partial fulfillment of the
requirements for the degree of
Doctor of Philosophy

Mechanical Engineering

Raleigh, North Carolina
2018

APPROVED BY:

Dr. Matthew Bryant Chair of Advisory Committee	Dr. Katherine Saul
Dr. Lawrence Silverberg	Dr. Michael Daniele

DEDICATION

To my nephew, Wyatt Thomas Chapman, for whose generation the efforts of scientists and engineers work to understand, preserve, and improve the world. Seek you and you will find.

BIOGRAPHY

Edward M. (Ted) Chapman was born in Charleston South Carolina and grew up in Palm Harbor Florida. Upon graduation from Palm Harbor University High School, he attended and graduated from Clemson University in 2008 with his B.S. in Mechanical Engineering. He subsequently attended Navy Officer Candidate School and was commissioned as an ensign in the Navy in September 2008. He served as Communications Officer aboard USS THE SULLIVANS (DDG 68) through two deployments before attending Nuclear Power School in Charleston, SC. Upon completion of Nuclear Power School, he qualified as Engineering Officer of the Watch at Nuclear Power Training Unit in Ballston Spa, NY. He then served aboard USS THEODORE ROOSEVELT (CVN 71) as Main Propulsion Division Officer, qualifying first Propulsion Plant Watch Officer and then Nuclear Engineer. He continued aboard CVN 71 as Assistant Reactor Electrical Assistant before separating from active duty service in 2014 to begin his PhD studies.

He began his graduate studies at North Carolina State University in the department of Mechanical and Aerospace Engineering as part of the direct-track PhD program in August of 2014. He received his en-route M.S. in Mechanical Engineering in August of 2017. He will complete the requirements for his PhD in Mechanical Engineering at NCSU in June 2018.

ACKNOWLEDGMENTS

I would like to thank my brother, Rick for his thoughtful encouragement as I've worked to finish the requirements of this degree. His motivational attitude and enthusiastic and measured support has been integral to my success. And also my parents, whose thoughts were with me throughout this process and whose support has always been steadfast.

I would also like to extend my thanks to Dr. Matthew Bryant, my advisor. His efforts to shape a naval officer and nuclear operator into a research engineer required a great deal of patience and I would not be in the position to author this work without his guidance and support. Lastly, I would like to thank all the members of my committee, but in particular Dr. Katherine Saul, who's support, expertise, and guidance helped foster the motivation for and biological underpinnings of much of this work.

TABLE OF CONTENTS

LIST OF TABLES

LIST OF FIGURES

CHAPTER I

Introduction

a) FAM background and history

Fluidic Artificial Muscles (FAMs) have received a great deal of attention in recent studies. Their existence dates to the 1950's when Joseph McKibben was inspired to give increased mobility to his daughter, who had been paralyzed by polio, and developed a 'muscle' actuated by compressed carbon dioxide [1], [2]. McKibben's original muscle and custom built control valve system included only a 'pressurized' and a 'vent' control scheme but was effective in allowing patients to accomplish small tasks, like holding a pen, despite their paralysis. FAM's are biologically inspired and bear many similarities to mammalian muscles; they are single acting and require antagonistic pairing to induce bi-directionality in force application. They respond to external activation (i.e. fluid pressure) by producing radial expansion and axial contraction and are capable of generating a wide variance of force profiles depending upon the loading, activation pressure applied, and specific construction.

Recent studies experimentally characterized FAM contraction behavior and showed that FAM force-strain production can be likened to variable stiffness springs [3]. Meller, et al. and Tondu expanded upon this theory with analytic models and generated improved force-strain relationships by including experimentally derived correction factors for maximum strain, blocked force, friction, and elastic correction models [2],[4]. Bryant, et al. performed studies on the efficiency and actuation force of variably recruited FAM 'bundles' and showed that more uniform and higher efficiencies could be induced by utilizing FAMs of various sizes aligned in parallel groups and only actuating the muscles needed for a specific force-strain regime [5]. Robinson, et al. utilized a single degree of freedom robot arm actuated by a bundle of six FAMs to perform a study on selecting the number of pneumatic FAMs which would deliver the highest efficiency for various loading scenarios [6]. Meller, et al. and Tiwari, et al. demonstrated both the feasibility of using hydraulic FAMs rather than the traditionally used pneumatic FAMs and compared them in force output and efficiency to similarly sized pneumatic FAMs and traditional hydraulic pistons. Their results support the large force-to-weight ratio and efficiency advantage that hydraulic FAMs have over the traditional hydraulic piston [7],[4], especially when grouped as bundles, enabling a wider range of use within the force-strain space.

b) Research Aims.

This work is separated into 3 main sections which each address a previously unconsidered area of fluidic artificial muscle research. Chapter II explores a system-level analysis of a climbing robot which utilizes single-acting FAMs and explores the effect of various design parameters on the total system efficiency. Chapter III uses a thin-walled elastic bladder model to explore the feasibility of using FAM elastic nonlinearities as part of a simplified control methodology inspired by mammalian muscle orderly recruitment. Lastly, chapter IV compares recruitment methodologies, and electrohydraulic operating strategies to determine how they dictate the efficiency and function of the electro-hydraulic system used to provide the motive force of actuation.

c) Idealized FAM modeling

Idealized FAM models begin by considering the virtual work model and setting

$$PdV = Fdx \tag{1}$$

Where P is the pressure applied to the muscle, F is the tensile actuation force applied by the muscle, dV is the change in muscle volume and dx is the linear change in location along the muscle's axis of action. The geometry of the idealized muscle has been well established by

Tondu, et al. [2] and others and yields a relationship between axial contraction, radial expansion, and the angle of the braid fibers from the longitudinal axis. This geometric relationship is developed as

$$\frac{L}{L_0} = \frac{\cos\alpha}{\cos\alpha_0} \text{, and} \tag{2}$$

$$\frac{R}{R_0} = \frac{\sin\alpha}{\sin\alpha_0} \tag{3}$$

where L and R are the length and braid radius of the muscle, α is the braid angle of the braided sheath, and their initial values from construction are designated as L_0, R_0, *and* α_0. By performing a series of trigonometric substitutions for the volume of a cylinder, the volume of a muscle, V_m, in terms only of strain, ε, and initial construction characteristics is shown to be

$$V_m = \pi L_0 R_0{}^2 \frac{(1-\varepsilon)-(1-\varepsilon)^3\cos^2\alpha_0}{\sin^2\alpha_0} \tag{4}$$

The change in volume during contraction with respect to a change strain is shown to be

$$\frac{dV_m}{d\varepsilon} = \pi L_o R_0{}^2 \frac{-1+3(1-\varepsilon)^2\cos^2\alpha_0}{\sin^2\alpha_0} \tag{5}$$

Further substitution and defining strain as $\varepsilon = \frac{x}{L_0}$, where x is the change in length of the FAM and (also referred to as stroke) yields an idealized individual muscle force model of

$$F_{m,ideal} = P_{app}\pi R_0{}^2\left[a\left(1-\frac{x}{L_0}\right)^2 - b\right] \tag{6}$$

where P_{app} is applied pressure and

$$a = \frac{3}{tan^2\alpha_0} \text{, and} \tag{7}$$

$$b = \frac{1}{sin^2\alpha_0} \quad . \tag{8}$$

This idealized model is effective at predicting blocked force, especially at higher pressures, but is generally poor at predicting free strain. Each chapter following will explore different FAM models—chapter II uses an empirical model with predictive modification calculating braid frication, chapters III and IV apply a predictive elastic-nonlinearity model for total system predictability.

CHAPTER II

Fully Coupled Electrohydraulic Model of a Climbing Robot: The Effect of FAM Design Parameters on System Operation (Published (2017) in *Bioinspiration and Biomimetics)*

a) Climbing robot background

In order to gain a system-level understanding of FAMs and their interaction with the electrohydraulic pressure generation system, a biologically inspired, four legged, FAM-actuated climbing robot is considered. Climbing robots are testing-ground platforms for new technologies in actuation, gait control, foot adhesion, and efficiency analysis. Actuator studies have been performed in robots of various sizes. Large-scale climbing robots like *NINJA* and *NINJA II* demonstrated the feasibility and effectiveness of high-powered hydraulic actuators—requiring tethers to ensure continuity of power and required precision hydraulic alignments during construction [8]**.** DC motor actuators have been effective on smaller climbing robots like *ROCR* [9], which has limited payload capability. Smaller still, the gecko inspired robots, *Rigid Gecko Robot (RGR)* also uses DC Servo-motors while its counterpart, the *Compliant Gecko Robot (CGR)* uses shape memory alloys as actuators [10]. Other climbing robot studies focus on gait analysis and locomotion methods rather than system efficiency and longevity of operation [11]. *Climbot*, for example, makes use of a variable degree of freedom gate strategy analyses with antagonistic pairing of "rubbertuators" to enact a non-planar gait in an inspection robot. *Robug* focuses on the control-algorithm driving its gait and foot-adhesion techniques with its pneumatic legs [12, 13]. Still other climbing robots focus almost exclusively on foot-adhesion techniques: the *CLIBO* design uses a 4 DOF DC-motor-driven robot for analysis of a gripping method toward maintaining a stable position for a prolonged period [14]. These climbing robots have been at the forefront of actuator, gait, and adhesion analysis and have set the stage for efficiency analyses, but traditional

DC motor robotic actuators are at a disadvantage when compared to FAMs due to increased weight, alignment criteria, and large variations in electrical power consumption during operation [2]. Furthermore, hydraulic piston-cylinder assemblies are heavier per force output than FAMs, sensitive to alignment, and make use of sliding seals which are prone to leak or degradation [7]. In addition to their high force output and light weight construction, FAMs also offer a smooth, naturalistic motion that is well suited to bio-inspired legged robot architectures.

Previous studies have focused on the operation, control, and efficiency of the FAMs individually, in groups, and even in antagonistic pairs, but in isolation from the system which generates the pressure utilized by the muscles [15]. The purpose of this study is to determine how various FAM and system components affect the efficiency and effectiveness of the system's operation. It will do so by generating a fully coupled electro-hydraulic model of a climbing robot with FAM actuators, validating this model against data from a climbing robot of like-design, and using the model to study the effect of design and operating parameters on system efficiency and velocity of the robot.

b) System Overview

A simple, bio-inspired climbing robot is considered. In this robot concept, a DC motor operating with a prescribed applied voltage drives a constant volume positive displacement pump to form the hydraulic power source. The pump pressurizes a gas-charged accumulator which is connected to a network of valves directing fluid to the artificial muscle actuators. The FAMs are used as linear tensile actuators to drive the limbs of the robot. Each limb and FAM actuator pair is assumed to have identical parameters, including a kinematic relationship described in section 2.1. The robot considered is shown in figure 1 and the hydraulic system considered is shown in figure 2 and is discussed in section 2.2. A complete description of the proof-of-concept climbing robot, its construction, and hardware components can be found in Bryant, et al.[16].

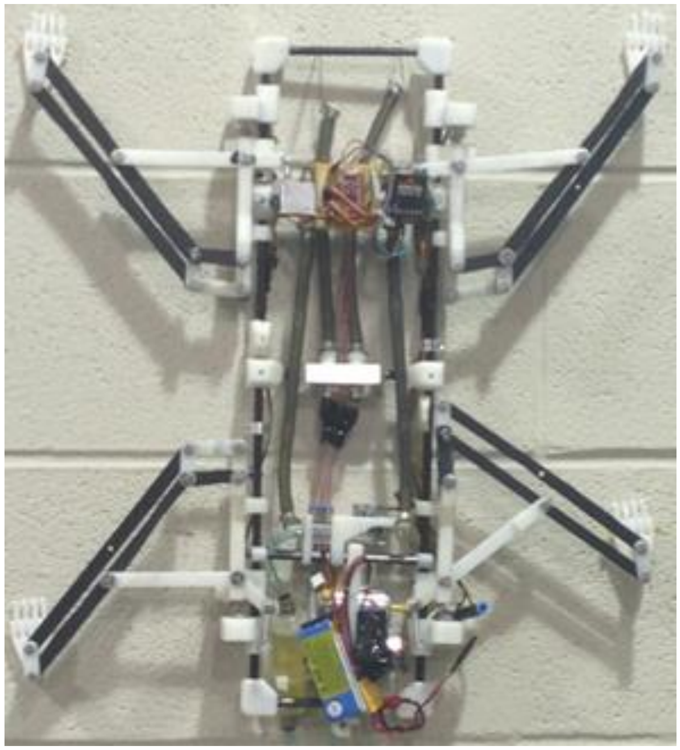

Figure 1: Proof-of-concept prototype climbing robot with onboard hydraulic system and FAM actuators gripping a vertical wall.

The FAMs provide single acting tensile actuation and therefore a linear return spring is included to extend the muscle and leg during depressurization. The robot performs climbing locomotion by making use of claws, which are modeled as a no-slip condition on the vertical wall. During climbing the appropriate FAMs are inflated with working fluid from the accumulator. The actuators then contract, moving the robot vertically while the un-activated muscles are vented and allowed to extend from the force applied by the return springs. In order to fully understand the electrohydraulic coupling to the mechanical operation of the climbing robot, this study begins by modeling the FAM force production and continues with the hydraulic actuation system. This is followed by an analysis of the pump-motor combination and a dynamic model of the motion of the robot itself.

i. FAM subsystem

First, an accurate model of FAM force-contraction behavior is applied to the system under study. The most basic fluidic artificial muscle models were discussed previously and ignore losses and assume constant surface area and a during bladder inflation while maintaining a cylindrical shape. Later studies have generated correction-factors which address energetic losses in the form of friction, elasticity, and non-cylindrical shape near the tips of the muscle. The model employed here includes empirically-determined correction factors to address these construction-associated losses. We express the muscle force-contraction model in terms of the contraction, *x*, rather than the more typical nondimensional strain, ε, by making the substitution, $\varepsilon = \frac{x}{l_0}$ where l_o is the initial muscle length. The key performance-driving parameters of fluidic artificial muscles are the initial braid angle, α_o, initial braid radius, r_o, and applied pressure by the working fluid, P_{app}. FAM output force, F_m initially proposed by Tondu [17] and is fully developed and tested by Meller, et al. [4] as

$$F_m = P_{app} \pi r_0^{\,2} \kappa_F \left[a \left(1 - \kappa_\varepsilon \frac{x}{l_0} \right)^2 - b \right] \quad (9)$$

$$\kappa_F = \frac{F_{meas,\,max}}{\left(\pi r_0^{\,2}\right) P_{app} \left(a - b\right)} \quad (10)$$

$$\kappa_\varepsilon = \frac{1}{\varepsilon_{meas,\,max}} \left[1 - \frac{1}{\sqrt{3}\cos\left(\alpha_0\right)} \right] \quad (11)$$

where, κ_F and κ_ε are the experimentally determined blocked force and free-strain correction factors, respectively. $F_{meas,\,max}$ and $\varepsilon_{meas,\max}$ are the maximum measured blocked force and free strain for a given pressure application. These correction factors are determined for a specific muscle and act to correct differences between calculated and observed force characteristics, largely from inherent elastic bladder effects in the FAM contraction. In this study, the correction factors were determined for the muscles from the experimental climbing robot at system pressure and have values shown in table 3. The model is predicated on the assumption that FAMs retain an approximately cylindrical shape during their quasi-static contraction, and the correction factors help correct for the portions near the tips of the FAMs which do not maintain that shape.

Tondu expanded upon his original modeling by generating a braid on braid frictional force, which accounts for both static and kinetic friction [17]. This frictional force is represented as

$$F_{fric} = (f)(1/\eta)S_{con}P_{app}(sgn(\dot{x})) \tag{12}$$

where $\dot{x}$ is muscle contraction rate, and f is the total dry friction coefficient and is determined by

$$f = f_k + (f_s - f_k)e^{-\dot{x}/\dot{x}_s} \tag{13}$$

with f_s and f_k being the static and kinetic friction coefficients of the braid material, $\dot{x}_s$ is a material based velocity constant, and $1/\eta$ is the estimated ratio of the muscle's lateral self-surface contact. S_{con} is the braid-to-braid surface area of contact, and is defined as [17]

$$S_{con} = \left(2\pi r_o l_o\right)\frac{\sin\alpha_o}{\sqrt{1-\cos^2\alpha_o\left(1-\left(\frac{x}{l_o}\right)\right)^2}}\left(\frac{1}{1-\frac{x}{l_o}}\right) \tag{14}$$

We combine the force and strain correction factors with the frictional loading parameters in order to capture both bladder elasticity and friction effects, yielding an output force model which takes into account the primary loss criteria for FAMs.

ii. Hydraulic subsystem

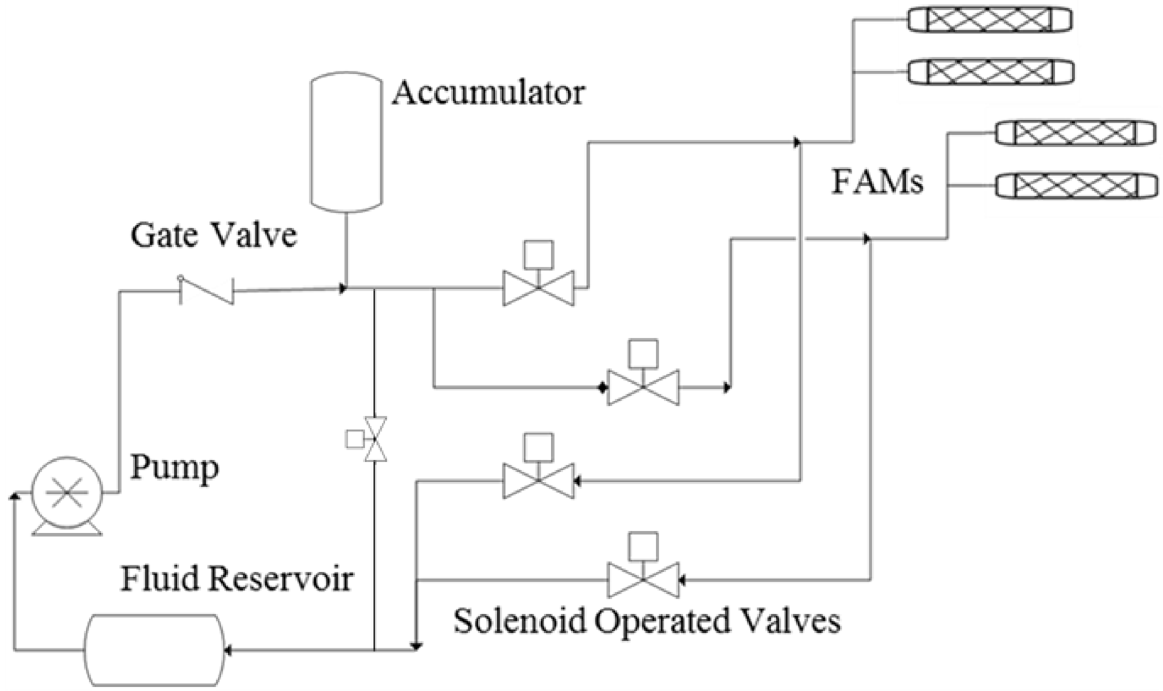

Figure 2: Hydraulic subsystem schematic.

Upon modeling of the FAM contraction characteristics, it is next necessary to couple this contraction with the hydraulic-actuation power-source. The hydraulic system considered is shown in figure 2**.** The system diagram shows four muscles grouped into two pairs; each muscle actuates a single leg on the climbing robot with two legs moving simultaneously for each step. The working fluid analyzed is water due to its relative incompressibility and its compatibility with the system components. A series of equations describing the fluid flow through the system are developed. The fluid volume consumption and rate of consumption of the FAMs during contraction are of foremost importance. The fluid volume consumption as a function of length by an actuated FAM, V_m, is developed by Tondu as

$$V_m = \pi r_0^{\,2} l_0 \left[\frac{\left(1 - \frac{x}{l_0}\right)}{\sin^2 \alpha_0} - \frac{\left(1 - \frac{x}{l_0}\right)^3}{\tan^2 \alpha_0} - 1 \right] \tag{15}$$

The chain rule is utilized on equation (9) to determine the time rate of change of the volume consumption, $\dot{V}_m$ as

$$\dot{V}_m = \pi r_0^{\,2} l_0 \left[\frac{\left(-\frac{1}{l_0}\right)}{\sin^2 \alpha_0} + \frac{3\left(\frac{1}{l_0}\right)\left(1 - \frac{x}{l_0}\right)^2}{\tan^2 \alpha_0} \right] \dot{x} \tag{16}$$

where $\dot{x}$ is the time rate of contraction. In order to determine the pressure drop in the accumulator due to muscle contraction, we relate the gas volume change in the gas-charged accumulator to the volume consumed by the muscles and the fluid added by the positive displacement pump, yielding

$$P_{acc} = \frac{P_{acc,initial} V_{acc,initial}}{V_{acc,initial} + V_m - V_p} \tag{17}$$

by use of the ideal gas law with a constant temperature approximation, where P_{acc} is accumulator pressure and V_p is the volume added to the accumulator by the pump. There is a conditionally opened bypass valve which maintains operating pressure at or below initial system operating pressure. The pressure transmitted by the accumulator to the muscle is similarly derived using first principles, resulting in

$$P_{app} = P_{acc} + \frac{\rho}{2}\left[\left(\frac{\dot{V}_m - \dot{V}_p}{A_{acc}} \right)^2 - \left(\frac{\dot{V}_m}{A_{m,inlet}} \right)^2 \right] - h_l \tag{18}$$

where $\dot{V}_p$ is pump flowrate, $A_{m,inlet}$ is the cross sectional areas of the muscle inlet— defined to be the initial cross sectional area of the FAM, and A_{acc} is the cross sectional area of the accumulator. Pipe losses are modeled as

$$h_L = k_{fl} \frac{\left(\frac{\dot{V}_m}{A_{m,inlet}}\right)^2}{2g} \tag{19}$$

where k_{fl} is the pipe fluid friction coefficient, based on a combination of the fittings and piping used and result in less than a 1% loss in pressure from the accumulator to applied to the muscle.

iii. Electrical subsystem

The hydraulic system pressure is created and maintained by a constant-volume positive displacement pump with displacement, *D*, This pump is driven by a brushed DC-motor with an applied voltage. The hydraulic pump and motor assembly used on the proof-of-concept robot are an off the shelf HP-48030 hydraulic pump and DC motor from HP-Tech [18]. Based on first principles of torque balance and making use of Kirchoff's Voltage Law, the motor-pump rotational acceleration, $\ddot{\theta}$**,** is modeled as

$$\ddot{\theta} = \frac{k_e I - B_m \dot{\theta} - \tau_p - \tau_{fric}}{J} \tag{20}$$

where τ_{fric} is motor friction, *J* is the motor's moment of inertia, k_e is motor's torque constant**,** and B_m is frictional damping coefficient. The rate of change of current, $\dot{I}$ **,** can be shown to be

$$\dot{I} = \frac{V_{motor} - k_b - IR}{L} \tag{21}$$

where k_b is back electro-magnetic force constant, *L* is motor inductance [19], and motor-pump impeller torque, τ_p, is described by

$$\tau_p = \frac{P_{acc} D}{2\pi} \quad (22)$$

As shown in table 1, current and motor speed are set to be initially zero (open circuit) and allowed to adjust as required to meet the other system inputs after a switch is closed at *t=0*.

Table 1. Initial conditions of key electrical parameters

Parameter	Initial Value
I(A)	0
$\dot{\theta}$ (rad/s)	0

iv. Climbing dynamics

A Hoeken-linkage leg mechanism is selected for the study due to its ability to translate rotational movement about a revolute joint into linear motion of the end effector, allowing for a linear climbing stroke with a single degree of freedom at each leg [20] . The robot is moved by four Hoeken-linkage legs operated in pairs and assuming negligible leg mass compared to the overall robot mass.

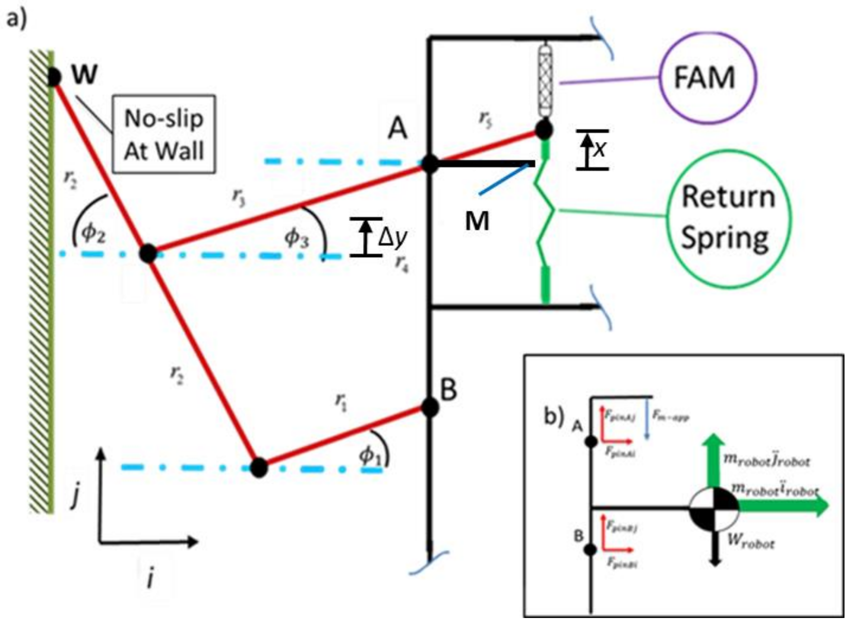

Figure 3: a) Hoeken linkage leg design schematic of upper left leg. A and B are pin-joints connecting leg linkage to robot body, M is a mechanical stop, point W is claw rotational joint at the wall b) Free Body diagram showing the applied and reaction forces along with the inertial response of the robot for the upper left quarter.

Figure 3 shows the leg mechanism, including FAM and return spring connections along with relevant kinematic labels. In order to avoid nomenclature conflicts during the climbing movement analysis, movement along the horizontal axis is labeled in figure 3 as *i* and movement along the vertical axis is similarly labeled as *j*. Linkages r_1-r_5 were selected to have lengths such that linearity was optimized [16, 20] and angles ϕ_1-ϕ_3 change based on the contraction of the FAM. We relate muscle contraction, *x*, to the robot body by

$$x = \mathrm{r}_5 \sin\phi_3 . \tag{23}$$

The position of the robot, *y*, measured at point A relative to the no-slip condition assumed at the claw-to-wall connection point, W, is

$$y = \mathrm{r}_3 \sin\phi_3 - r_2 \sin\phi_2 . \tag{24}$$

Since the system has a single degree of freedom, performing a loop closure analysis allows the use of

$$r_1^2 = r_3^2 + r_2^2 + \mathrm{r}_4^2 + 2r_3r_2(\sin\phi_3\sin\phi_2 - cos\phi_3\cos\phi_2) - 2r_3r_4\sin\phi_3 - 2r_2\,\mathrm{r}_4\sin\phi_2 \tag{25}$$

to relate ϕ_2 **to** ϕ_3**.** At the beginning of each step, link r_3 is horizontal and angle ϕ_3 is zero. The applied muscle force to the system acts vertically and is calculated as

$$F_{m-app} = F_m - F_{spring} - F_{fric} + T \tag{26}$$

where tension, T, represents the force from a mechanical stop that prevents upward leg extension beyond the $\phi_3 = 0$ position. It is defined such that when $F_m - F_{spring} - F_{fric} = 0$, $m_{robot}\ddot{j}_{robot} = 0$. It ensures that mathematically, FAM length never extends beyond l_o and allows the robot to maintain static equilibrium even when applied pressure is zero. The spring is a linear return-spring and has a force of $F_{spring}=0$ at $x=0$. The return spring is never compressed, and the value of x is never negative. In order to relate the applied end-effector forces to the rotational torque about point W, we use the Jacobian analysis of the linkage system [19], defined as

$$J_{W-A} = \begin{bmatrix} \dfrac{\partial i_A}{\partial\phi_2} & \dfrac{\partial i_A}{\partial\phi_3} \\ \dfrac{\partial j_A}{\partial\phi_2} & \dfrac{\partial j_A}{\partial\phi_3} \end{bmatrix} \tag{27}$$

where J_{W-A} is the Jacobian relating translational motion of the pin-joint at point A to the rotational motion about the joint robot's claw at W. $\frac{\partial i_A}{\partial\phi_2}$ is the partial derivative of the horizontal motion of point A with respect to ϕ_2, while $\frac{\partial j_A}{\partial\phi_2}$ is the partial derivative of the vertical motion of point A with respect to ϕ_2. While the movement of point ***A*** is dependent on ϕ_3 as well as ϕ_2**,** by equation (19**)**, we have $\phi_3 = f(\phi_2)$ and, therefore equation (21) can be expressed as

$$J_{W-A} = \begin{bmatrix} \dfrac{\partial i_A}{\partial \phi_2} \\ \dfrac{\partial j_A}{\partial \phi_2} \end{bmatrix} \tag{28}$$

J_{W-B} is similarly constructed for pin-joint B and J_{W-M} for the point of muscle attachment. We apply the virtual work [19] model for Jacobian analysis to show that

$$\tau_{W-A} = J_{W-A}^T F_{pinA} \tag{29}$$

where τ_{W-A} is the torque about the wall-joint at the robot claw induced from the pin-reaction force, J_{W-A}^T is the transpose of the Jacobian from pin A to the wall joint, and F_{pinAj} is the vertical pin reaction force at point A. This process is repeated using the vertical force at the other leg-body pin joint, F_{pinBj} to find τ_{W-B}, applied muscle force, $F_{m\text{-}app}$ to find τ_{W-M}, and W_{robot} to find τ_{W-R}, the torque from the robot's weight at its center of gravity. The equations of motion of the robot can be written as

$$I_W \ddot{\phi}_2 = \tau_{W-A} + \tau_{W-B} + \tau_{W-M} + \tau_{W-R} \tag{30}$$

$$m_{robot} \ddot{i}_{robot} = (F_{pinAi} + F_{pinBi})_L + (F_{pinAi} + F_{pinBi})_R \tag{31}$$

and

$$m_{robot} \ddot{j}_{robot} = F_{pinAj} + F_{pinBj} - F_{m-app} - W_{robot} \tag{32}$$

where I_W is the time-varying moment of inertia of the robot's center of gravity about point W, and horizontal acceleration of the robot, $\ddot{i}_{robot}$, is zero based on the restrictions of the Hoeken linkage assembly, and $(F_{pinAi} + F_{pinBi})_{L/R}$ is the horizontal pin reaction forces from the leg on each side of the climbing robot . This system of equations, along with the coupled FAM contraction formulae give the relationships governing the motion of the robot in terms of muscle force generation as a function of contraction and applied pressure. Initial conditions for this subsystem are shown in table 2.

Table 2. Initial conditions of key climbing subsystem parameters

Parameter	Initial Value
$x(m)$	0
ϕ_3 (rad)	0
F_{spring} (N)	0 (x=0)
j (m)	0

c) Model Validation

The model output is compared to results measured from the climbing robot shown in figure 1. The parameter values for this prototype robot are listed in Table 3. These parameters were directly measured, or, in the case of the motor-pump assembly, provided by the component manufacturer. The experimental results are collected using 2D video motion analysts to measure the position of the robot as a function of time and an onboard ammeter and data logging to record current [16]. Comparison of both operating current and robot motion were found using the system of coupled equations previously listed. Model operating current and robot motion as functions of time were found using the system of coupled equations previously defined.

Table 3. Initial parametric values

Parameter (units)	Baseline
m_{robot} (kg)	1.264
l_o (m)	0.165
r_o (m)	0.003225
α_o (degrees)	30
κ_F	0.97
κ_ε	1.57
P_{app} (kPa)	689
V_{motor}(V)	8
K_{spring} (N/m)	60
D (cm^3/rev)	0.023
V_{acc} (m^3)	3.77e-4

Table 3 (Continued). Initial parametric

No-load speed (RPM)	17000
No-Load Current (A)	0.5
k_f ke (Nm/A)	17.1e-3
k_e (V.sec/radian)	17.1e-3
B_m (Nm/(rad/s))	1.23e-6
J (kg.m^2)	9.45e-7
R (Ohms)	0.45
L (H)	0.112e-3
$V_{acc,I}$ (%)	50

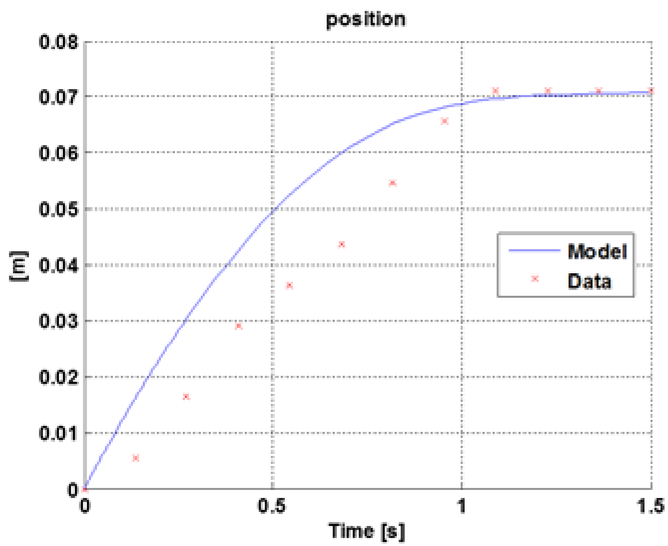

Figure 4: Experimental and model climbing robot movement during one climbing step.

Figure 4 plots the vertical position of the robot during one climbing step (i.e. a single contraction of a leg pair), and shows that the model predicts the positon at the end of the step to within 1.1% of the measured value. This is vitally important to the usability of the model, since the primary measure of the system's energy output is the change in potential energy after a specific number of total steps. The apparent mismatch between the model and the data during this contraction is due to the model-assumed instantaneous valve-opening which allows instantaneous flow into the FAM. Since real valves take some time period to open and allow flow, there is a slight delay in contraction seen in the data. While the intermediate motion is not perfectly aligned, the average velocity between time $t = 0.2$ *seconds* and time $t = 0.8$ *seconds* matches to within 1.5%. The initial and final leg positions are the primary drivers of system output and therefore, the match of 1.1% as seen in figure 4 is sufficient for our analyses. Figure 5 shows a clear overlap of experimental and predicted current draw throughout motor starting operation; the initial current spike, and final steady state operating currents are of particular note. The model is therefore satisfactorily accurate in its prediction of system current draw over time.

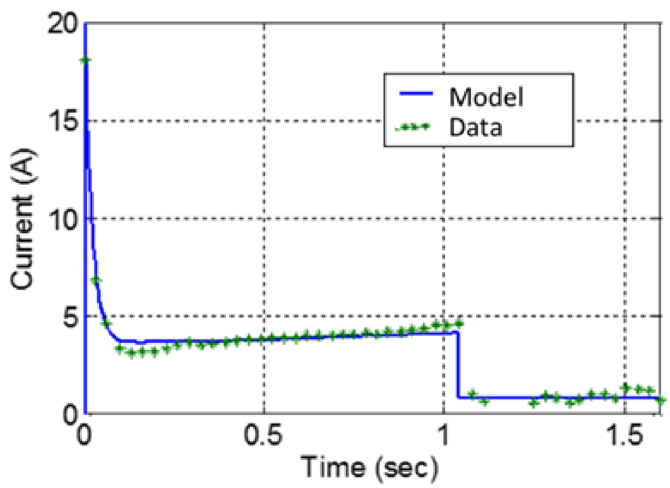

Figure 5: Experimental and model climbing robot current use.

These validation tests demonstrate that the model reasonably captures the mechanical and electrical behavior of a physical meso-hydraulic climbing robot with FAM actuation. It can therefore be used to perform case studies for the purpose of understanding the dependencies of system-level performance metrics like locomotion speed and efficiency on the design and operating parameters of the robot.

d) Simulation of Continuous Climbing Operation

Next, the model is used to analyze the response of the system during continuous climbing. The simulation is started with a zero current condition and is initialized at rest. The system parameter values are set as shown in Table 3. Applied voltage and muscle contraction are enacted at $t=0$ and muscle contraction is allowed to continue until the accumulator has been refilled so that the next step can be performed. The simulation is set to have the robot perform a predetermined number of steps by alternating actuation of leg pairs. The top right and bottom left legs are actuated together as leg pair 1 and the top left and bottom right legs are actuated as leg pair 2. We define system efficiency as the ratio of output work to input energy for the climbing locomotion. Considering locomotion to start from rest and end at rest, the system efficiency is given by

$$\eta_{sys} = \frac{\Delta U_{robot}}{\int P_{motor}\,dt} \tag{33}$$

where instantaneous power input, P_{motor} is calculated as the constant operating voltage multiplied by the instantaneous motor current, and ΔU_{robot} is the change in robot gravitational potential energy following a climbing operation.

The output results for the climbing robot model parameters performing a 3-step climbing sequence are shown in figure 6. As muscle contraction occurs, fluid volume is consumed from the accumulator, resulting in a pressure drop in the accumulator, thereby inducing a motor torque decrease and speed increase. As the pump operates to re-pressurize the accumulator to the prescribed operating pressure, torque increases and motor-speed drops. This speed change directly affects operating current, and therefore power consumption. There is an initial current spike correlating to the startup of the motor; this is followed by smaller current fluctuations during the climbing gait cycle. The position dwells at each step occur due to the mechanical range of motion limitations while the system re-pressurizes the accumulator.

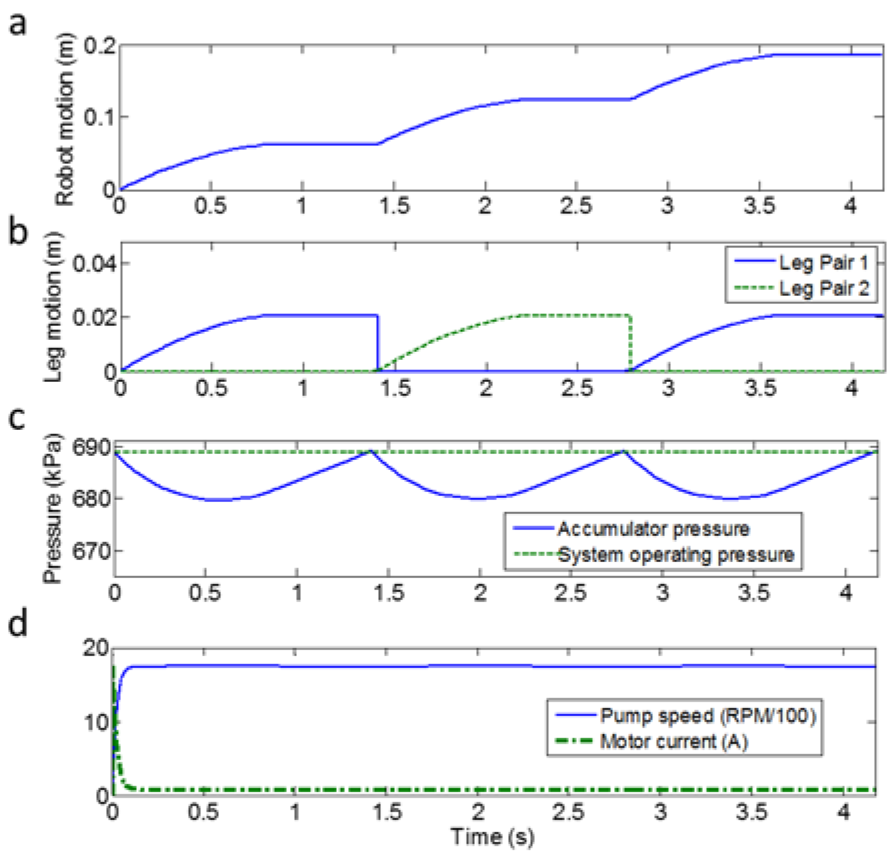

Figure 6: (a) Variation in robot height, (b) Muscle contraction, (c) Accumulator pressure variance from system operating pressure, and (d) Motor speed and current with time for three climbing steps.

After the initial starting current spike, the system operates at a near constant current draw, yielding an improved system efficiency as the duration of operation increases. Figure 7 shows efficiency as a function of the number of steps taken. As the number of steps increases, the starting current of the motor makes up a smaller percentage of the overall energy usage while the output work remains constant per step. This represents an interesting potential advantage of this electrohydraulic actuation scheme for a legged robot. In a more conventional approach using a servomotor at each leg DOF, a starting current spike would be encountered at each step. The hydraulic power system used here, however, allows the single motor to run continuously and distribute power among the legs. The peak efficiency seen for a long operational period of this climbing robot approaches 8.3% for this baseline configuration; the parametric variation studies which follow will bring to light design characteristics which can altered in order to improve this peak efficiency.

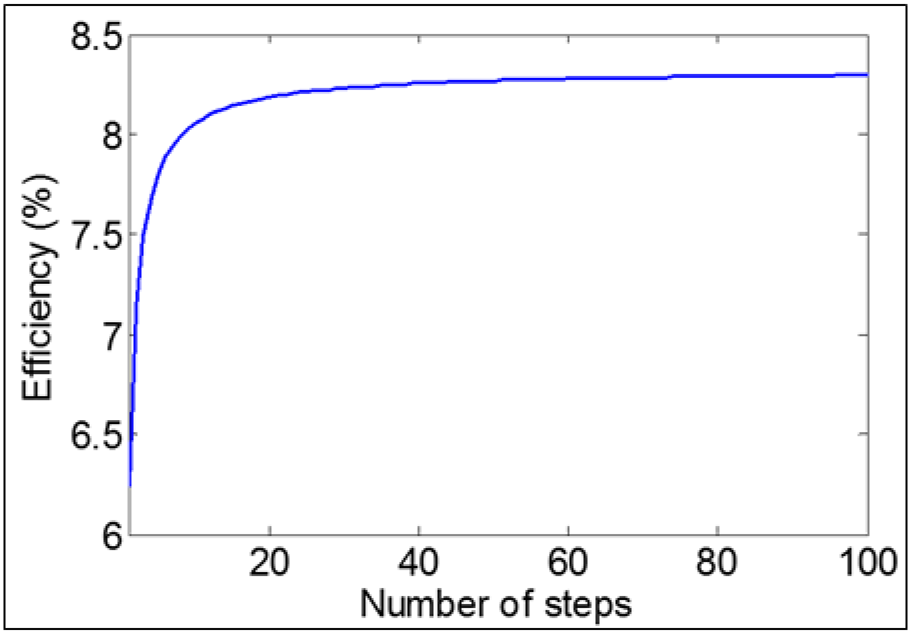

Figure 7: Efficiency as a function of number of steps taken by the climbing robot.

e) Parameter Sensitivity Studies

..............The model is next used to study the effects of various parameters on the electro-hydraulic system performance as defined by average robot velocity and system efficiency. Parameters to be investigated are categorized as either *design parameters*: pump displacement, initial braid angle, and initial braid radius, or *operating parameters*: robot mass, system voltage, and system operating pressure. Values not being varied in a given study were fixed at the values for the baseline climbing robot as shown in Table 3. The parametric sensitivity study is performed by simulating the system across a sweep of design parameter values for several operating parameter cases to reveal the interdependencies of the system configuration

i. Investigation of initial braid angle sensitivity

As a key actuator design characteristic, initial braid angle is swept from 25-40 degrees to determine its effect on system efficiency and velocity. The individual actuator is modeled for these various initial braid angles first to find if there is any deviation between traditional actuator-focused FAM research and the system-level approach performed here.

1) Sensitivity of actuator efficiency to initial braid angle

An actuator-only quasi-static analysis of an idealized FAM (no friction, $\kappa_F = 1$, $\kappa_\varepsilon = 1$) and a real model which includes the empirically-determined frictional losses and correction factors is performed to determine the effect of initial braid angle on the actuator efficiency. Actuator efficiency is defined as

$$\eta_{act} = \frac{\int F_m dx}{\int P dV} \tag{34}$$

where η_{act} is the actuator efficiency, F_m is the muscle force and P is the fluid pressure applied to the muscle. The results, as shown in figure 8, indicate that while an idealized muscle is 100% efficient with any initial braid angle, as initial braid angle increases in a non-ideal FAM, there is a correlating negative effect on both maximum achievable strain and actuator efficiency. These strain and efficiency limitations in comparison to an idealized model are consistent with the experimental results of Meller, et al. [4].

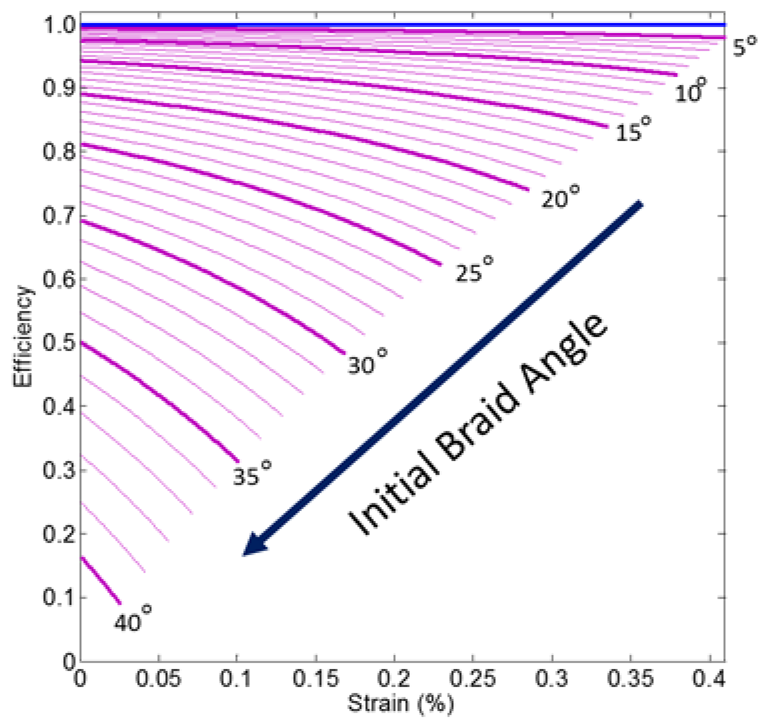

Figure 8: Efficiency as a function of contraction for initial braid angles from 5-40 degrees for ideal muscle model (blue) and non-ideal muscle model (magenta). Curves for non-ideal model results end at the free-strain limit of the given initial braid angle.

2) *Effects of robot mass and initial braid angle on system performance*

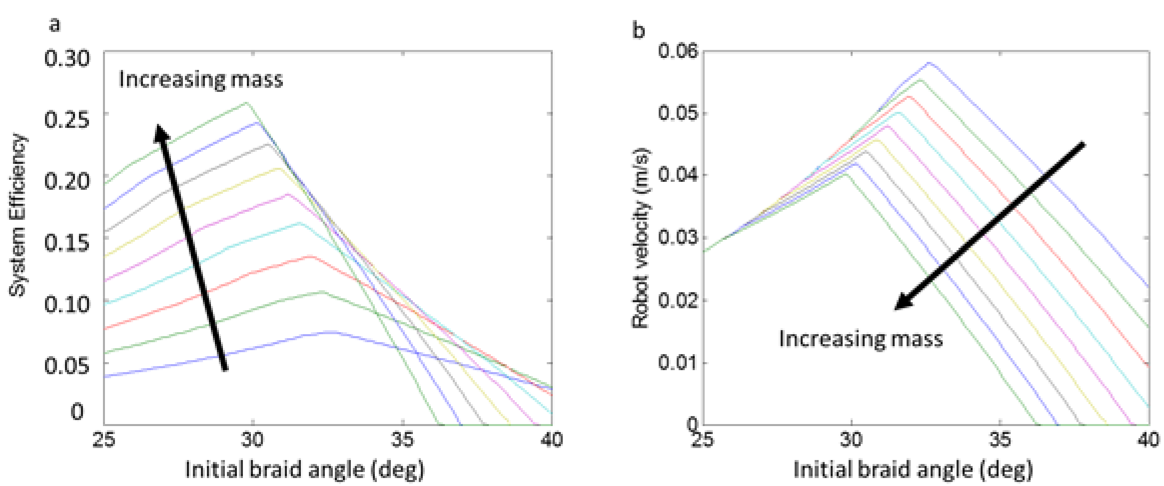

Figure 9: (a) efficiency and (b) velocity as a function of initial braid angle for mass ranging from 1-5kg.

Figure 9 illustrates the significant effect initial braid angle has on both system efficiency and robot velocity. Figure 9(a) shows a distinct peak efficiency value and its corresponding initial braid angle for each robot mass tested. Robot mass affects both the value of this peak and the initial braid angle at which it occurs. For a robot mass of 1kg, the peak efficiency occurs at an initial braid angle of 32.6 degrees while for a robot mass of 5kg, the peak efficiency occurs at 29.8 degrees. As mass increases from 1-5 kg, the system's efficiency also becomes more sensitive to changes in initial braid angle. The increased efficiency for a heavier robot is indicative of an over-powered FAM at a given braid angle. The rapid drop of the 5kg case to 0% efficiency when the initial braid angle is increased to 36.2 degrees is indicative of the initial braid angle being sufficiently large that the muscle underpowered and unable to contract under the robot load, which is predicted by equation (1). As the robot's mass increases, its velocity at all initial braid angles decreases. By comparing the two plots, it is noted that the initial braid angle at which peak velocity and peak efficiency occur is the same point, yielding an important design criterion.

It is interesting to note that while lower initial braid angles increase the peak force output of the actuator, they do not correspond to maximum system efficiency nor maximum robot velocity. To understand this result, we must recognize that peak muscle contraction also is related to initial braid angle. This contraction leads to an increase in volume consumption by the muscle, as shown in equation (9), and lower initial braid angles thus consume more pressurized working fluid. This increased volume consumption causes increased accumulator refill time and therefore larger electrical power consumption and a longer cycle-rate and lower robot velocity. This analysis underscores the importance of considering braid-angle during system design; too small will cause unnecessary fluid consumption and decreased efficiency while too large will cause insufficient force output and lead to a potential for incomplete range of motion, an effect magnified by an increase in system load.

3) Effects of operating pressure and initial braid angle on system performance

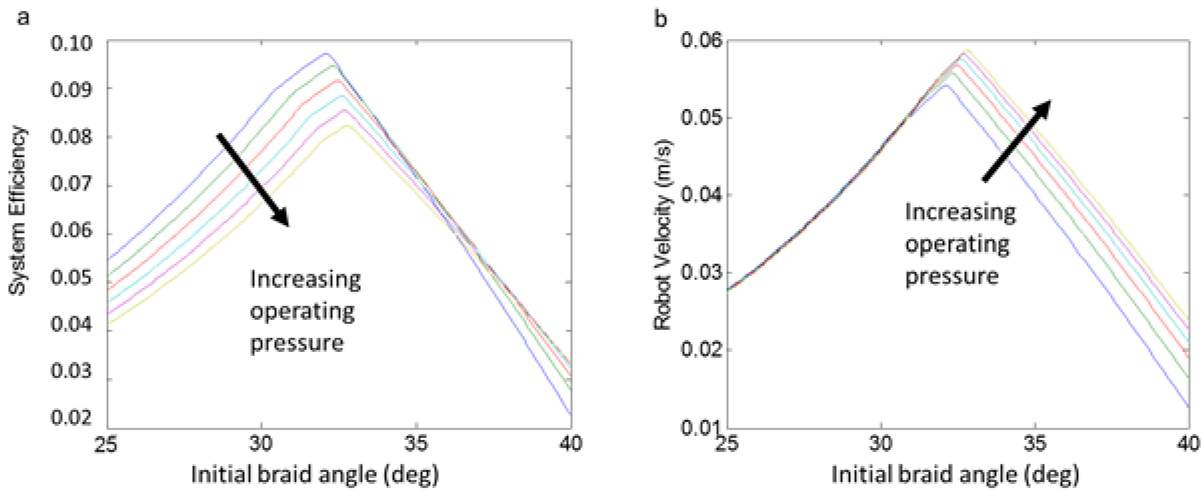

Figure 10: (a) efficiency and (b) velocity as a function of initial braid angle for operating pressures from 500-1000 kPa.

The sensitivities of system efficiency and average velocity for initial braid angles from 25-40 degrees and operating pressures from 500-1000 kPA are shown in figure 10. The results indicate that at each pressure, there is a distinct initial braid angle for which both efficiency and velocity are maximized. At 500 kPa, this optimal initial braid angle is 32.1 degrees and at 1000 kPa it increases to 32.8 degrees. Of interest, as with the mass analysis, is that lower braid angles lead to increased volume consumption and decreased efficiency. Also, at higher braid angles, the FAMs are underpowered, as predicted by equation (1), so while volume consumption is lower, the decrease in energy output of the system—shorter leg strides—dominates the efficiency of the system. This effect can be overcome somewhat by increasing system operating pressure as seen in the efficiency plot overlap at approximately 36 degrees in figure 10(a), but only slightly, since FAM contraction is also limited by braid angle. These results illustrate that an initial braid angle between 32 and 33 degrees yields the best performance over the pressure range tested and that, furthermore, the lowest pressure which will effectively perform the motion should be selected if maximizing efficiency rather than velocity is the goal.

4) Effects of applied voltage and initial braid angle on system performance

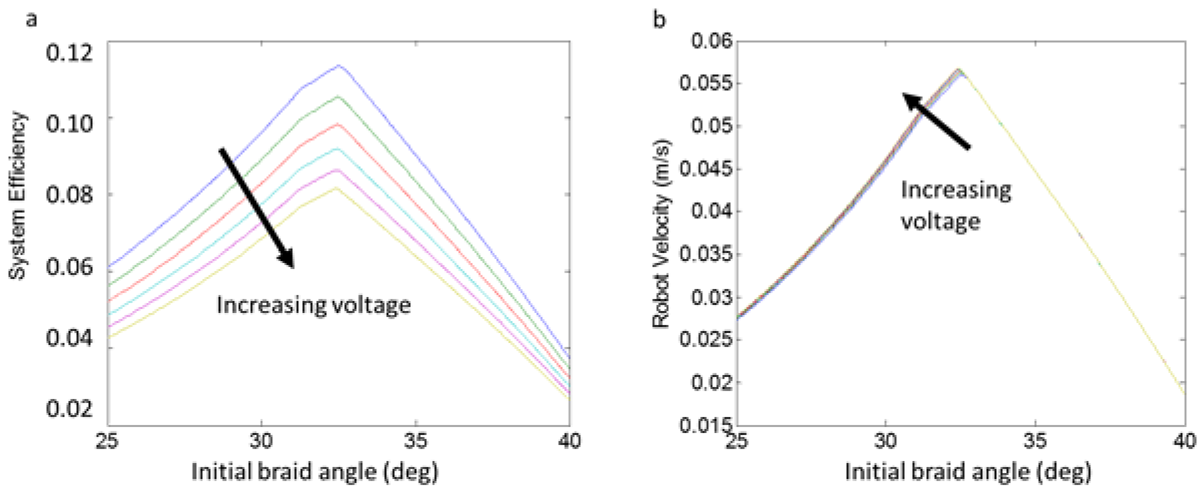

Figure 11: (a) Efficiency and (b) Velocity as a function of initial braid angle for voltages ranging from 5-10 V.

Initial braid angle is swept from 25-40 degrees for applied system voltages of 5-10 V. The results, shown in figure 11, indicate that voltage has a significant effect on efficiency, but little effect on the velocity of the system. Also, unlike both robot mass and system operating pressure, system voltage has almost no effect on the initial braid angle at which peak efficiency occurs. This is because voltage has no direct effect on output force or volume consumption, as indicated in equations (1) and (9)As with both pressure and mass changes, however, the system becomes more sensitive to initial braid angle as voltage is increased. While voltage has a significant effect on efficiency at all initial braid angles, only at lower initial braid angles does the higher voltage result a marginal increase in velocity—due to a lower accumulator refill time. But, as initial braid angle decreases beyond its value for peak efficiency, velocity drops uniformly for all voltages.

Based on this information, when designing an electrohydraulic system for operating in conjunction with FAM's, the lowest operable voltage should be selected.

ii. Investigation of initial braid radius sensitivity

Initial braid radius is another key actuator design characteristic, having an impact on force output, surface area and frictional losses, and volume consumption. We begin with a study of the actuator alone, and then perform a sweep of initial braid radii for analysis with mass, pressure, and voltage.

1) Sensitivity of actuator efficiency to initial braid radius

A sweep of braid radii from small (1.5 mm) to large (6.5 mm) is performed for an ideal actuator and a non-ideal actuator as defined in section 5.1.1. The results are shown in figure 12. For all braid radii, the ideal muscle exhibits an efficiency of 1 as defined by equation (26). However, as braid radii decreases, both the peak strain and the peak efficiency decreases as well. This indicates that for a given application, one would select a FAM with the largest possible braid radius, but, as can be seen in subsequent sections, this is not the case when designing for the system as a whole when considering a non-ideal muscle.

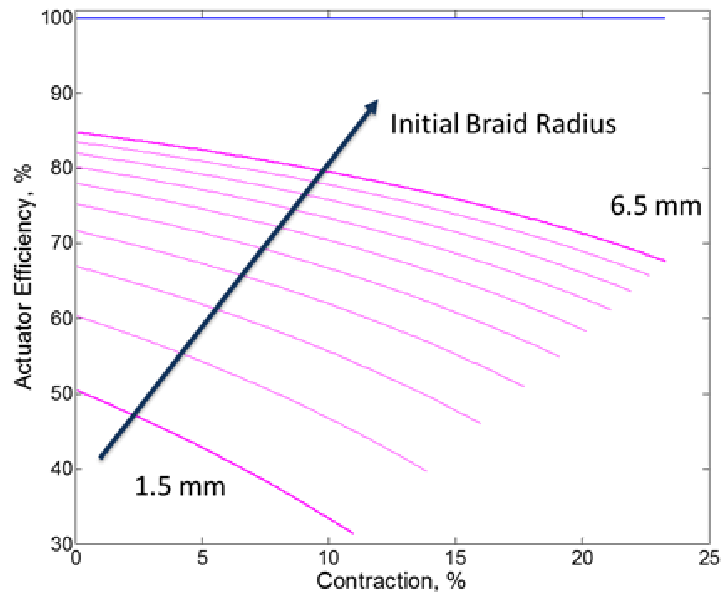

Figure 12: Actuator efficiency as a function of strain for a variety of braid radii with both ideal (blue) and real (magenta) muscle models.

2) *Effects of robot mass and initial braid radius on system performance*

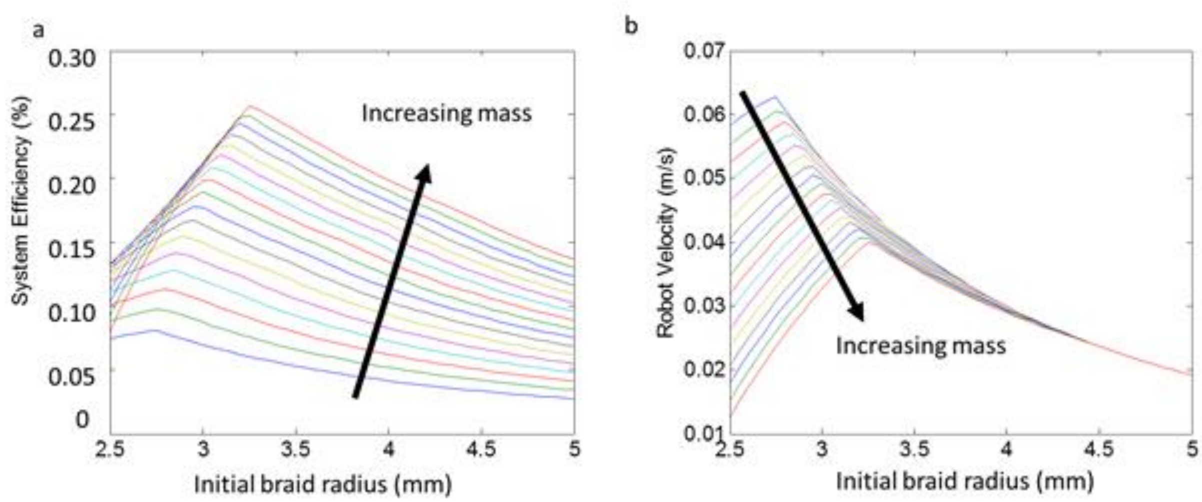

Figure 13: (a) Efficiency and (b) Velocity as functions of initial braid radius and robot masses from 1-5 kg.

Initial braid radii from 2.5-5mm for a range of masses from 1-5 kg were considered to produce the system efficiency and average velocity results shown in figure 13. For all masses, system efficiency and average velocity increase initially as braid radius is increased. This is because at low braid radii, output force is insufficient for complete muscle contraction—the FAMs are underpowered and this limits the cycle rate and the energy output. Peak system efficiency increases with mass over the entire range tested as it did in the mass-braid angle study; this is due to the increased energy output possible with a more massive robot. The optimal braid radius increases with increasing mass over the entire range due to the increased force output required to move the load. Because the output force of the muscle as described in equation (1) increases quadratically with the radius, FAMs with large radii can become overpowered—that is, they have a higher peak force output than necessary to reach full contraction allowed for the given load. The increased volume consumption in this case drives the system efficiency down rather than the contraction-limitations which occur at smaller, less forceful braid radii. The peak efficiencies and peak robot velocities occur at the same braid radius for a given mass, because volume consumption and average step-cycle rate are linked. As shown in equation (11), the larger volume consumed by the muscle, the more volume must be restored by the pump in order to restore operating pressure to its initial value. This requires more time, so step-cycle speed decreases. As mass increases at smaller braid radii, the efficiency drops due to the muscle contraction being limited by load.

3) Effects of operating pressure and initial braid radius on system performance

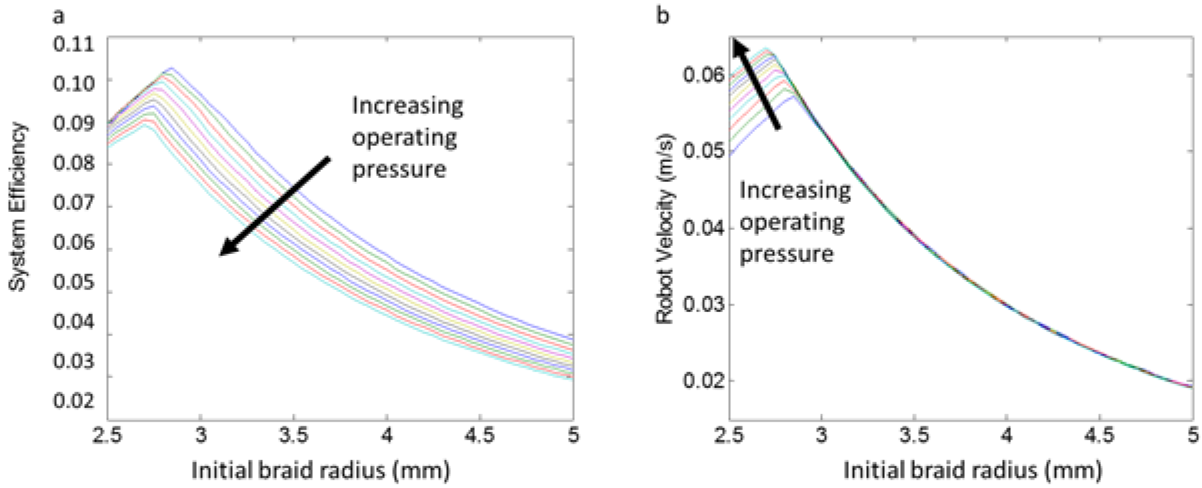

Figure 14: (a) Efficiency and (b) Velocity as functions of initial braid radius pressures from 500-1000 kPa.

The same range of braid radii are considered over a range of operating pressure from 500-1000 kPa in figure 14. As with the mass-sensitivity study, changing pressure affects peak system efficiency and the initial braid radius at which peak efficiency occurs. In increasing initial braid radius from 2.5mm to its optimal value, the lowest pressure demonstrates the highest sensitivity to initial braid angle. At initial braid radii greater than the optimal value, higher pressure shows an increased sensitivity to braid radius. Increasing pressure has a positive effect on robot velocity at lower braid radii, but this advantage decreases as braid radius increases beyond the optimal value. The positive impact of pressure on velocity and efficiency at low braid radii is because of the underpowered nature of the smaller FAMs. As the FAMs increase in size, the impact of the radius in volume consumption dominates the work output. Furthermore, at low braid radii, the lowest pressures fail to fully contract the FAM, resulting in low efficiency and velocity outputs. As with previous analyses, the balance between ensuring sufficient FAM output force while minimizing volume consumption is essential for achieving both optimal efficiency and robot velocity.

4) Effects of applied voltage and initial braid radius on system performance

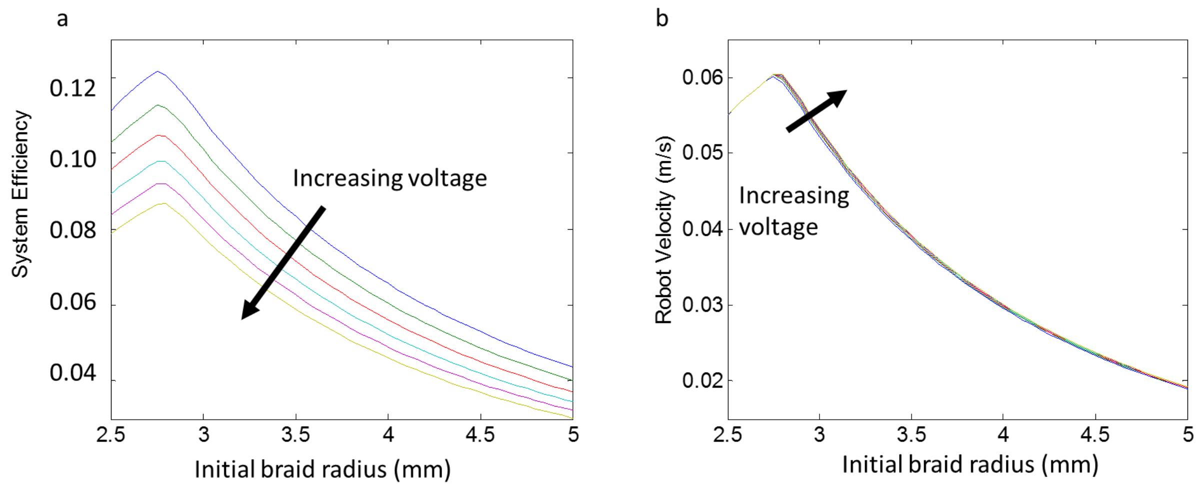

Figure 15: (a) Efficiency and (b) Velocity as a function of initial braid radius for applied voltages from 5-10 V.

Braid radius is next swept through the range of 2.5-5 mm for applied voltages from 5-10 V in figure 15. As with initial braid angle, when the FAM is underpowered, as at lower braid radii, applied voltage has no effect on the velocity of the system. While increasing voltage negatively affects the system efficiency, it has a negligible effect on the sensitivity of efficiency to initial radius. At all braid angles, using a higher system voltage is less efficient due to the larger power consumption of the system with negligible decrease in operating time. We see here, again, for an improved efficiency, the lowest usable voltage is best.

iii. Investigation of pump displacement effects

Pump displacement per revolution is an important design choice because it provides the physical coupling between the electrical and hydraulic aspects of the system. It directly impacts operating motor torque, pressure recovery and maintenance, and volumetric flowrate into the accumulator. Pump displacement is swept from values of 0.01 – 0.1 cm^3 for a range of robot masses, operating pressures, and applied voltages constraints in order to determine if there is an ideal pump displacement for the system in question and if so, whether and how that pump displacement is affected by other system parameters.

1) Effects of robot mass and pump displacement on system performance

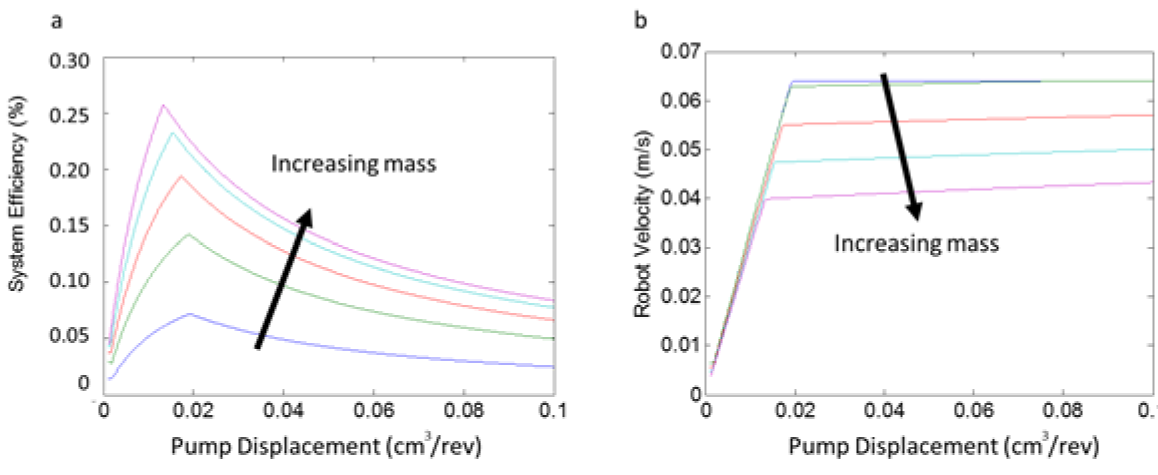

Figure 16: (a) Efficiency and (b) Velocity as functions of Pump Displacement for robot masses from 1-5 kg.

Figure 16 plots the resultant efficiency and velocity output plots as functions of pump displacement for robot masses from 1-5 kg. For each mass, there is an ideal pump displacement which correlates to the peak efficiency of the system as well as sharp change in the slope of the velocity curves. This point correlates to the pump displacement at which volumetric consumption by the FAM is more limiting than volumetric flowrate into the accumulator by the pump, governed by equations (11), (14), (15), and (16). At lower pump displacements, the FAM has reached contraction equilibrium prior to the accumulator being re-pressurized to its initial value. At higher pump displacements, the accumulator is refilled quickly, so it is FAM contraction equilibrium which drives cycle-rate. As can be seen in figure 16(b), at very low pump displacements, the motor can operate near its peak speed but not refill the accumulator quickly, causing prolonged operation at lower motor efficiencies, as well as impacting velocity negatively.

2) Effects of operating pressure and pump displacement on system performance

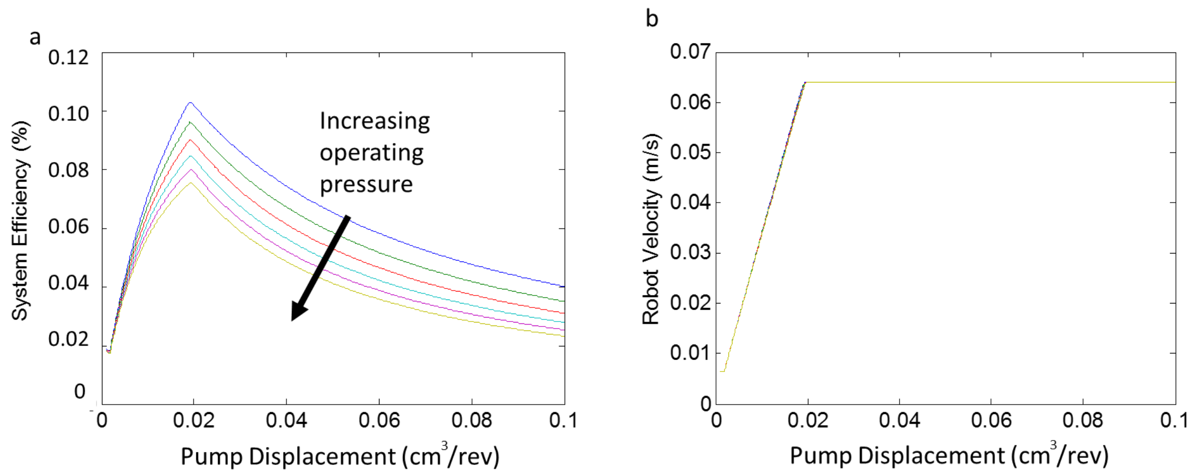

Figure 17: (a) Efficiency and (b) Velocity as functions of Pump Displacement for operating pressures from 500-1000 kPa.

In figure 17, pressure is swept from 500-1000 kPa for the same range of pump displacements. Increasing operating pressure increases pump torque, and therefore, system power consumption. This results in an efficiency drop at all pump displacements considered. Pressure has a negligible effect on the velocity of the robot in comparison to the pump displacement since, for the mass given, even the lowest applied pressure considered is sufficient to fully contract the FAM; therefore volume consumption is independent of pressure in the load case considered. Since volume consumption is not changed by pressure for this robot mass, the system efficiency is decreased from higher operating torques required for increased pressures. This indicates that the pump be designed such that the motor's steady-state operating speed is at or near its peak efficiency speed in order to refill the accumulator effectively while minimizing power draw.

3) Effects of applied voltage and pump displacement on system performance

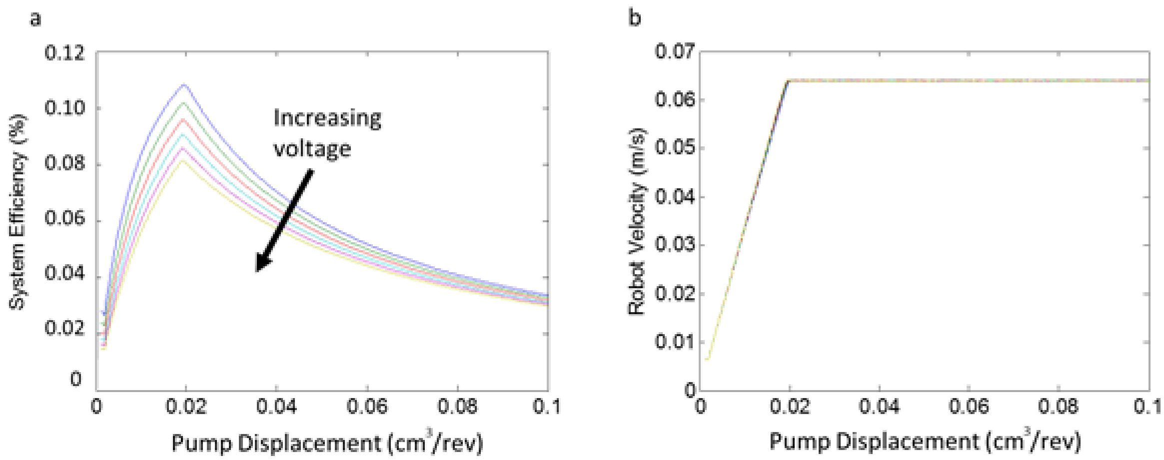

Figure 18: (a) Efficiency and (b) Velocity as functions of Pump Displacement for applied voltages from 5-10 V.

Figure 18 plots the system efficiency and velocity when voltage is varied from 5-10V for the same range of pump displacements. As with changes in pressure and mass, the velocity of the robot is largely unaffected by changes in applied voltage when compared to the pump displacement sensitivity. System efficiency is more sensitive to pump displacement changes at higher voltages, in addition to being less efficient. Increasing system voltage does increase operating motor speed, but this speed increase results in a larger current draw, so, as with the voltage studies performed in both FAM design studies, it is ideal to operate at the lowest reasonable voltage for the electrical system being designed.

f) Muscle Selection Case Study and Discussion

Based on results presented in Section 5, it is apparent that, while the FAMs exhibit improved actuator efficiency with smaller initial braid angles and larger initial braid radii, these straightforward trends do not necessarily hold when the system-level efficiency is considered. In order to delve deeper into the design and selection of muscle actuators for the climbing robot, a case-study is performed for a hypothetical robot which could carry a variable payload to operate with three different masses; 1, 3, and 5 kg at 500 kPa and 750 kPa operating pressure. The results of this study over a range of both braid radii and braid angles were calculated for each combination of mass and pressure. The results are shown in figure 19.

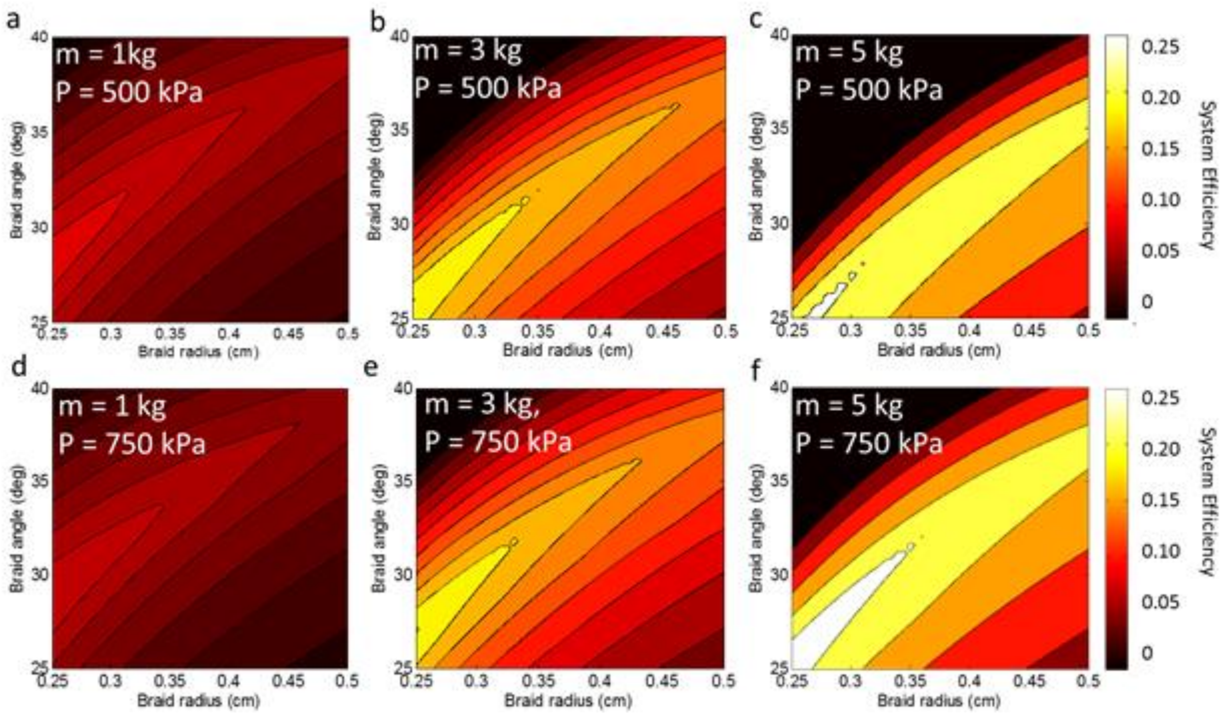

Figure 19: Efficiency as a function of initial braid radius and initial braid angle for robot masses of 1, 3, and 5 kg and system operating pressures of 500 and 750 kPa.

As is seen previously, with increasing system load, the peak efficiency is increased due to the larger potential energy output, but, as is more apparent when viewing these plots side by side, an increase in system load also decreases the braid angle for which the peak efficiency occurs. Furthermore, as load increases, the range of braid radii and braid angles for which the system will not operate (shown in figure 19 as zero efficiency regions) increases, even at a higher operating pressure. The higher operating pressure yields an increased range of peak efficiency and operational range for a heavier load, but a decreased peak efficiency and range for that efficiency at the lower loads. The implication of this case study is that it is critical to first discern the load of the system and then select the FAM and hydraulic operating pressure together such that peak efficiency can be attained. However, often FAM construction is limited to specific braid radii with limited braid angles [2]; figure 19 shows that, when operating at higher loads, these construction limitations can be overcome by increasing system operating pressure. Previous sections showed that, within a given muscle construction limitation, there are specific optima for operating and design parameters; that is, for a specific braid radius, there is an optimal braid angle for a given operating pressure and robot mass. This case study shows that the design characteristics interact with one another as well as the operating parameters such that there is an optimal combination of initial braid angle and initial braid radius for a given set of operating parameters. This radius and angle combination does not correlate to an isolated actuator's optimal characteristics.

g) Conclusions From Climbing Robot Study

The results outlined in this paper demonstrate the effectiveness of the coupled electro-hydraulic model at predicting the electrical energy consumption and mechanical output of the climbing robot used for this case study. They also show the interactive relationship between task and design in FAM usage. While the transduction efficiency of a FAM converting hydraulic input energy to mechanical output work is clearly maximized by selecting the largest possible initial braid radius and smallest possible initial braid angle, optimizing the system-level efficiency of the climbing robot is more complex. For example, in the case of a robot that changes mass when different payloads are attached or removed from the system, having the smallest braid angle would not provide the highest system efficiency for all operating modes. This would be an important consideration in many applications such as a disaster recovery or search and rescue robot that may need to deliver medical supplies or food to stranded persons or, at a larger scale, even transport injured victims to safety. In such a design, it would be more prudent to either size the actuators based on an expected average load over the course of the intended mission, or, in a more advanced design, make use of a bio-inspired selective actuator recruitment scheme that can choose to activate one of several parallel muscles to match the instantaneous load. The analysis presented here, while focused on the climbing robot application, is readily extended to other FAM-actuated robot geometries and operating concepts. The system-level analysis approach offers a new contribution to FAM actuator studies and demonstrates the links between FAM design and construction with their use in light-weight, robust, electro-hydraulic systems for prolonged use. The results of this study emphasize the importance of looking beyond the control and modeling of the actuator itself and into its contribution to and effect on the system as a whole.

CHAPTER III

Passive Variable Recruitment: A Bio-inspired FAM Recruitment Methodology (Accepted for publication (May 2018) in *Journal of Intelligent Material Systems and Structures)*

a) Variable Recruitment Background

Previous studies of FAMs have focused on modeling, control, and analysis of FAM contractile force output [4, 17, 21-23] based on idealized models and using experimentally derived correction factors to account for deviations from the ideal in the FAM performance as well as taking into account the elastic and material nonlinearities inherent in the construction of these artificial muscles [24]. Tiwari, et al. [7] and Meller, et al. [4] included work comparing hydraulic and pneumatic actuation—the results indicate that while pneumatics are cleaner and often have a simpler fluid circuit the compressibility of air causes pneumatic FAMs to be less efficient than their hydraulic counterparts. More recent studies have found more in-depth, predictive models of FAM output force and stroke during static and dynamic conditions [25-28]. There have also been a studies of how FAM design parameters impact the efficiency of an entire electro-hydraulic system in a self-contained mobile robot [29] as well as multiple other applications of FAMs in robotic and rehabilitation applications [12, 30-32]. Still others have investigated using bundles of FAMs and active control schemes to mimic biologically-inspired incremental muscle recruitment. Bryant, et al., first proposed this concept [5] by grouping multiple smaller muscles in parallel and showed, using quasi-static analysis and experiments, that performance gains were possible by actuating only the smallest FAMs needed to generate the desired output force and stroke. In most variable recruitment studies, a single FAM is considered as analogous to a mammalian muscle fiber and multiple FAMs, when actuated together, are considered a 'motor unit.' Using a control valve to actively pressurize or vent each motor unit is referred to henceforth as active variable recruitment (AVR). The active variable recruitment method has advantages over using a single, larger FAM and improved control algorithms have been developed to ensure the most effective control valve and throttle operation schemes are utilized. Jenkins, et al. [15] designed and characterized an intelligent FAM online variable recruitment switching scheme and Meller, et al. [33] experimentally demonstrated online variable recruitment control and efficiency improvements in a robot arm using a recruitment logic state machine. These studies show that when recruiting FAMs, it is more efficient to use smaller muscles when smaller output forces and displacements are required and to only engage more or larger FAMs when an increased force or displacement is necessary [6].

While the FAM AVR studies above illustrate the efficiency gains possible by selective recruitment control in FAM actuation systems, they require increased complexity in the fluidic circuit and additional control valves in the system, adding weight and bulk. Biology offers a simpler approach— physically encoding recruitment behavior in the actuator structure itself. In natural muscle tissue, motor units with larger muscle fibers tend to have larger motor neurons, which, due to their increased diameter have a larger minimum amplitude of stimulation required before recruitment occurs [34]**.** This recruitment process is known as Henneman's size principle and while there are some exceptions, motor units are generally engaged from smallest to largest. This is regulated by the central nervous system by the motor neurons and their associated axons [35]. An analogous behavior can be created in FAMs; those with thicker or stiffer elastomeric bladder materials tend to require larger applied pressures before output force or significant contraction are generated [26].

It has been shown [4, 25] that there are bladder-induced nonlinearities in FAMs based on the stiffness of the bladder. These bladder stiffness effects result in a minimum pressure that must be applied to a FAM before it contracts [26]. Pillsbury et al. refer to this minimum pressure as ‘deadband pressure’ and Sangian et al. refer to a similar phenomenon as ‘threshold pressure’ [25]. There is a relationship between the material thickness of the bladder as it compares to the volume of the whole FAM to this initial actuation pressure. This minimum actuation pressure will be called threshold pressure, P_{th}, in this study and will be described in more detail in the modeling section. This threshold pressure is typically considered a loss in the actuation of FAMs because it prevents force from being applied to the braid and therefore generating work output in the FAM until a larger pressure is applied. This study presents a method by which the threshold pressure effect can be used to create a simplified passive variable recruitment (PVR) control scheme which uses only a single throttle valve to control the activation of multiple FAM motor units.

This paper first discusses the modelling of fluidic artificial muscles and threshold pressure, including some design challenges involved in grouping muscles with different threshold pressures and elastic properties in parallel and potential solutions to these challenges. It then compares PVR bundles with a single equivalent motor unit (SEMU) and concludes with both a quasi-static and dynamic comparative efficiency analysis.

b) Elastic FAM modeling

As discussed previously, the ideal FAM force model is generally effective at predicting blocked force, but is generally poor at predicting free strain. Of note is that the ideal model predicts a constant free-strain which is based on initial braid angle as

$$\varepsilon_{free} = 1 - \sqrt{\frac{b}{a}}\,. \tag{35}$$

This is inconsistent with most experimental data; nearly every study shows a pressure-dependent departure between the ideal and the real free-strain data due to bladder elasticity effects [23, 27, 28, 36]. These mismatches, especially at lower applied pressure, have led to a variety of methods aimed at more accurately modeling and predicting the output force-strain behavior of FAMs. Tondu, et al. [17] and Meller, et al. [4] corrected for these losses using empirically determined blocked force and free-strain correction factors. Alternatively, attempts to model the elastic effects predictively have shown fairly accurate results [25, 27]. There are two effects created by the stiffness of the bladder used in building FAMs. The first is threshold pressure, P_{th}, and is defined as the minimum pressure required to overcome the radial elasticity of the bladder, expand, and exert contractile force in the braid [26, 36]. Threshold pressure was characterized by Pillsbury, et al. for some FAM construction methods as a function of the bladder volume ratio [26] and is assumed here as

$$P_{th}(kPa) = \left\{ \begin{array}{ll} 750\left(\dfrac{V_{bladder}}{V_{braid}}\right) - 337.5 & for\left(\dfrac{V_{bladder}}{V_{braid}}\right) \geq 0.45 \\ 0 & for\left(\dfrac{V_{bladder}}{V_{braid}}\right) < 0.45 \end{array} \right\} \tag{36}$$

where $V_{bladder}$ is bladder wall volume and V_{braid} is the volume enclosed by the braided sheath.

$$\left(\frac{V_{bladder}}{V_{braid}}\right) = \left(\frac{t_{0,bladder}}{R_{0,bladder}}\right)\left(2 - \frac{t_{0,bladder}}{R_{0,bladder}}\right) \tag{37}$$

where $t_{0,bladder}$ is the initial bladder wall thickness and $R_{0,bladder}$ is the initial bladder outer radius. Equation 10 is an empirical relationship based on the data reported by Pillsbury, et al [26]. These data were measured for FAMs constructed such that the bladder material is initially in contact with the braid. It is of note that if the FAMs are constructed with alternative materials or such that the bladder is not initially in contact with the braid, the P_{th} may vary from that predicted by equation 10 because additional pressure is required to inflate the bladder to the bladder-braid contact radius. For the study performed here, we assume FAMs similar to those in the Pillsbury study and which have construction-based contact between bladder and braid prior to any FAM pressurization.

The second elasticity effect is due to the pressure required to stretch the bladder after threshold pressure has been reached. This has been modeled by various researchers and depends on the construction of the FAM itself. We assume that this elasticity can be modeled by the thin-walled model presented by Sangian et al. [25]:

$$F_m = P_{eff}\pi R_0^{\,2}\left[a\left(1-\frac{x}{L_0}\right)^2 - b\right] \tag{38}$$

where P_{eff} is the pressure transmitted through the bladder to the braid and is defined as

$$P_{eff} = P_{app} - P_{el}\,, \tag{39}$$

and P_{el} is pressure loss caused by the bladder elasticity; it is defined as

$$P_{el} = P_{th} + \frac{E_b t_{0,bladder}}{R_0 \sin\alpha_0}\left[\left(1-\left(\frac{L_0 - x}{L_0}\right)^2 \cos^2\alpha_0\right)^{1/2} - \sin\alpha_0\right] \tag{40}$$

where E_b is the Youngs modulus of the bladder.

c) Passive Variable Recruitment

As discussed in the modeling section, bladder elasticity creates an internal energy storage in the FAM and decreases the amount of output work performed by the actuator in contraction. Some FAM materials have minimal or no threshold pressure, [4], but since this is not universally the case, learning to harness, rather than avoid, the threshold-pressure phenomenon is essential. To this end, we consider the advantages of a bio-inspired control system which makes use of a single pressure control valve to activate multiple FAMs, whose output is determined by their elasticity and threshold pressure. This has the simultaneous advantage of reducing the number of often bulky control valves and simplifying the system control algorithms as compared to the active variable recruitment approach previously discussed. By using motor units consisting of one or more “low threshold pressure muscle(s)” (LTPM) in parallel with a motor unit consisting of one or more “high threshold pressure muscle(s)” (HTPM), it is possible to gain the benefits of variable recruitment; that is, low volume consumption when force output requirements are lower; without the drawbacks of large or numerous control valves and complex control algorithms. We will refer to these motor units as low and high threshold pressure motor units (LTPMU and HTPMU). Figure 20 shows the fundamental set up of the simplest PVR bundle: a LTPMU consisting of a single muscle in parallel with a HTPMU consisting of a single muscle with both motor units connected to a common control valve. The biological motivation for this study lies in Henneman’s size principle, as discussed previously.

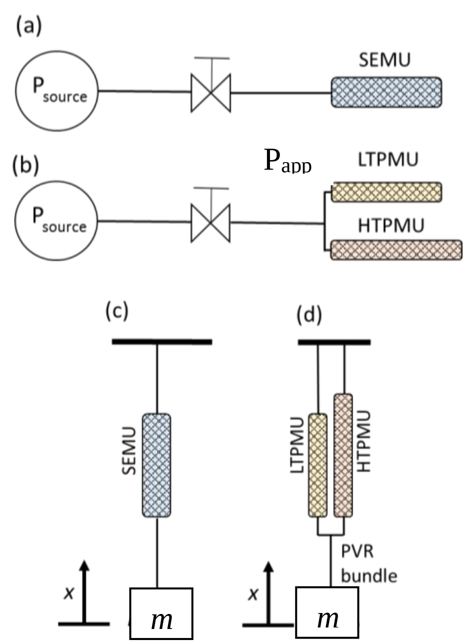

Figure 20: Hydraulic system of a) SEMU and b) PVR bundle, and constant force and actuation setup of c) SEMU and d) PVR bundle.

i. Experimental validation and discovery of lag pressure

In order to test both the FAM contractile model and the ability of two non-similar FAMs to operate in parallel as part of a PVR bundle, we performed an experiment on an in-house PVR bundle composed of a HTPMU with one FAM with initial length of 0.29 m and P_{th} = 70 kPa in parallel with a LTPMU with initial length of 0.18 m and P_{th} = 0 kPa. Both muscles had an initial braid radius of 6 mm. The experimental data for our in-house bundle lifting an 11.4 kg load and the previously described model are shown along with photographs of the FAMs used in the experiment are shown in figure 21. Also plotted are the displacement of the load when it is lifted by the LTPMU alone and the unloaded (free) contraction of the HTPMU with pressure. As shown, the HTPMU begins to contract at 70 kPa but, even without load, does not contract the same distance as the LTPMU until 205 kPa is reached. At above 205 kPa, the PVR bundle contracts uniformly. The change in slope at 205 kPa is due to the additional force provided by the HTPMU when it reaches equal contraction with the LTPMU. This delay in contraction before force is contributed by the HTPMU is referred to henceforth as lag pressure, P_{lag} and will be discussed in more detail in the *Lag Pressure Quantification* section. Of note is how the loaded condition of the bundle tracks with the loaded condition of the LTPMU until after the system reaches lag pressure, after which, the bundle contracts more than the loaded condition of the LTPMU. The model slightly under predicts contraction at higher pressures by approximately 0.5% bundle strain. This experiment shows validates the concept of PVR bundle activation using a single throttle valve and suggests that more fully understanding the design criteria for FAM selection within such a bundle is critical. Quantifying this methodology and studying the design considerations required in bundling FAMs in this way will comprise the remainder of this section.

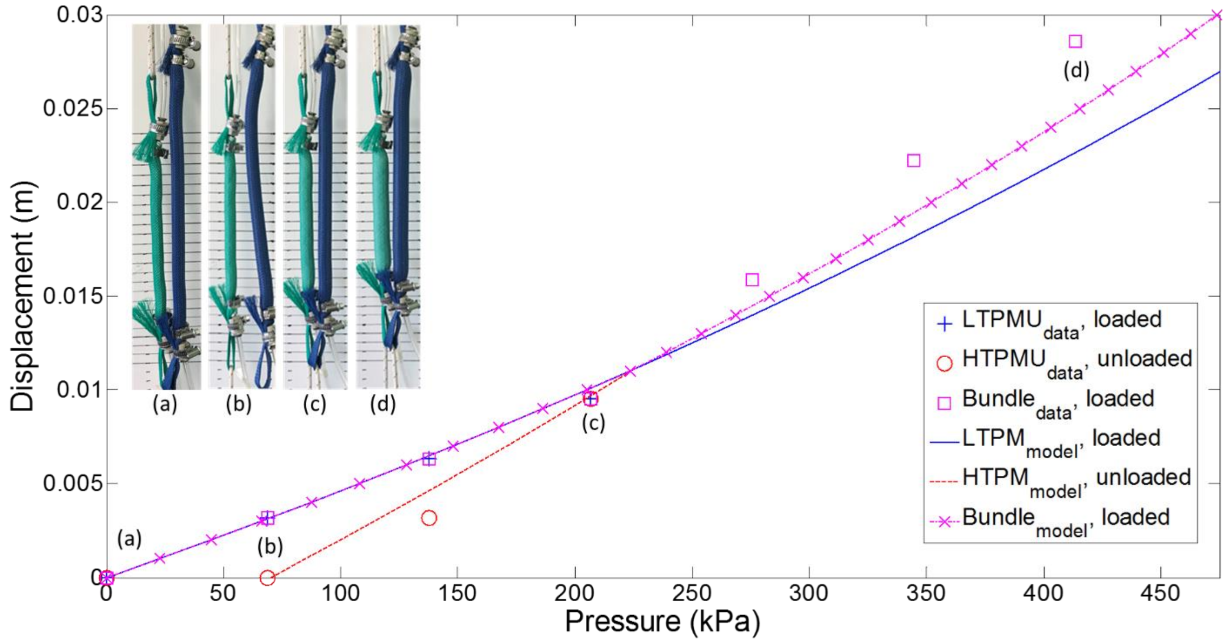

Figure 21: Model and experimental data for a PVR bundle consisting of a LTPMU (green) and a HTPMU (blue) when they are a) both unpressurized, b) both pressurized and below lag pressure, and c) both pressurized at lag pressure, and d) both pressurized and above lag pressure.

ii. Definition of single equivalent motor unit

In order to perform the analyses required for this study, we compare passive variable recruitment bundles to a single equivalent motor unit (SEMU) as sketched in figure 20. The parameters of the SEMU are defined such that its blocked force, F_{bl}, and its free-stroke (x_{free}) are identical to that of the PVR bundle at a given source pressure. As will be discussed later, having a higher available source pressure will have an effect on both the x_{free} and F_{bl} of a FAM, motor unit, and bundle. Since we define a SEMU as having the same blocked force and free stroke as the PVR bundle, it is first necessary to consider the effect of design parameters on these outputs.

iii. Design considerations for PVR bundles

Upon inspection of equations 12, 13 and 14, it is evident that free strain and blocked force are dependent on multiple FAM design parameters. These parameters include initial braid angle, initial muscle length, initial braid radius, initial bladder thickness, and bladder elasticity. Since we have defined a single equivalent motor unit as a single FAM which has the same blocked force and free stroke as the passive variable recruitment bundle (including two or more FAMs of differing threshold pressures), it is necessary to be able to determine the effects of the parameters listed here on the free strain and blocked force. This will also allow differing FAMs in the bundle to produce the same contraction when source pressure is applied.

1) Free strain design considerations

Inspection of equation 12 shows that when calculating free strain, there are two possibilities: 1) free contraction is limited by braid kinematics, or 2) free contraction is limited by bladder elasticity effects. If the muscle parameters are such that braid kinematics limit free strain, contraction is governed by equation 9. If the parameters are such that bladder elasticity limits the free strain, equations 13 and 14, which govern P_{eff}, are the driving factors behind the free strain limit. In either case, initial braid angle affects free strain calculations. Since, for finding the size requirement for the SEMU, we need to understand free strain contraction at source pressure, we consider several source pressures from 250 kPa (just above the $P_{th,HTPMU}$ used for our analyses in the comparison and case study sections) to 500 kPa. The results indicate that, for a given bladder thickness, which affects both the P_{th} and the P_{el}, there is a difference in the effect of braid angle on free strain that depends on the source pressure applied. Figure 22 shows bladder thicknesses of 3 mm, 2 mm, 1 mm, and 0.5 mm for a braid radius of 6mm and Young's Modulus of 0.9 MPa and the effect of both source pressure and braid angle on the free strains. As can be seen, the choice of braid angle, bladder thickness, and source pressure combine to affect free strain. At low initial braid angles, this effect is magnified due to the governance of equations 2 and 3 in FAM operation; at smaller initial braid angles the radial strain for a given axial contraction is greater. Even though at lower initial braid angles the ideal model predicts an increase in free strain, the increased radial expansion by the braid at low braid angles causes an increase in work done by the working fluid on the bladder. Since the work done in stretching the bladder is not recoverable, this is expressed as increased lost in the actuator and, subsequently, a limit on free-contraction at a given source pressure.

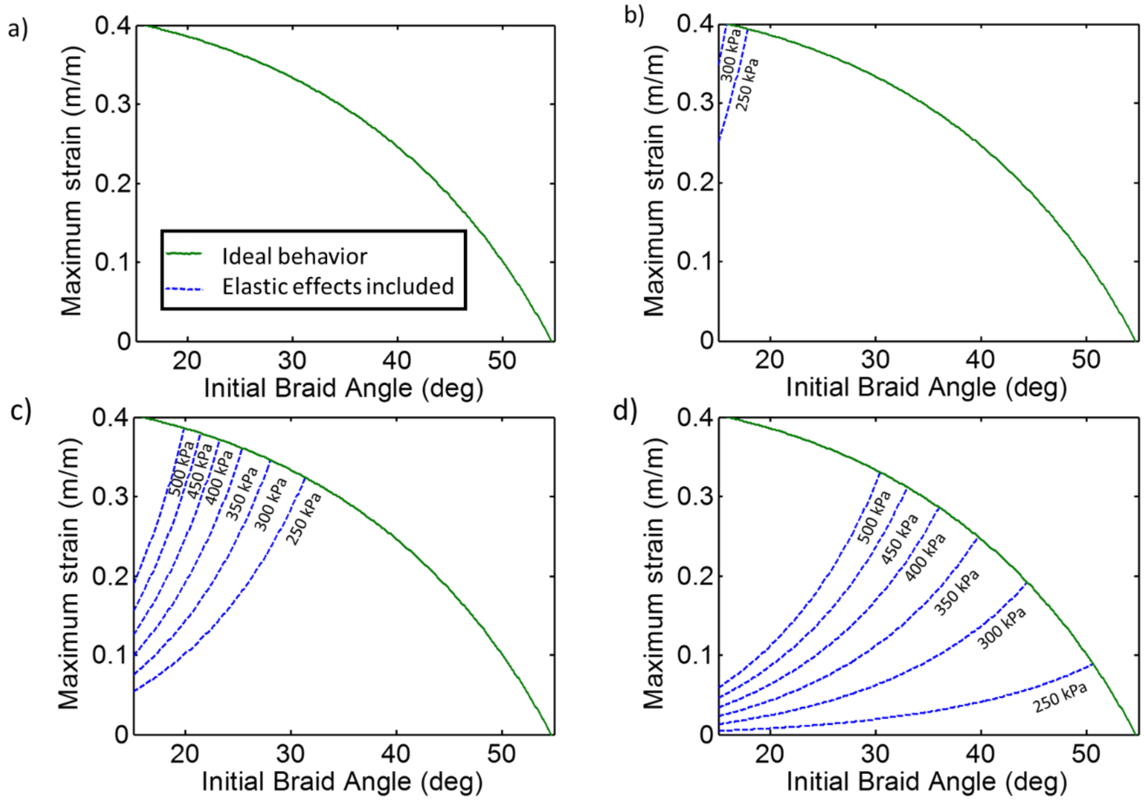

Figure 22: Relationship between initial braid angle and free strain for a) 0.5 mm, b) 1 mm, c) 2mm, and d) 3 mm bladder wall thickness for a 6 mm radius FAM for source pressures of 250 kPa to 500kPa. Note that as bladder thickness increases, there is a corresponding increase in the domination of the elastic effects in limiting the free strain.

Since the P_{source} for this study will be 450 kPa, the bladder thicknesses above were used to calculate the free strain for various braid angles. The results are shown in figure 23 and show that at that the source pressure for this study (450 kPa), a FAM with an initial braid angle of 30 degrees and a 3mm thick bladder will be limited by the elastic bladder to a free strain of ~25% while a thinner bladder of the same braid angle will have a free strain of ~33%**.** The study of these effects on strain allow engineers to make decisions about FAM design when grouping FAMs with differing bladder thicknesses and threshold pressures since using muscles with different thicknesses will carry with it the added design challenge of ensuring free contraction is the same for bundled motor units. Designers could either select HTPMU and LTPMUs sheaths which have different initial braid angles or select LTPMUs and HTPMUs with differing lengths.

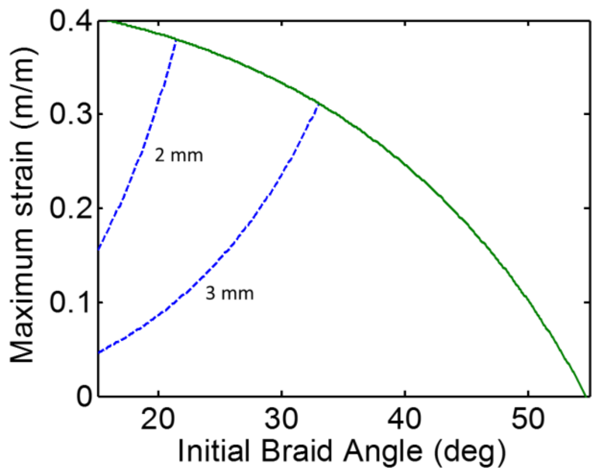

Figure 23: Ideal (green) and non-ideal (blue, dashed) free strain as a function of braid angle at 450 kPa for a 6mm radius FAM with bladders of wall thickness 2mm and 3 mm. As shown in figure 22, at 450 kPa, bladders of 0.5mm and 1mm have a negligible effect on free strain.

2) Blocked force design considerations

Similarly, threshold pressure has an effect on the blocked force generated by a FAM and in order to ensure the SEMU has the same blocked force as the combination of LTPMUs and HTPMUs bundled in parallel, it is necessary to determine how the design parameters affect blocked force. Since blocked force occurs at $x = 0$, equations 12 and 14 simplify to

$$F_{bl} = P_{eff}\pi R_0^{\,2}\left[a-b\right]. \tag{41}$$

where $P_{eff} = P_{app} - P_{th}$ because $P_{eff} = P_{app} - P_{th}$ when $x = 0$. For various bladder thicknesses, equation 15 applied yields the blocked force results shown in figure 24 for braid angles of 20 to 40 degrees.

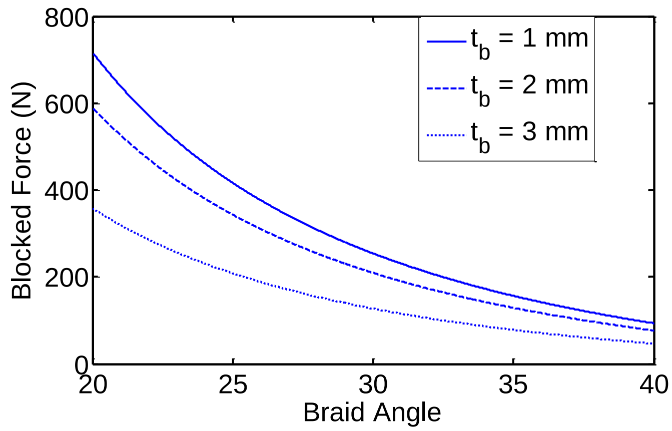

Figure 24: Blocked force as a function of braid angle for a FAM with 6mm initial braid radius and various bladder thicknesses at a source pressure of 450 kPa.

These results give the researcher the opportunity to predict the blocked force of a FAM motor unit and use that information to select SEMU design parameters which are appropriate. By selecting braid radii, bladder thicknesses, and braid angles which result in the same blocked force in the SEMU as the combination of LTPMU and HTPMU, we ensure validity of the comparison. In this study, we select a SEMU with the same braid angle as the PVR bundle and the same bladder thickness as the LTPMU. This allows the initial braid radius of the SEMU to be calculated by

$$R_{braid,SEMU}{}^{2} = \frac{(P_{source} - P_{th,LTPM})R_{braid,LTPM}{}^{2} + (P_{source} - P_{th,\mathrm{HTPM}})R_{braid,\mathrm{HTPM}}{}^{2}}{(P_{source} - P_{th,SEMU})} \tag{42}$$

iv. Quantification of lag pressure

As shown in the experimental validation section and as indicated by further inspection of equation 14, there will be a lag in contraction between a HTPMU being actuated and reaching the same contraction as an in-parallel LTPMU. The pressure required to bring the HTPMU to the same contraction as the LTPMU, $x_{current}$, is referred to as lag pressure and defined as

$$P_{lag} = P_{th} + \frac{E_b t_{0,bladder}}{R_0 \sin\alpha_0}\left[\left(1-\left(\frac{L_0 - x_{current}}{L_0}\right)^2 \cos^2\alpha_0\right)^{1/2} - \sin\alpha_0\right] \tag{43}$$

where $x_{current}$ is the current contraction position of the bundle. Figure 25(a), shows PVR bundle force at P_{th}, P_{lag}, and P_{source} for a LTPMU in parallel with a HTPMU with $P_{th,\ HTPM} = 0.5P_{source}$. We note that when displacement, x=0, that lag pressure is equal to threshold pressure and that therefore blocked force is the same for both the P_{lag} and $P_{th,\ HTPMU}$ curves. Figure 25(b) and 25 (c) show the change in slope of bundle output force from the actuation of the HTPMU when (b) there is no displacement in the HTPMU and (c) when there is a non-zero displacement. The slope of blocked force (b) occurs as soon as threshold pressure is surpassed, whereas when displacement in the HTPMU is non-zero (c) that increase occurs at lag pressure. The shaded areas in figure 25 (a) demonstrate the areas where the LTPMU provides force and consumes fluid volume, only the LTPMU provides force but both the LTPMU and HTPMU consume fluid volume, and where both the LTPMU and the HTPMU provide force and consume fluid volume.

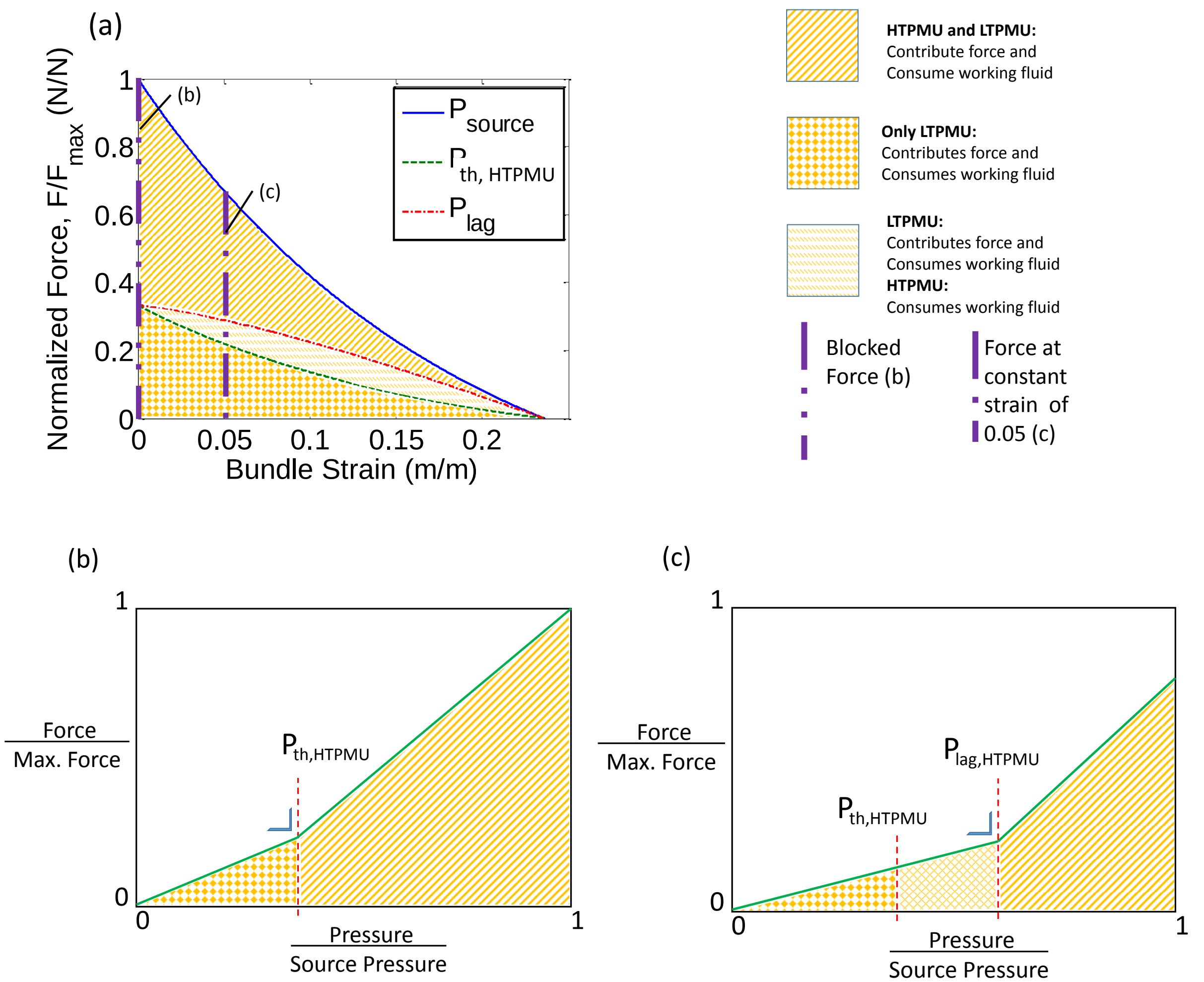

Figure 25: a) PVR bundle normalized force and strain for applied pressure of P_{source}, $P_{th,HTPM}$, and P_{lag}. Normalized force as a function normalized applied pressure at b) zero bundle strain (blocked force condition) and c) 0.05 bundle strain.

d) Isobaric PVR-SEMU Comparison

Having established a method for ensuring equivalent operating characteristics, it is now possible to compare a PVR bundle composed of one LTPMU and one HTPMU with a SEMU. This is performed to determine 1) if PVR bundles are ever more efficient than a SEMU and 2) if so, through what portion of the force-displacement space their use is beneficial. The parameters of the FAMs in the motor units considered, calculated using the methods described in the design considerations section, are shown in Table 4. Note that P_{source}=450 kPa and $P_{th,\,HTPM}=0.5\ P_{source}$.

Table 4: PVR and SEMU FAM parameter values

	LTPM	**HTPM**	**SEMU**
L_0 *(m)*	0.1	0.14	0.1
$R_{0.braid}$ *(m)*	0.006	0.006	0.0073
$t_{bladder}$ *(m)*	0.001	0.003	0.001
E_b *(MPa)*	0.9	0.9	0.9
P_{th}*(kPa)*	0	225	0
α_0*(deg)*	30	30	30

We first compared the force-stroke-efficiency relationship of FAMs in the PVR bundle to that of a SEMU. FAM Bundle and SEMU efficiency were defined to be

$$\eta_{bundle} = \frac{\int F_{bundle} dx}{P_{source} \int dV} \tag{44}$$

$$\eta_{SEMU} = \frac{\int F_{SEMU} dx}{P_{source} \int dV} \tag{45}$$

where P_{source} is the source pressure and F_{bundle} and F_{SEMU} are the stroke-and-pressure dependent output force of the PVR bundle and the SEMU, respectively. Figure 26 shows the quasistatic isobaric contraction efficiency for both a PVR and a SEMU as calculated by equations 18 and 19. Each actuation efficiency is calculated as the PVR bundle or SEMU contracts from $x=0$ at a constant pressure.

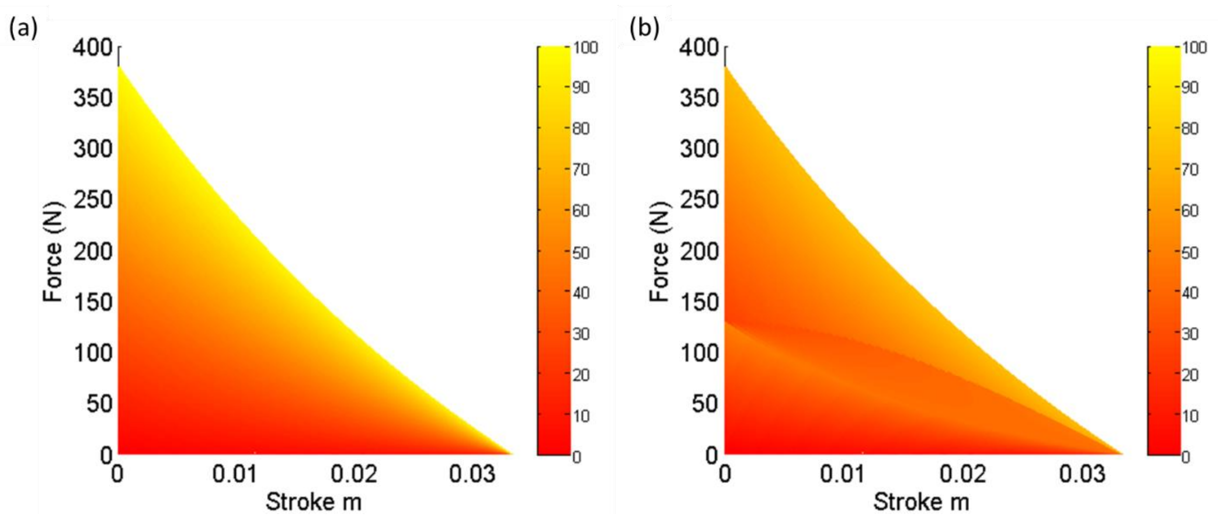

Figure 26: Actuator efficiency for the force and stroke characteristics of a) a PVR bundle with two muscles and b) a SEMU with a peak pressure of 450 kPa. These plots show the equal blocked force and free stroke, as defined. Note the area of decreased efficiency in the PVR bundle corresponding to the area between $P_{th,\ HTPMU}$ and P_{lag} and the area of increased efficiency in the PVR bundle corresponding to applied pressures below $P_{th,\ HTPM}$.

As shown in figure 26, the PVR bundle is able to operate in the lower-force regime with higher efficiency than the SEMU, but as applied pressure increases above the threshold pressure of the HTPM, the volume consumption makes an equivalent increase and the efficiency of the PVR decreases below the efficiency of the SEMU. Average efficiency in the PVR bundle is 40.7% and for the SEMU is 45.5%, which assumes operation at every point in the force and strain space equally. A differential efficiency plot was generated in order to show the points at which the PVR is more efficient than the SEMU and is shown in figure 27**.**

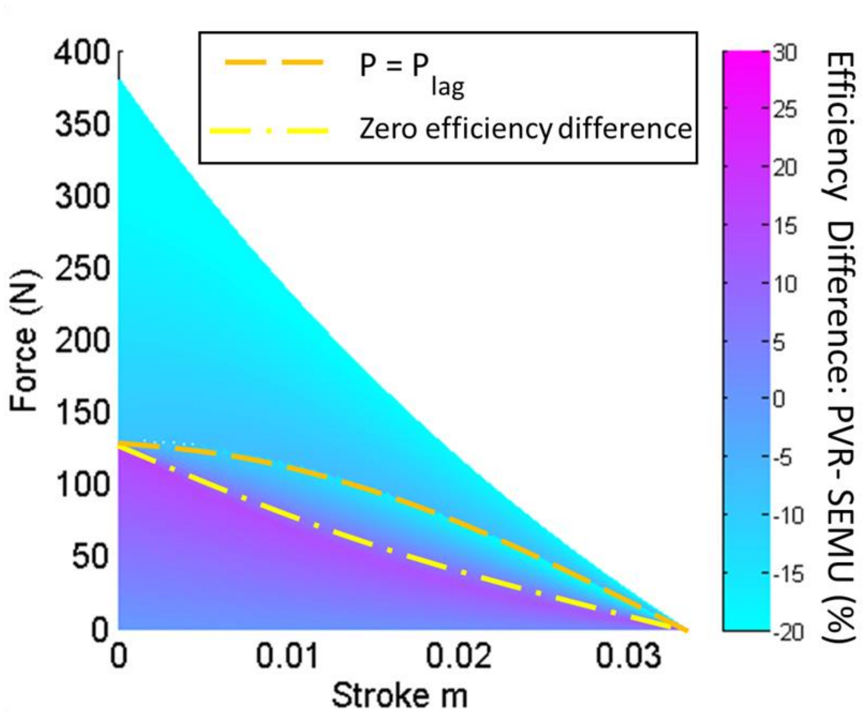

Figure 27: Efficiency difference between PVR Bundle and SEMU. At pressures below $P_{th,HTPM}$ the PVR is more efficient because the HTPMU is not consuming fluid volume. Of interest is that the percent difference is zero at $P_{th,HTPM}$.

This implies that for a system in which the primary mode of operation requires either small loads or small deflections of a moderate load (less than ~ 125 N), the PVR bundle is more efficient and at large loads the SEMU is more efficient. It is worth noting that in the case where the higher loads or displacements are *never* required, it would in fact be most efficient to use a single smaller muscle and operate closer to the maximum system pressure, thereby minimizing throttling losses. In the case that a larger output force is needed occasionally and that it is difficult or undesirable to change system pressure when that need occurs, it would be more efficient to use a PVR bundle. We further investigate these situations in the actuation case studies section**.**

e) *PVR Bundles and SEMU Actuation Case Studies*

i. *Constant force actuation*

An initial way of comparing the actuation efficiencies of a PVR bundle to a SEMU is to simulate their stroke through the full range of motion while exerting a constant force. In order to do this, three forces were selected for the motor units described in Table 4, one correlating to 1/10th of the peak output force of the SEMU and PVR bundle, one at 1/4th and the other at 1/2 the peak output force. Figure 28 shows the load-paths of loads 1, 2, and 3 described above.

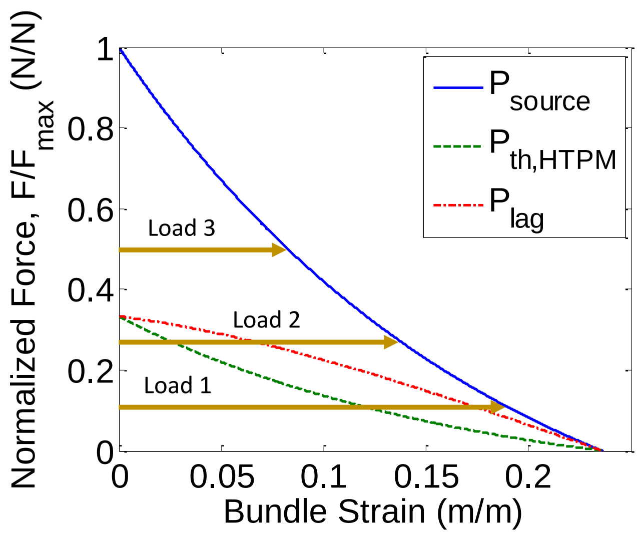

Figure 28: Force output of PVR bundle when applied pressure is source pressure, HTPMU threshold pressure, and lag pressure.

Figure 29 shows the required applied pressure and the fluid volume consumed for both the PVR bundle and SEMU as functions of contraction. What is most interesting in this analysis is the response of the fluid volume consumption as pressure approaches first the threshold pressure and then the lag pressure. When applied pressure is lower than threshold pressure for the HTPMU, the volume consumption of the PVR bundle is lower than that of the SEMU; indicating through equations 18 and 19 that the actuation efficiency of the PVR bundle is higher than the SEMU. When applied pressure is higher than threshold pressure, but lower than the lag pressure, only the LTPMU is contributing to the force application, but both the HTPMU and the LTPMU are consuming working fluid. In his case, equations 18 and 19 would show a decrease in PVR bundle efficiency from the increased volume consumption.

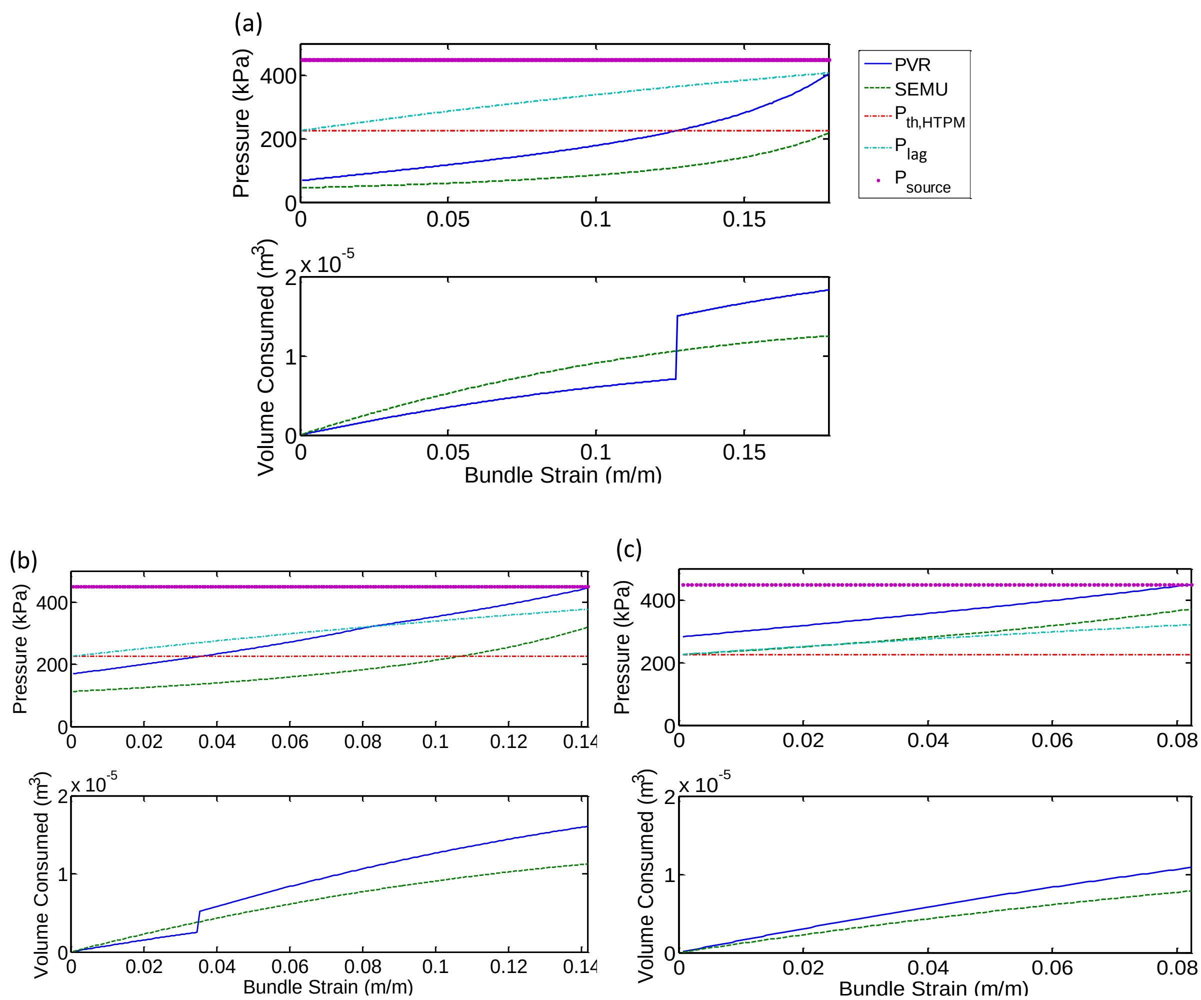

Figure 29: Applied pressure and volume consumed by the PVR bundle and SEMU for a) load 1, b) load 2, and c) load 3. Note that the maximum displacement is smaller as load increases. At high loads, the SEMU always consumes less working fluid because the HTPMU is always engaged and that at light loads and small displacements the PVR bundle always consumes less working fluid.

ii. Inverse dynamics analysis

In order to determine if the PVR concept is a worthwhile recruitment methodology, it is necessary to quantify the effect of the percentage of total operation spent in a given operating region. The actuator efficiency plots shown in figures 26 and 27 are for isobaric contraction, not actuation with time-varying pressurization to track a desired path. Thus, determining the implications of path-following actuation with various loads and paths is not as simple as merely taking a weighted average of the number of cycles in each operating regime due to the path-dependency of the work output of FAMs [33]. In order to do so, we considered a series of cases in which a SEMU or PVR bundle was used to produce a prescribed displacement history under load. We then solved for the required applied pressure history, fluid volume consumption history, and resulting actuator efficiency. This inverse dynamics method is common amongst biomechanical studies [37-39] and is used here to glean additional insight into the actuator efficiency. Mammalian muscles provide a variety of strains and forces [40] and, as discussed in the introduction, are comprised of many motor units and controlled by a common signal from the central nervous system. In keeping with the mammalian muscle force-strain studies [40] which inspired this study, the PVR bundle and SEMU output forces were normalized by peak output force at source pressure and the free strain associated with those force outputs. In order to determine the range of operation during which the PVR bundle is more efficient than a SEMU, we studied a variety of forces and strains with our system.

Bioinspired examples of muscle contraction are myriad; the same muscles which allow human walking movement over flat ground are capable of applying the forces needed to perform steep hill, stair-climbing movements [41, 42] as well as lifting heavy loads. The muscle engaged in picking up a pen from a table at elbow level are the same as those doing dumbbell curls at the gym; a wide variety of forces must be available as even the initial position of the limb impacts its required force profile [43]. Even though these applications use the same skeletal muscles, they require different force and contraction profiles [44]. As was shown in PVR-SEMU comparison section, if a large range of displacement with a moderate load is always desired, the SEMU will generate the necessary force with a smaller volume consumption, and therefore higher efficiency. However, as with mammalian muscles, it is important to consider the time spent operating in each force-displacement regime and design for maintaining capability to perform in all required regimes. This study examines a variety of load and displacement cases in order to determine if and when PVR muscle bundles should be utilized.

In order to determine the efficiency of the PVR bundle in comparison to the SEMU, an inverse dynamics simulation was performed for a sinusoidal displacement history of a given load mass, *m* as

$$x(t) = \frac{x_{\max}}{2}\cos(\omega t - \pi) + \frac{x_{\max}}{2}, \text{ and} \tag{46}$$

$$m\ddot{x} = F_m - mg \tag{47}$$

where $x(t)$ is the prescribed displacement history and $x_{\max}$ is the peak displacement. Several combinations of $x_{\max}$ and *m* were selected to capture different regions of the system force-strain space. A circular frequency, ω, *of ½ Hz* was set for all the cases simulated. In each simulation, two operating conditions were considered, a base low-load / low-strain condition and a more demanding condition with either increased load or increased strain required. A varying percentage of the operating cycles were simulated at each operating condition. The percentage of total operation cycles with the increased contraction or load was swept from 0% (100% low-strain and/or low load) to 100% (0% low strain and/or low load). Figure 30 shows 5 cycles of an example study during which 40% of the cycles were performed with low displacement and 60% were performed at a high displacement. These inverse dynamics studies are performed in order to determine if and how the PVR bundle is advantageous over a SEMU when moving an inertial load with a prescribed displacement history.

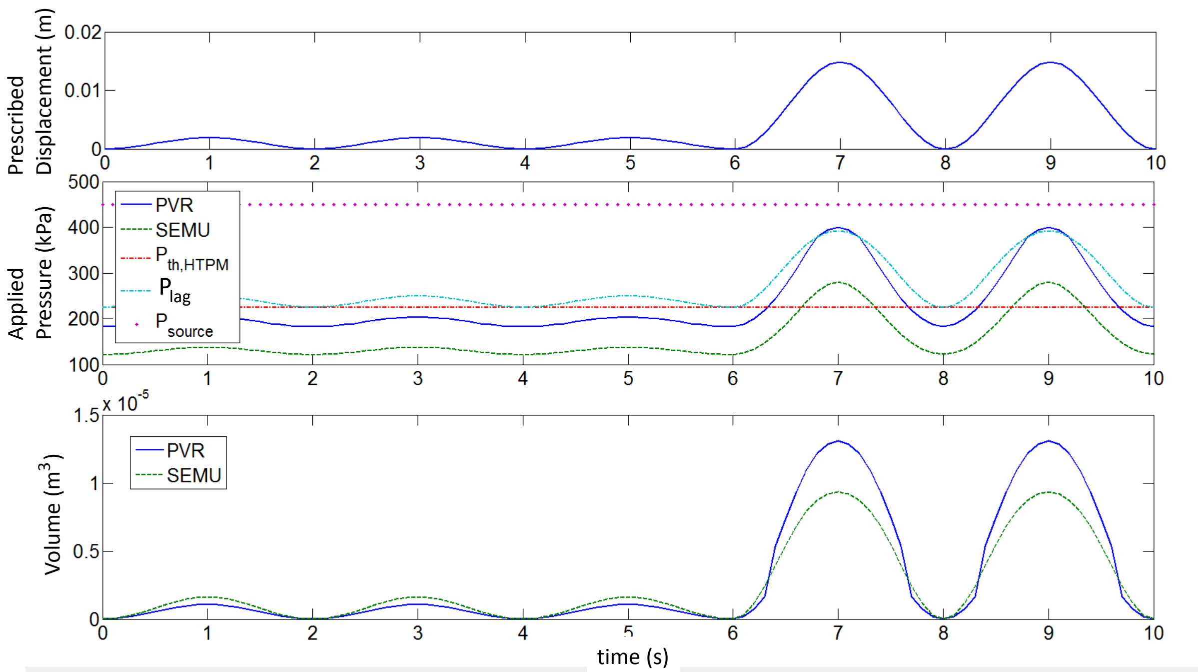

Figure 30: 5 cycle operation performed at a constant (low) load and varying displacement.

Similarly, figure 31 similarly shows a constant displacement amplitude with an increased load for 60% of the operating cycles.

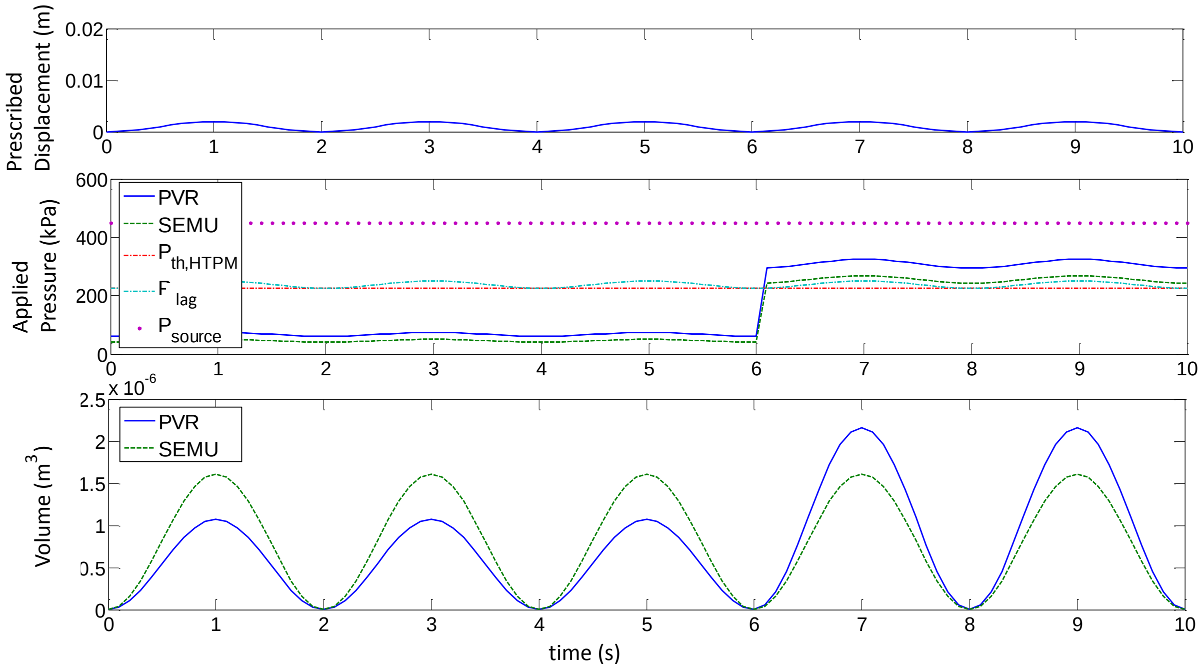

Figure 31: 5 cycle operation at constant (low) displacement and varying load.

Figure 32 shows some of the points analyzed in this study. These cases, whose results are shown in figure 33, were selected because they demonstrate the extremes; low efficiency when operating at below the threshold pressure of the HTPMU and near the peak efficiency within the SEMU operating region.

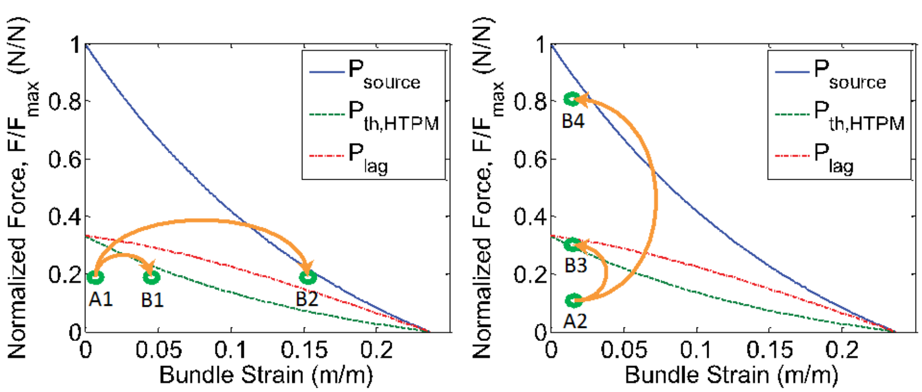

Figure 32: Load and displacement selection points for the trials shown in Table 5.

Table 5 shows the data from the analyses described in figure 32**.**

Table 5: Dynamic case study load and strain values

Case	Load A (mg/F_{max})	Load B (mg/F_{max})	Strain A	Strain B
A1→B1	0.2	0.2	0.014	0.16
A1→B2	0.2	0.2	0.014	0.046
A2→B3	0.1	0.3	0.014	0.014
A2→B4	0.1	0.8	0.014	0.014

For each case, a crossover point can be determined that represents the maximum fraction of operating cycles at the higher load or strain, for which the PVR bundle is more efficient than the SEMU. For example. in a biomimetic context, having a crossover of 11% is analogous to a muscle system being more efficient if 89% of the day is spent walking on flat ground while 11% or less of the day is spent walking uphill. Cases where the low-force or low-strain operating point was closer to the threshold pressure of the HTPMU had higher crossover points, meaning that it was increasing advantageous to select a PVR bundle over a SEMU. When the system operates below $P_{th,HTPMU}$ for the majority of the time, it is more efficient to use a PVR bundle than to use a SEMU. However, as the percentage of operation at an increased load or displacement increases, designers would be remiss not to reconsider the FAM selection. Of further interest is that changing the ratio of $P_{th,HTPMU}$:P_{source} has the effect of changing the crossover point for a bundle as it compares to a SEMU. For the same threshold pressure shown here and a P_{source} =375 kPa ($P_{th,HTPMU}/P_{source}$ = 60%), the crossover point for the A2→B4 case becomes 55% (shifts to the right, in favor of PVR bundle). Similarly, changing P_{source} = 550 kPa ($P_{th,HTPMU}/P_{source}$ = 40%) changes the crossover point to 37% (shifts left, in favor of SEMUs), This is due to the increased portion of the force-strain space for which the HTPMU is engaged and therefore the PVR bundle is consuming more working fluid than the SEMU. This further emphasizes the need for determining the purpose for which an actuator bundle is being purposed when designing its component FAMs.

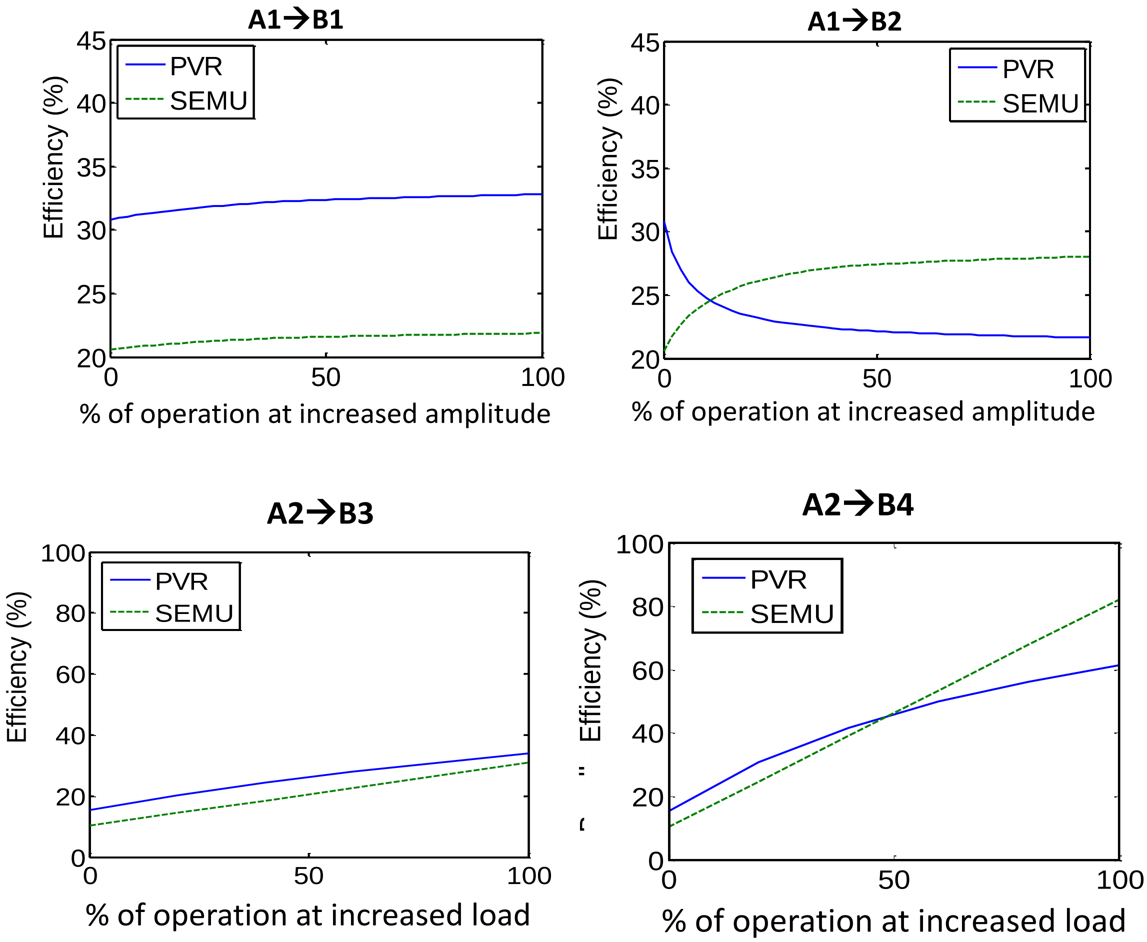

Figure 33: Operating efficiencies for varying percentages at a higher load or displacement cases.

f) Conclusions from Passive Variable Recruitment Study

Fluidic artificial muscles have the potential to make a large impact in the wearable assistive robotics and mobile rehabilitation fields due to their light weights, high force-weight ratios, flexibility, ease of scalability, and low cost. In order to fully integrate these soft-actuators into wearable exoskeletons and prosthetic or orthotic devices it is necessary to understand their construction, model their performance and limitations, and design systems which capitalize on their functionality. This study specifically addresses the fundamental challenge of utilizing the inherent elastic properties of FAM bladder materials as a control and efficiency advantage in actuator selection and design. Additionally, while evaluating the effect of elasticity on the contraction of FAMs intended to be bundled together, it was discovered that because of the increased rate of radial strain observed in FAMs at smaller initial braid angles, the elastic stiffness has a more extreme effect on the free-strain of FAMs. This result emphasizes the need to consider the FAM design parameters in detail.

The results show that in order to maintain wide coverage of force and strain capability when the primary operating mode is in the low-force, low strain regime, using PVR bundles is more efficient than a single FAM sized to produce equivalent force and contraction. This result reflects the biomimetic structure of mammalian muscles which was the motivation for this study. Like the PVR FAM bundle, mammalian muscles have evolved such that they can perform low-force output movements repeatedly for long periods of time while still maintaining the ability to generate high-force movements when required. Smaller FAMs, when paired with a higher-threshold muscle, can, with a single applied pressure and one standard control valve, perform small, lightweight, repetitive movements, like walking, with higher efficiency than a single FAM (SEMU). However, if the desire is to generate higher forces more frequently, efficiency in the low-force regime will be sacrificed. This leads to a relationship between the fraction of time the system spends in each operating condition on the optimal actuator choice. Based on the results of this study, passive variable recruitment bundles are both feasible and preferable if utilized in the correct manner for systems that require primarily low force and displacement motion with occasional bursts of high intensity actuation.

CHAPTER IV

Electrohydraulic Model of Various FAM Recruitment Methodologies (Submitted for publication (June 2018) in *Smart Materials and Structures)*

a) *Introduction to Recruitment Methodology and Pressurization System Study*

This study aims to understand the efficiency and bandwidth implications of active variable recruitment artificial muscles in a fully coupled electrohydraulic system including the motor, pump, and accumulator dynamics. Studies of variable recruitment artificial muscles to date have only considered the actuators downstream of the hydraulic pressure source and have ignored the coupling and system design implications of the complete system. Furthermore, this study develops a steady-state analytic solution for determining the maximum operating frequency, referred to as bandwidth, of the coupled electrohydraulic system. The results presented have implications on the necessary design considerations for each recruitment method when implementing FAMs in soft-robots, prosthetics, and out-of-laboratory rehabilitation devices.

b) *Modeling and Design Parameters*

This section includes the modeling and system parameters needed for the performance of this chapter. Some equations are duplicated from previous chapters, but are not re-derived here.

i. FAM and variable recruitment subsystem

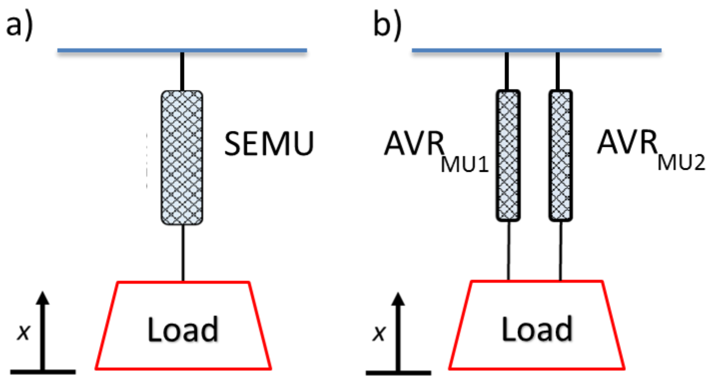

Figure 34: Actuator arrangement for a) SEMU, and b) AVR bundle.

Figure 34 shows the actuator arrangements considered: a single equivalent motor unit (SEMU) and an AVR bundle with two motor units, MU1 and MU2. The AVR bundle has two recruitment levels (RL's), RL 1 in which only MU1 is active and RL2 in which both MU1 and MU2 are active. The ideal FAM output force, $F_{m,ideal}$, has been well established and is based on the virtual work model [11] as

$$F_{m,ideal} = P_{app}\pi R_0^{\,2}\left[a(1-\varepsilon)^2 - b\right] \tag{48}$$

$$a = \frac{3}{tan^2\alpha_0} \tag{49}$$

$$b = \frac{1}{sin^2\alpha_0} \tag{50}$$

where ε is the non-dimensional strain defined as $\varepsilon = \dfrac{x}{L_0}$ L_0 is the initial muscle length and x is the contraction of the FAM. Other key parameters are the initial braid angle, α_o, initial braid radius, R_o, and applied pressure by the working fluid, P_{app}. This ideal model does not take into account nonlinearities inherent in the elastic bladder and excludes the various methods that have been shown to improve modeling accuracy [8-12]. The model accounting for these nonlinearities considered here was developed by Sangain, et al.[24] and was previously used and validated in the analysis of one type of FAM variable recruitment [23]. It accounts for the elasticity of the bladder material by introducing the idea of effective pressure, P_{eff}, which is defined as

$$P_{eff} = P_{app} - P_{el}\,, \tag{51}$$

where P_{el} is non-recoverable energy storage [23] caused by bladder elasticity; and is analytically derived as

$$P_{el} = P_{th} + \frac{E_b t_0}{R_0 \sin\alpha_0}\left[\left(1-\left(1-\frac{x}{L_0}\right)^2 \cos^2\alpha_0\right)^{1/2} - \sin\alpha_0\right] \tag{52}$$

where E_b is the elastice modulus of the bladder and t_0 is the initial thickness of the bladder. The threshold pressure, P_{th}, the minimum pressure required to overcome bladder elasticity, marking the onset of radial expansion and tensile force application [9, 12]. Threshold pressure is generally determined through empirical FAM testing and is defined here by the same method used by Pilsbury, et al. [9]. Equations 4 and 5 combine with equation 1 [24] to yield

$$F_m = P_{eff}\pi R_0^{\,2}\left[a\left(1-\frac{x}{L_0}\right)^2 - b\right] \tag{53}$$

Since the purpose of this study is to compare the effect of different recruitment methodologies on the operation and design of the electrohydraulic system pressurizing the working fluid for the actuation, it is necessary to ensure that all recruitment methodologies are comparable. To do this, we define our active variable recruitment bundle and the single equivalent motor unit (SEMU) as having the same maximum applied (or blocked force), F_{bl}, and free contraction, x_{max}, at the maximum applied pressure, $P_{max,app}$. Since elasticity affects free strain [7, 8, 13, 23], it is necessary to solve equation 6 for r_0 such that x_{max} for the bundles and

SEMU are equivalent. This is performed as described in Chapman and Bryant [23] and the resulting parameters for the FAMs under consideration are shown in Table 6**.** Figure 35 displays the output force, normalized by blocked force, and the AVR bundle force at the transition between RL1 and RL2. This transition occurs at 90% of $P_{max,app}$ in order to ensure smooth spline engagement of RL2 as describe in Meller, et al. [19]. The actuator hydraulic flow schematics for the cases considered are shown in figure 36.

Table 6: FAM Design Parameters

	SEMU	**AVR (MU1 & MU2)**
L_0 (m)	0.1	0.1
R_0 (mm)	6	4.25
P_{th} (Pa)	0	0
E_b (MPa)	0.9	0.9
t_0 (mm)	1	1
α_0 (deg)	30	30

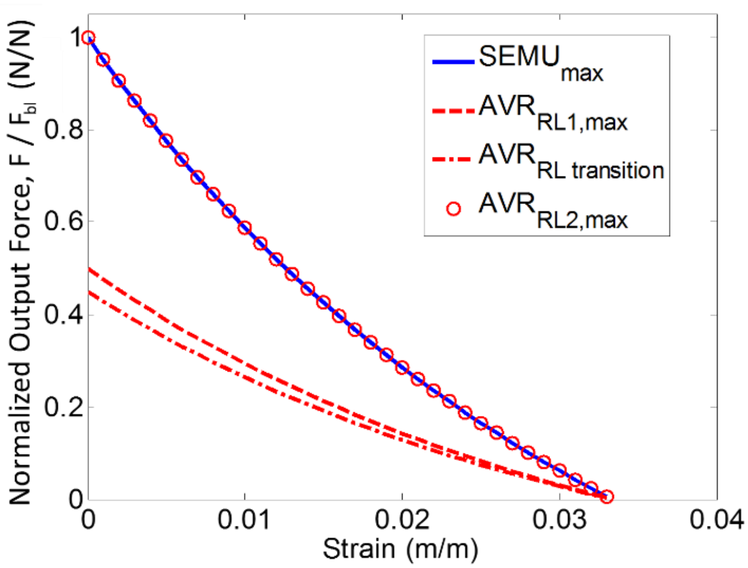

Figure 35: Normalized output force vs Actuator Strain for SEMU and AVR Bundle.

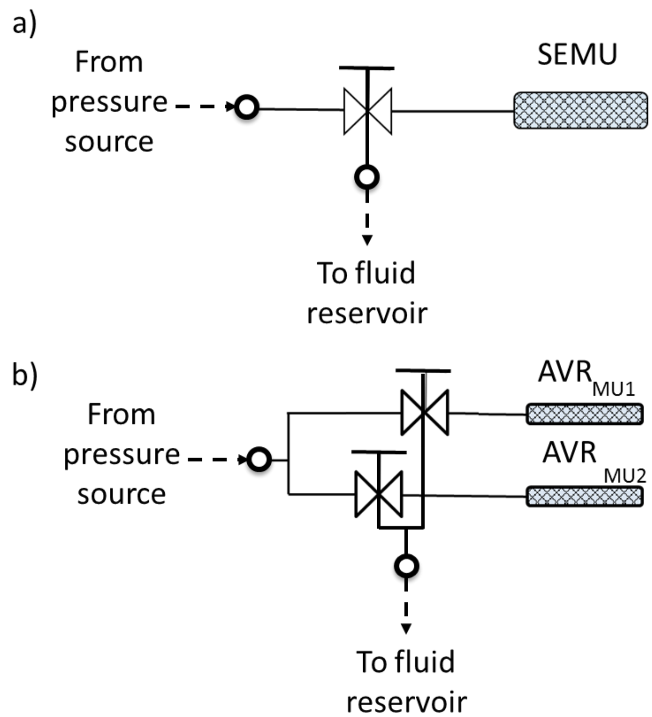

Figure 36: Hydraulic flow diagram for a) SEMU and b) AVR.

Figure 36 illustrates that this study utilizes throttle valves to control the applied pressure to each FAM motor unit. The SEMU is operated by a single control valve while the AVR bundle consists of one control valve for each motor unit (MU1 and MU2). The working fluid volume consumed by a contracted FAM, V_m has been shown [11] to be

$$V_m = \pi R_0^{\,2} L_0 \left[\frac{\left(1 - \frac{x}{L_0}\right)}{\sin^2 \alpha_0} - \frac{\left(1 - \frac{x}{L_0}\right)^3}{\tan^2 \alpha_0} - 1 \right] \tag{54}$$

and the volumetric flowrate from the accumulator into each activated FAM, $\dot{V}_m$, is [15]

$$\dot{V}_m = \pi R_0^{\ 2} L_0 \left[\frac{\left(-\frac{1}{L_0}\right)}{\sin^2 \alpha_0} + \frac{3\left(\frac{1}{L_0}\right)\left(1-\frac{x}{L_0}\right)^2}{\tan^2 \alpha_0} \right] \dot{x} \tag{55}$$

where $\dot{x}$ is the time rate of contraction of the bundle. Two hydraulic pressurization systems will be considered, both include a gas-charged accumulator for hydraulic energy storage. The accumulator pressure is a function of V_m and the volume added to the accumulator by the pump, V_p as governed by the ideal gas law with a constant temperature approximation.

$$P_{acc} = \frac{P_{acc,initial} V_{acc,initial}}{V_{acc,initial} + V_m - V_p} \tag{56}$$

P_{acc} is the accumulator pressure and $P_{acc,initial}$, and $V_{acc,initial}$ are the initial accumulator pressure and volume, respectively. Two hydraulic pressurization methods will be studied; both are detailed in section c. In the first, a bypass valve maintains the pressure of the accumulator at or below its initial set pressure and the pump operates continuously. In the second scheme, the motor is started at the beginning of each contraction and stops upon accumulator pressure being restored to initial pressure.

ii. Electrical subsystem

The electrical system considered is driven by a brushed DC motor with constant applied voltage during operation [15]. First principles analysis of such a system [26] yields the motor-pump rotational acceleration, $\ddot{\theta}$ **,** as

$$\ddot{\theta} = \frac{k_e I - B_m \dot{\theta} - \tau_p - \tau_{fric}}{J} \tag{57}$$

where τ_{fric} is motor friction, J is the motor's moment of inertia, k_e is motor's torque constant**,** and B_m is frictional damping coefficient. The rate of change of current, $\dot{I}$ **,** can be shown to be

$$\dot{I} = \frac{V_{motor} - k_b\dot{\theta} - IR}{L} \tag{58}$$

where k_b is the back electro-magnetic force constant, L is motor inductance and motor-pump impeller torque, τ_p, is described by

$$\tau_p = \frac{P_{acc}D}{2\pi}. \tag{59}$$

The initial motor considered is a 5W Maxon [27] DC Brushed motor with the properties shown in Table 7.

Table 7: Motor operating characteristics

V_{motor} (V)	18
No-load speed (RPM)	9970
No-Load Current (A)	10.4 e -3
k_b (*Nm/A*)	17.1e-3
k_e (V-sec/radian)	17.1e-3
B_m (Nm/(rad/s))	1.74e-7
J (kg-m^2)	4.2e-7
R (Ω)	13.8
L (H)	0.89e-3
D(mL/rev)	0.021

The pump displacement selected for this study was selected such that, for the maximum accumulator pressure, 550 kPa, the motor operates at its highest rated efficiency. This speed is calculated using steady state analysis of equations 57-59 and is dependent of the parameters in Table 7. Section d considers the effects of pump displacement changes on both performance and efficiency, but for all other cases, the pump displacement is as shown in Table 7.

c) Electrohydraulic Subsystems and Fully Coupled Dynamic Simulations

Increasing the number of operating cycles has been shown in some cases to increase the efficiency of a single-FAM actuated system by averaging out the starting-current present in each cycle [15]. One of the primary aspects of this study is to determine if this holds true when using variable recruitment, or if it is preferred to start and stop the motor as needed throughout operation. To this end, we perform analyses at steady-state operating condition, which represents the peak efficiency possible for a system with a continuously operating pump and motor; these will be referred to as 'continuous pump operation' analyses. Additionally, a series of similar analyses are performed during which the pump and motor are started at the beginning of each cycle and stopped when the system returns to initial pressure; these are referred to as 'intermittent pump operation' analyses. Multiple load cases and actuation frequencies (and therefore recruitment level requirements) are considered for each activation method in Sections d and e in order to determine system performance, as indicated by amplitude-bandwidth limits, and system efficiency. This section details the differences between these two electrohydraulic subsystems and shows their response to a dynamic load case. The prescribed path and loading for this load case and the these analyses which follow are

$$x(t) = \frac{x_{\max}}{2}\cos(\omega \mathrm{t} - \pi) + \frac{x_{\max}}{2}, \text{ and} \tag{60}$$

$$m\ddot{x} = F_m - mg \tag{61}$$

where load, *mg*, contraction length, $x_{\max}$, and frequency, ω, are prescribed. The required force and applied pressure are determined depending on the specific recruitment methodology (AVR or SEMU).

i. *Continuously pump operation*

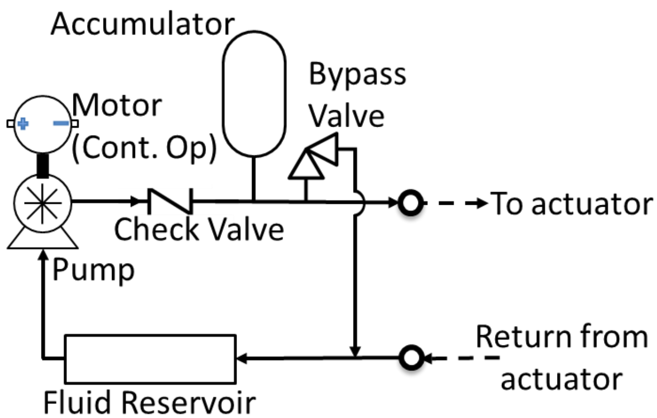

Figure 37: Electrohydraulic system diagram for continuous pump operation.

In the first electrohydraulic system considered, shown in figure 37, a pressure relief valve maintains accumulator pressure at a value less than or equal to 550 kPa and the motor and pump are in continuous operation. Initial conditions for this system are shown in Table 8 and were calculated using equations 57-59 and the motor operating specifications in Table 7.

Table 8: Continuous operation I/Cs

x (m)	0
$\ddot{x}$(m/s^2)	0
Current (A)	0.116
$\dot{\theta}$(rad/s)	958
P_{accum}(kPa)	550

The simulated system response history for the SEMU and the AVR bundle with continuous pump operation are shown in figures 38 and 39 for a load of mg/F_{bl} = 0.24. This load is a representative case as it requires recruitment level transitions in the variable recruitment bundle and therefore captures changes in the electrical power draw induced by the different recruitment methodologies.

The operating cycle frequency shown is 0.25 Hz and the amplitude is that of 18% strain; selected such that the operating effects can be seen in each case shown.

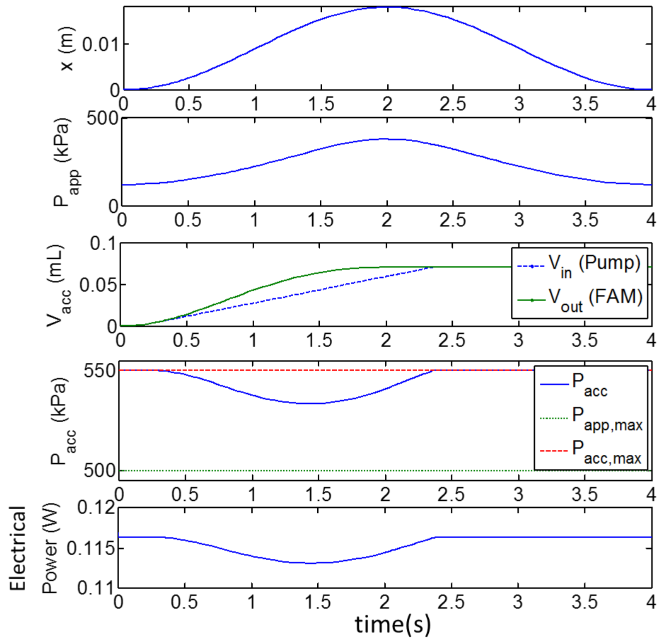

Figure 38: System response to prescribed path with frequency = 0.25 Hz, x_{max} = 0.018 m, and mg/F_{bl} = 0.24 for SEMU with continuous pump operation.

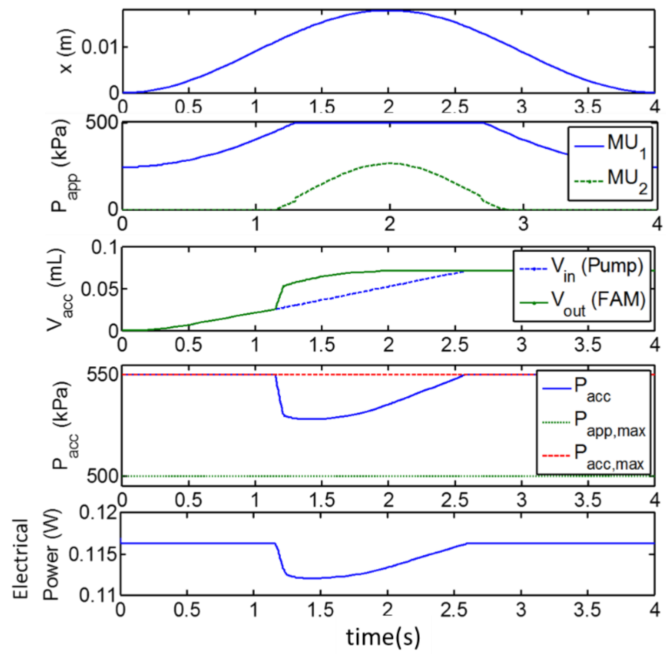

Figure 39: System response to prescribed path frequency = 0.25 Hz, x_{max} = 0.018 m, and mg/F_{bl} = 0.24 for AVR bundle with continuous pump operation. Note the sharp increase in working volume consumption rate (bottom) when AVR motor unit 2 is activated at 90% of max applied pressure.

As shown in figures 38 and 39, the accumulator pressure remains at 550 kPa until the volumetric flowrate out of the accumulator and into the muscles is greater than the volumetric flowrate into the accumulator from the pump. The pump flowrate is affected by the accumulator pressure, as indicated by equations 57-59. The AVR bundle shows a rapid increase in volumetric flowrate as the second motor unit is rapidly brought to pressure through filling and the first RL pressure simultaneously increases to its maximum. Due to the high differential pressure, this occurs nearly instantaneously and, of note is that the AVR bundle consumes the same volume as the SEMU when in RL2. In comparing these two system response plots, several trends are evident. The first, is that the AVR bundle consumes less fluid volume until RL1 begins to transition to RL2. The RL transition sharply increases the rate of working fluid volume consumption, which sharply drops the accumulator pressure. This decreases pump-torque, which increases the motor operating speed and decreases power draw rapidly.

ii. Intermittent pump operation

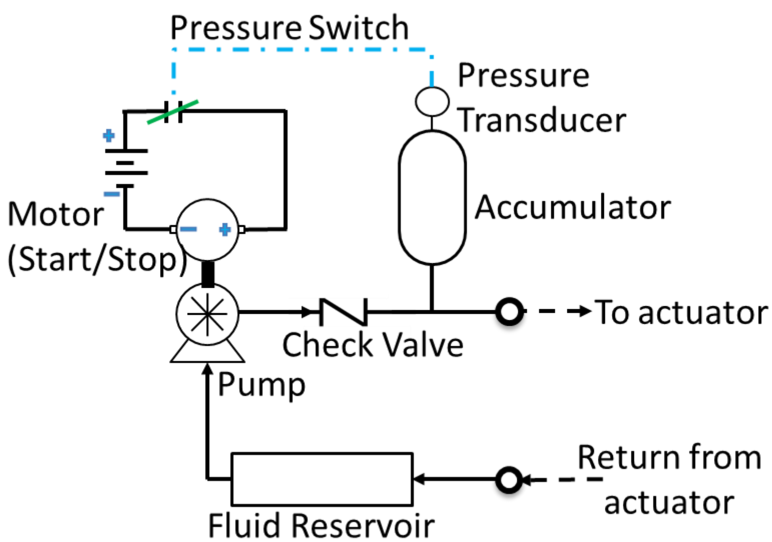

Figure 40: Electrohydraulic system diagram for Intermittent pump operation.

The second hydraulic system considered, illustrated in figure 40, has the same operating pressure range as that considered in the previous section but uses a pressure transducer attached to the accumulator to control the operation of the motor and pump. The motor starts at the beginning of each operation cycle and is turned off when the accumulator is restored to original pressure, 550 kPa. In this case, the high current draw of starting the motor must be overcome for each cycle, but the system is not consuming electrical power once the accumulator is restored to its initial conditions. Initial conditions for this operating system are shown in Table 9.

Table 9: Intermittent motor operation I/Cs

x (m)	0
$\ddot{x}$(m/s^2)	0
Current (A)	0
$\dot{\theta}$(rad/s)	0
P_{accum}(kPa)	550

The same loads, amplitudes, and frequencies are simulated for this hydraulic system as in the continuous pump operation system. The results of the SEMU and the PVR and AVR bundles are shown in figures 8 and 9.

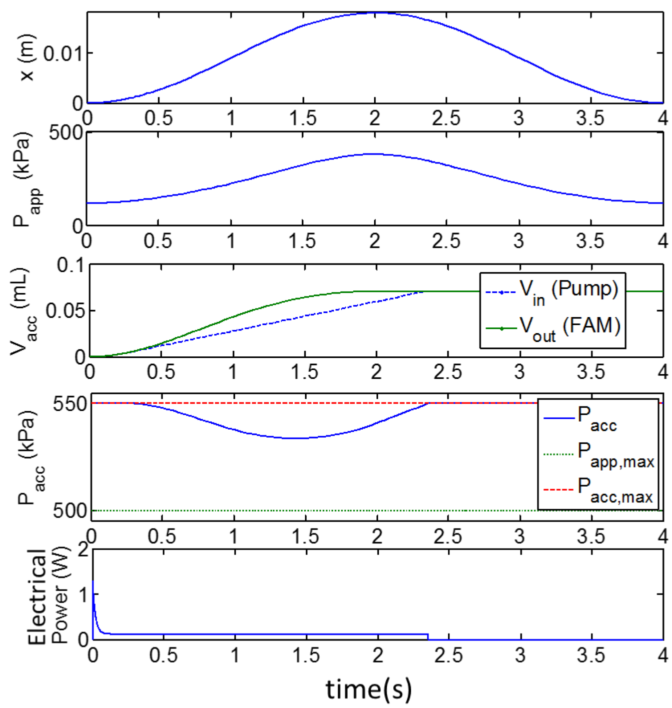

Figure 41: System response for a prescribed path with intermittent pump operation for a SEMU. Note the power-consumption drops to zero after the accumulator has been restored to 550 kPa.

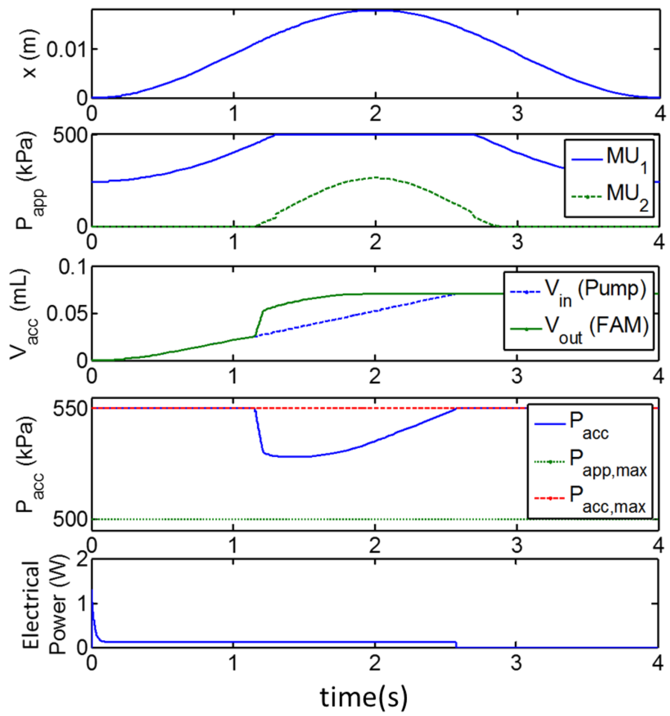

Figure 42: System response for a prescribed path with intermittent pump operation for an AVR bundle. Note the power-consumption drops to zero after the accumulator has been restored to 550 kPa.

As shown in figures 41 and 42, there is a large starting current draw and therefore power spike at the beginning of each cycle. Power then levels out and is approximately steady during muscle contraction. As the SEMU or AVR bundle contract, fluid volume flows from the accumulator and pressure in the accumulator drops. As occurred during the continuous pump operation system response, the AVR bundle has a sharp increase in volumetric flowrate when the second recruitment level is activated. As prescribed, when the accumulator pressure reaches its initial value, the motor stops, and power draw drops to 0 W for the remainder of the cycle. The system performance implications of the difference between these two methods will be discussed in sections d and e.

d) System Efficiency and Bandwidth

i. Efficiency and bandwidth definitions and analytic solution

Since we are performing cyclic operations of prescribed contraction, frequency, and load, and we're only interested in the work done by the FAM on the load, we define system output such that is defined as work done by the FAMs so that when $\dot{x}$ is positive, the FAMs are doing work. Actuator, and therefore system output work is, therefore

$$\Delta U_{actuator} = \int F_m dx \tag{62}$$

where F_m is based on the load as shown in equation 61. The energy consumed by the system is defined as

$$\Delta U_{motor} = \int P_{motor} dt \tag{63}$$

where $P_{motor} = IV_{motor}$, System efficiency is defined as

$$\eta_{sys} = \frac{\Delta U_{actuator}}{\Delta U_{motor}} \tag{64}$$

Bandwidth limit is defined here as the maximum frequency at which a given system can maintain FAM or bundle contraction to a desired $x_{\max}$ as defined **in equation 60**. In order to determine the maximum operating bandwidth for a given system, we must ensure two things: 1) that the FAM or bundle is able to apply sufficient force to generate the prescribed path with the given load, and 2) that the hydraulic system is capable of restoring accumulator pressure before the end of the cycle. For the first, we analyze equations 53, 60, and 61 and, solving them simultaneously come to

$$\omega_{\max,force} = \sqrt{2\left(\left[P_{eff,\max}\pi R_0^2\left(a\left(1-\frac{x_{\max}}{L_0}\right)^2-b\right)\Big/m\right]-g\right)\Big/x_{\max}} \tag{65}$$

where $P_{eff,\max}$ is the FAM effective pressure at $P_{\max,app}$. Equation 65 yields the force-limited frequency performance capability for a given amplitude, $x_{\max}$, FAM, and load condition.

The next limitation for operation is based on the ability of the coupled electrohydraulic system to restore accumulator pressure by the end of the actuation cycle. In order to do this, the working fluid moved to the accumulator by the pump during the cycle must be greater than or equal to the volume of the working fluid consumed by the FAM or bundle during the cycle. Solving for this relationship using the equation 54 and neglecting transient characteristics in equations 57-59, we see that a given electrohydraulic system will have a bandwidth limit of

$$\omega_{\max,\text{flow}} = D\dot{\theta}_{NL}\left(1-\frac{DP_{acc,\max}}{2\pi\tau_s}\right) \Bigg/ \pi R_0^{\ 2} L_0\left(\frac{\left(1-(x_{\max}/L_0)\right)}{\sin^2\alpha_0}-\frac{\left(1-(x_{\max}/L_0)\right)^3}{\tan^2\alpha_0}-1\right) \qquad (66)$$

where $\dot{\theta}_{NL}$ is the no-load speed of the motor in rad/s, τ_s is the motor's stall torque, and $P_{acc,\max}$ is the maximum accumulator pressure of the system. As shown in equation 66, increasing the size of the FAM or bundle decreases the max operating frequency of the system at a given amplitude ($x_{\max}$). Also of note is that changing the pump (manifested through *D*), the motor (manifested through τ_s and $\dot{\theta}_{NL}$), or the hydraulic system operating pressure (manifested through $P_{acc,\max}$) has an impact on the relationship between $x_{\max}$ and $\omega_{\max}$. Equations 65 and 66 yield a steady-state analytic solution which predicts the maximum bandwidth for an electrohydraulic system with FAM actuators. Figure 43 shows the output curves of these two equations, the FAM design parameters in Table 6, and the motor and pump characteristics shown in Table 7**.**

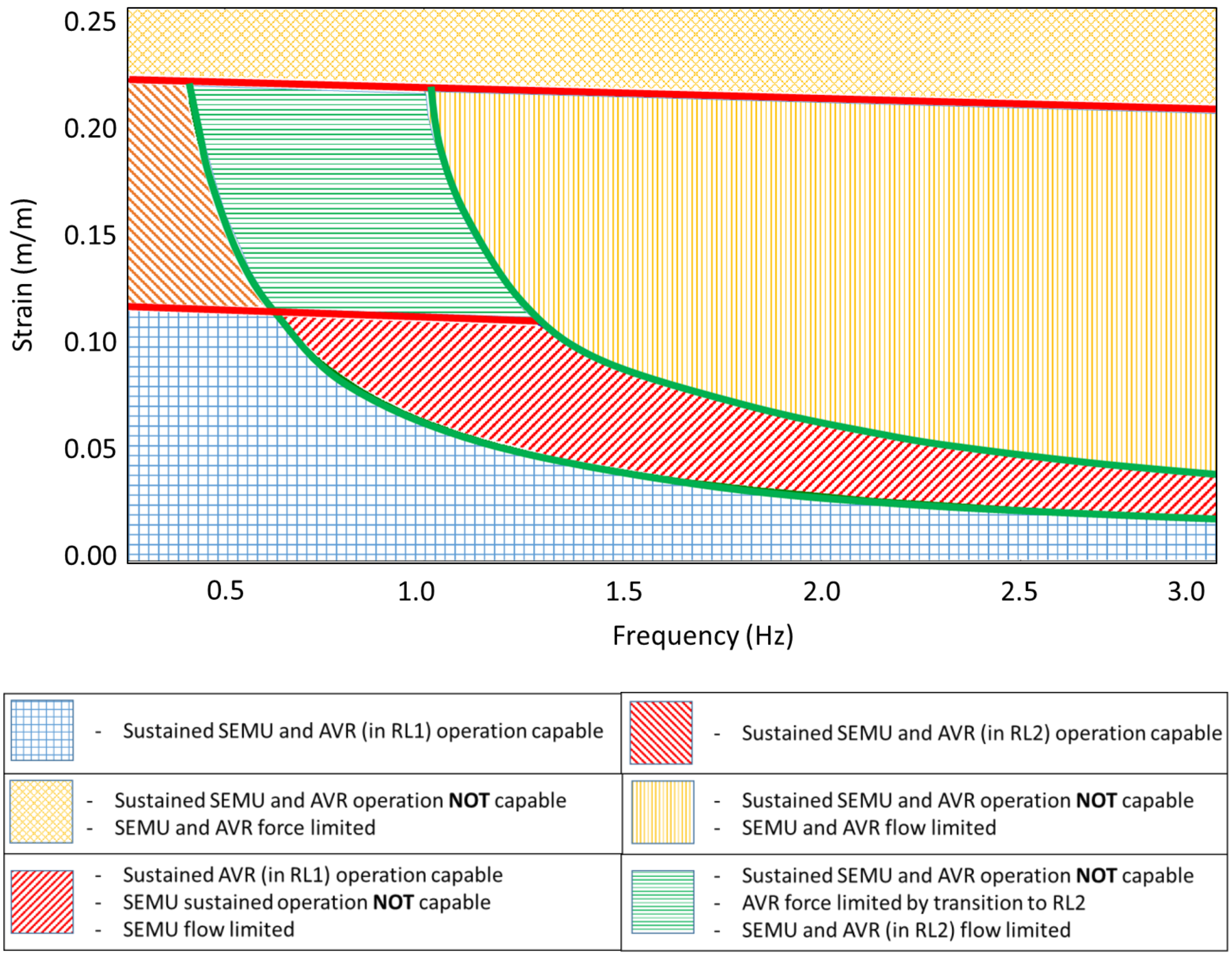

Figure 43: System bandwidth limits and operating region explanations for $mg/F_{bl} = 0.24$.

Figure 10 provides insight into the various operating regions of a given motor-pump-FAM assembly. These calculated bandwidth limitations from equations 18 and 19 are overlaid with the bandwidth limits found from the dynamic simulation results found in Section c in figure 11.

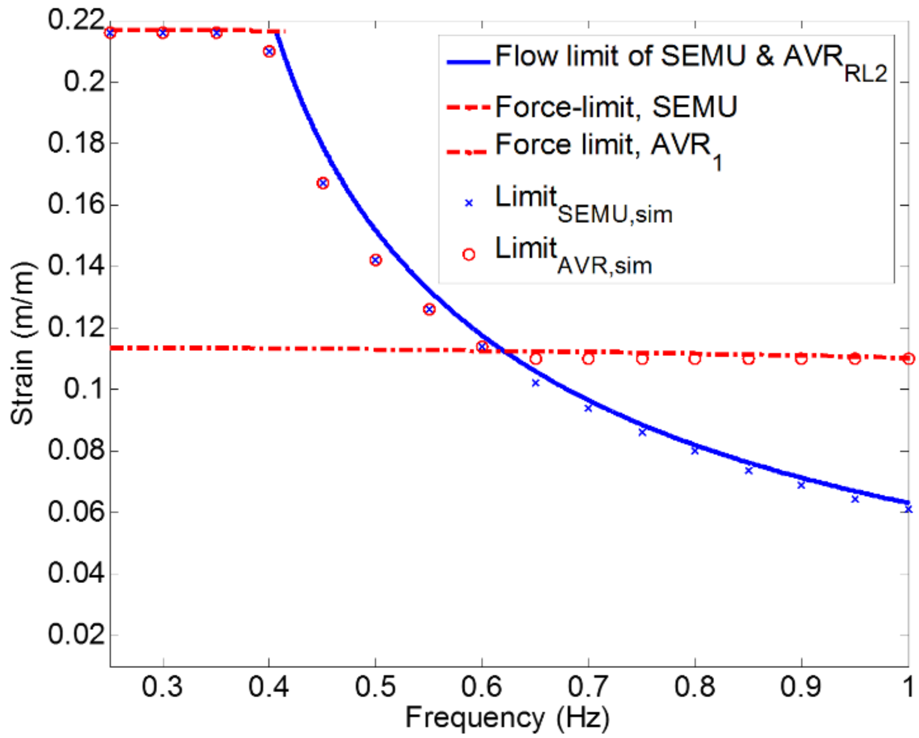

Figure 44: Steady-state analytical solution overlaid with dynamic simulation results for $mg/F_{bl} = 0.24$.

As seen in Figure 44, the limits calculated through the simulated system response plots shown in Section c closely follow the theoretical upper-bounds calculated by equations 65 and 66. The small differences (<0.1% strain) are due to the electrical and mechanical transients present as shown in the simulated system response studies shown in Section c. The data points shown are for both the continuous and intermittent systems; the difference in bandwidth limit for the cases considered here is negligible (<0.001% difference). Also of note, is that above ~0.6 Hz, the AVR bundle has an improved maximum strain over the SEMU at the same frequency. This is due to the AVR bundle, when operating in its lowest recruitment level (RL1), consumes at most half the working fluid volume of the SEMU. Because of this, the AVR bundle is limited by the maximum force capability in RL1 rather than by the hydraulic system's ability to maintain accumulator pressure. Figure 45 shows the bandwidth-strain limits for a SEMU and an AVR bundle without any extraneous curves.

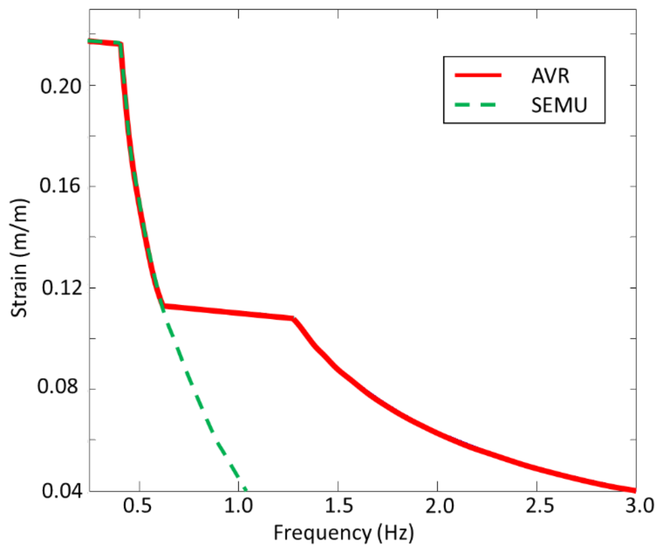

Figure 45: SEMU and AVR Bundle operating limits for $mg/F_{bl} = 0.24$. Note that the AVR bundle can operate in RL1 at much higher bandwidths than the SEMU.

So, at lower frequencies, there is no notable difference in bandwidth limit between SEMU and AVR bundles, but at higher frequencies, the AVR bundle allows the same hydraulic system to sustain operation at higher frequencies and amplitudes.

ii. Effects of pump displacement

The previous cases considered were performed with a constant pump displacement. This pump displacement was selected such that, when the accumulator pressure is 550 kPa, the motor is operating with the torque and speed which yields its highest efficiency based on the motor characteristics in Table 7**.** In this section, we consider different pump displacements to see their effect on bandwidth and efficiency for both the steady-state analytic responses of SEMU's and AVR bundles. Pump displacements displayed are normalized by the maximum volume consumption of the FAMs. Pump displacements are swept for three amplitudes: 25% (ε= 0.054), 50% (ε= 0.108), and 75% (ε= 0.162) of the maximum quasistatic contraction (ε= 0.216) of a

SEMU and n AVR bundle with a representative load (mg/F_{bl}=0.24). The results of changing pump displacement on both maximum bandwidth and efficiency are shown in figure 46**.**

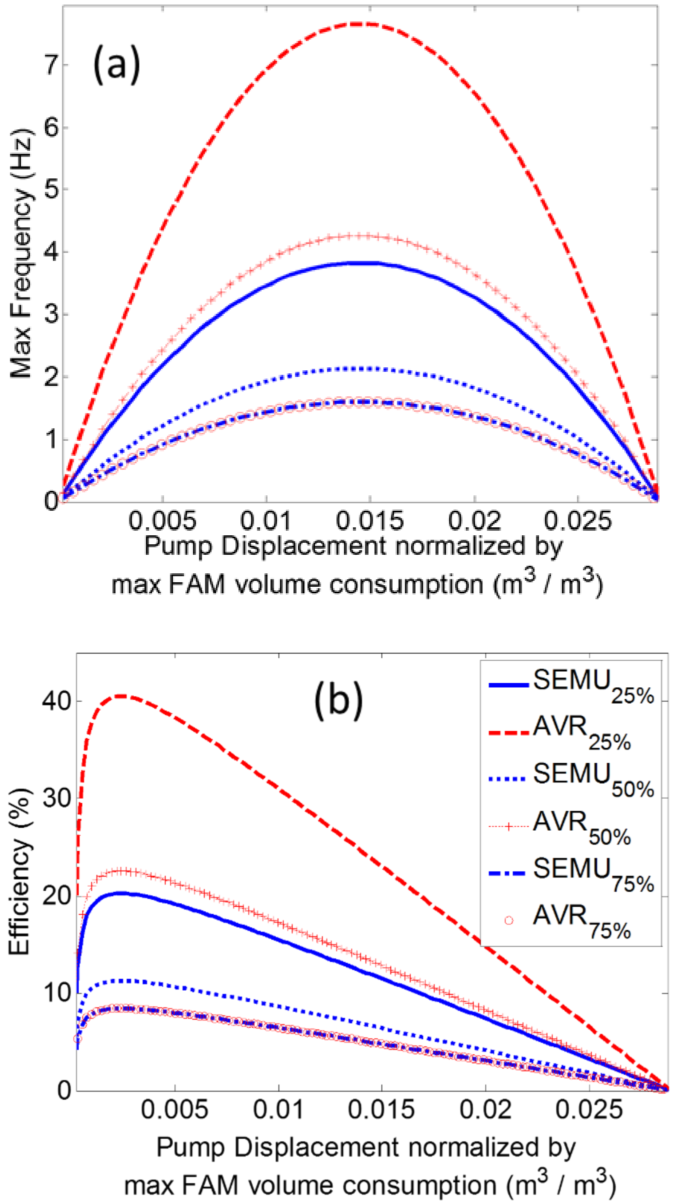

Figure 46: a) Maximum bandwidth and, b) system cycle efficiency for a variety of pump displacements for three strains and a representative load of mg/F_{bl}=0.24.

As shown in figures 46(a), increasing pump displacement increases electrohydraulic system operation bandwidth, until it reaches the peak motor power output. After the motor crests its peak output power capability, the bandwidth decreases. This is because, as shown in equation 57-59, increasing the pump displacement increases motor torque which decreases motor speed and increases current draw. This is advantageous in terms of the motor and pumps' ability to restore accumulator pressure but has a negative impact on the efficiency, as shown in figure 46(b) which shows the effect of this pump displacement on efficiency. These results clearly indicate the trade-off between bandwidth and efficiency as a function of pump displacement for a given motor. Most interesting, however, is that for the load case considered, an AVR bundle is able to sustain a higher frequency with a larger efficiency for the 50% of max-contraction case than the SEMU can sustain at the 25% of max contraction. This further emphasizes the clear performance advantage an AVR bundle has over its SEMU counterpart.

e) Combined Efficiency and Bandwidth Dynamic Simulation Results

In order to compare the AVR bundle and the SEMU within each of the hydraulic operating systems considered, a 0.5-1.0 Hz operating frequency was considered for three load conditions. A dynamic response simulation is performed for each load considered, mg/F_{bl} = 0.24 and mg/F_{bl} = 0.52, and mg/F_{bl} = 0.035. The first load considered, mg/F_{bl} = 0.24 illustrates the recruitment level transition for the AVR bundle.

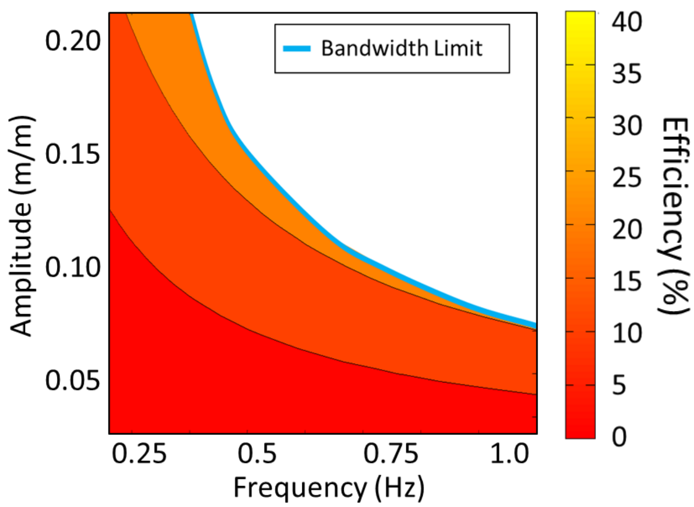

Figure 47: Efficiency and bandwidth plot for a SEMU with continuous pump operation and a load of mg/Fbl = 0.24.

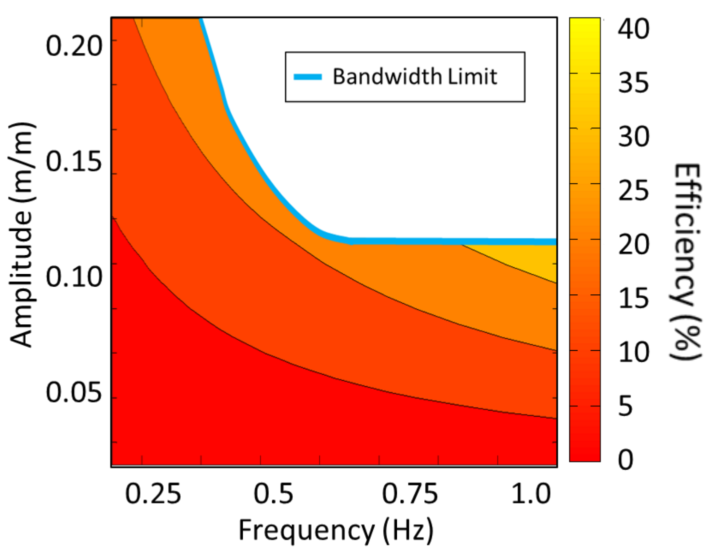

Figure 48: Efficiency and bandwidth plot for an AVR bundle with continuous pump operation and a load of mf/Fbl = 0.24.

When comparing the results of the continuously operating pump for the AVR bundle and the SEMU, in figures 47 and 48, the most striking result is that the efficiency results are nearly identical for all conditions considered. There are small differences (<1% efficiency) between the two which occur due to the slight variations in the motor power draw caused by the pressure drops. The primary reason that AVR does not show a significant advantage in this case is that the main benefit of variable recruitment, i.e. only operating the minimum number of FAMs needed, is undermined by sending excess working fluid through the bypass valves directly to the low pressure fluid reservoir. In doing so, while throttling losses are lessened in the AVR bundle case, these energy savings aren't passed on to the electrical system because the motor is always operating. Also of note is that while the SEMU has a slight efficiency advantage in the high-amplitude region, the AVR bundle is able to maintain much higher bandwidths in the low amplitude region.

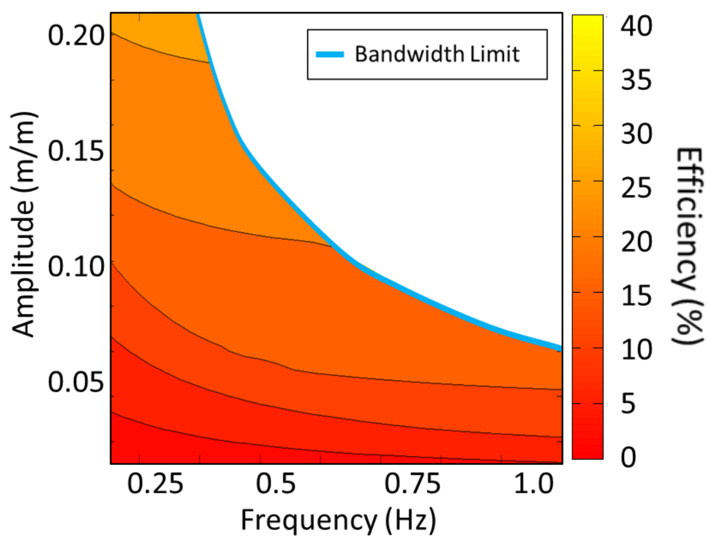

Figure 49: Efficiency and bandwidth plot for a SEMU with intermittent pump operation and a load of mg/F_{bl} = 0.24.

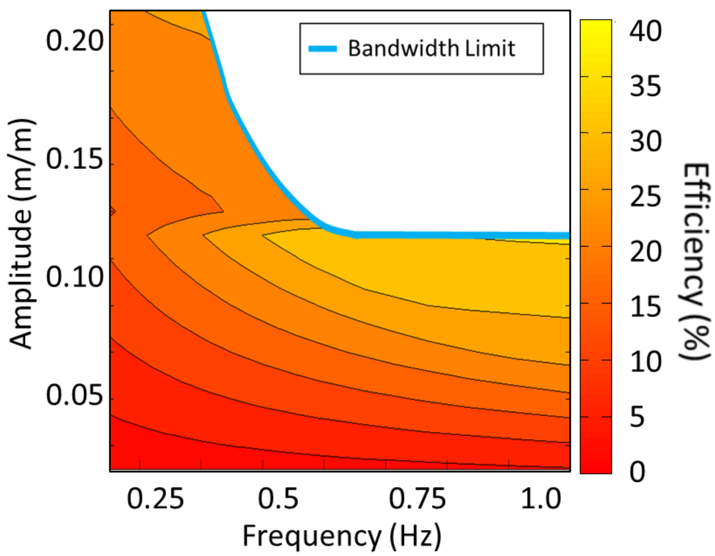

Figure 50: Efficiency and bandwidth plot for an AVR bundle with intermittent pump operation and a load of mg/Fbl = 0.24.

Figures 49 and 50 illustrate the clear advantage of powering an AVR bundle with an intermittent pump operation over all other cases. The AVR bundle, in both continuous and intermittent pump operation, has a significant advantage in low-amplitude bandwidth over its SEMU counterpart. The AVR bundle coupled with an intermittently operating motor provides an advantage over the both the SEMU operating with intermittent pump operation and the SEMU operating with continuous operation. Of additional interest is that the SEMU sees some low-frequency advantages by operating in the intermittent range, but above approximately 90% of the flow-limited bandwidth, the SEMU paired with the continuously operating pump is more efficient. Despite this, the AVR bundle with intermittent pump operation is more efficient than either of these systems. This is because using an intermittently operating motor allows the advantage of variable recruitment, lower volume consumption, to be transmitted to the electrical system.

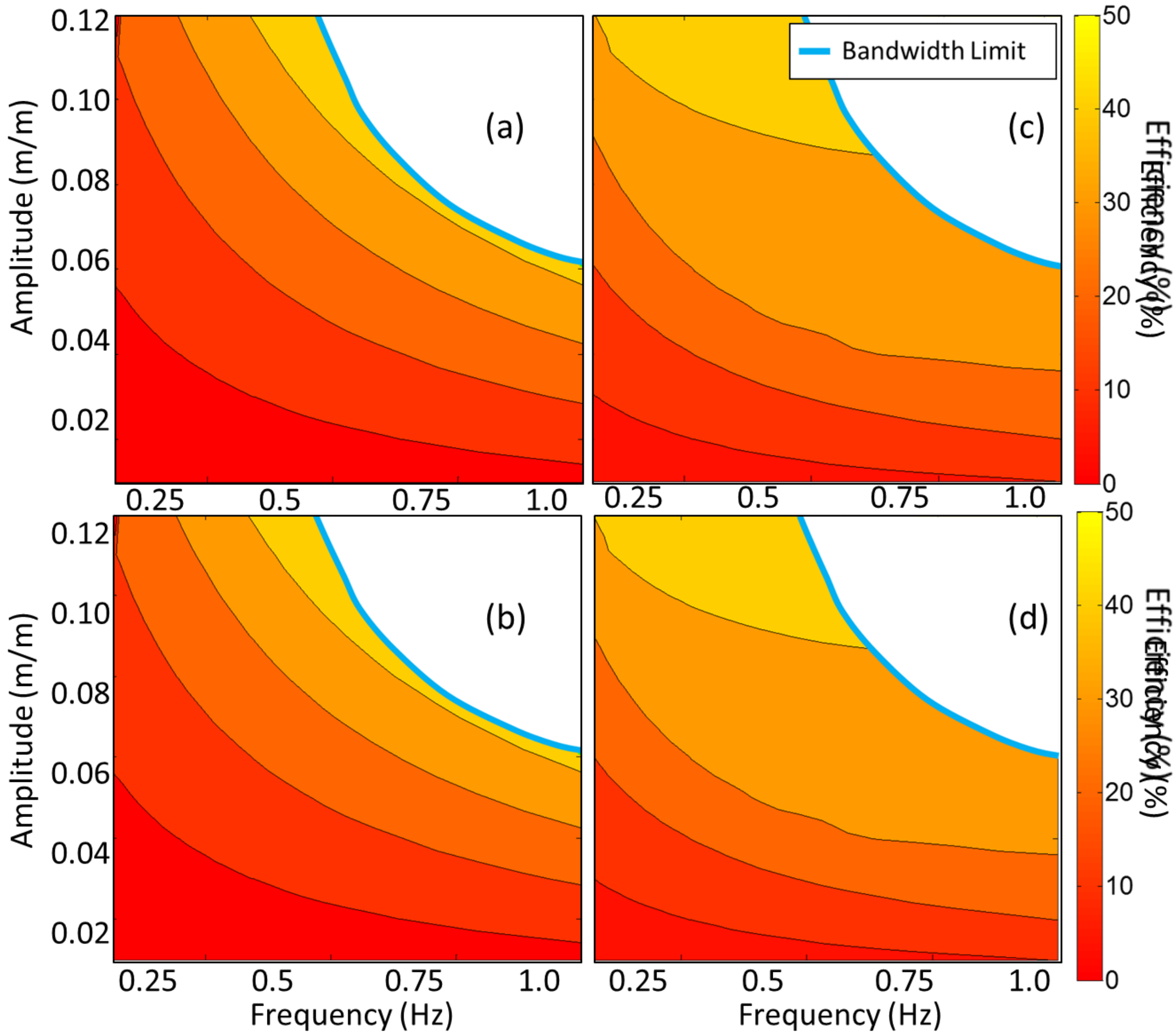

Figure 51: Bandwidth and efficiency dynamic simulation results for a load of mg/F_{bl}=0.54 for a) SEMU and b) AVR bundle with continuous pump operation, and c) SEMU and d) AVR bundle with intermittent pump operation.

Figure 51 shows the results of these same analyses for the 0.52 load, which was selected to show the effect of operating at the highest recruitment level for 100% of a cycle. Most notable in figure 51 is the absence of the horizontal portion of bandwidth limit curve which indicates the force limit of RL1 in each of the previous plots shown. This is because the AVR bundle must be fully activated at all times in order to move the heavier load. The effect this has on efficiency is that the AVR bundle and SEMU operate identically to one another in a given operating condition for both intermittent pump operation and continuous pump operation. The other notable data from Figure 51 is that the intermittent pump operation is more efficient than the continuous pump operation for the highest amplitudes. This is because the motor is always de-energized for sufficient time that the power draw is always lower than the continuous motor operation. As with the previous case, operating with a continuously operating pump is advantageous over the intermittently operating motor at frequencies where the motor is operating for more than ~90% of the cycle. In these cases, the portion of the cycle during which the motor is not consuming power is insufficient to make up for the power-spike required at the beginning of each cycle. This is the case in the low-load case, shown in figure 52, as well. This final load case, $mg/F_{bl} = 0.035$, was considered in order to determine the effect of operating in the low-load force-strain space on the system. These results are shown in figure 52. It has been well established [17-19, 23] that using variable recruitment is more efficient for light loads at the actuator level due to a decreases in both working fluid consumption and throttling losses. This actuator efficiency advantage is manifested in figure 52 by the large difference in bandwidth capability between the SEMU and AVR bundles. This low-load case demonstrates most clearly the advantages of AVR in terms of bandwidth because, in a low-load operating scheme, the second recruitment level isn't activated and, therefore, the AVR bundle has 50% of the volume consumption of the SEMU. As before, the combination of activation method and motor operation scheme are influential in the efficiency and effectiveness of the fully coupled electrohydraulic system.

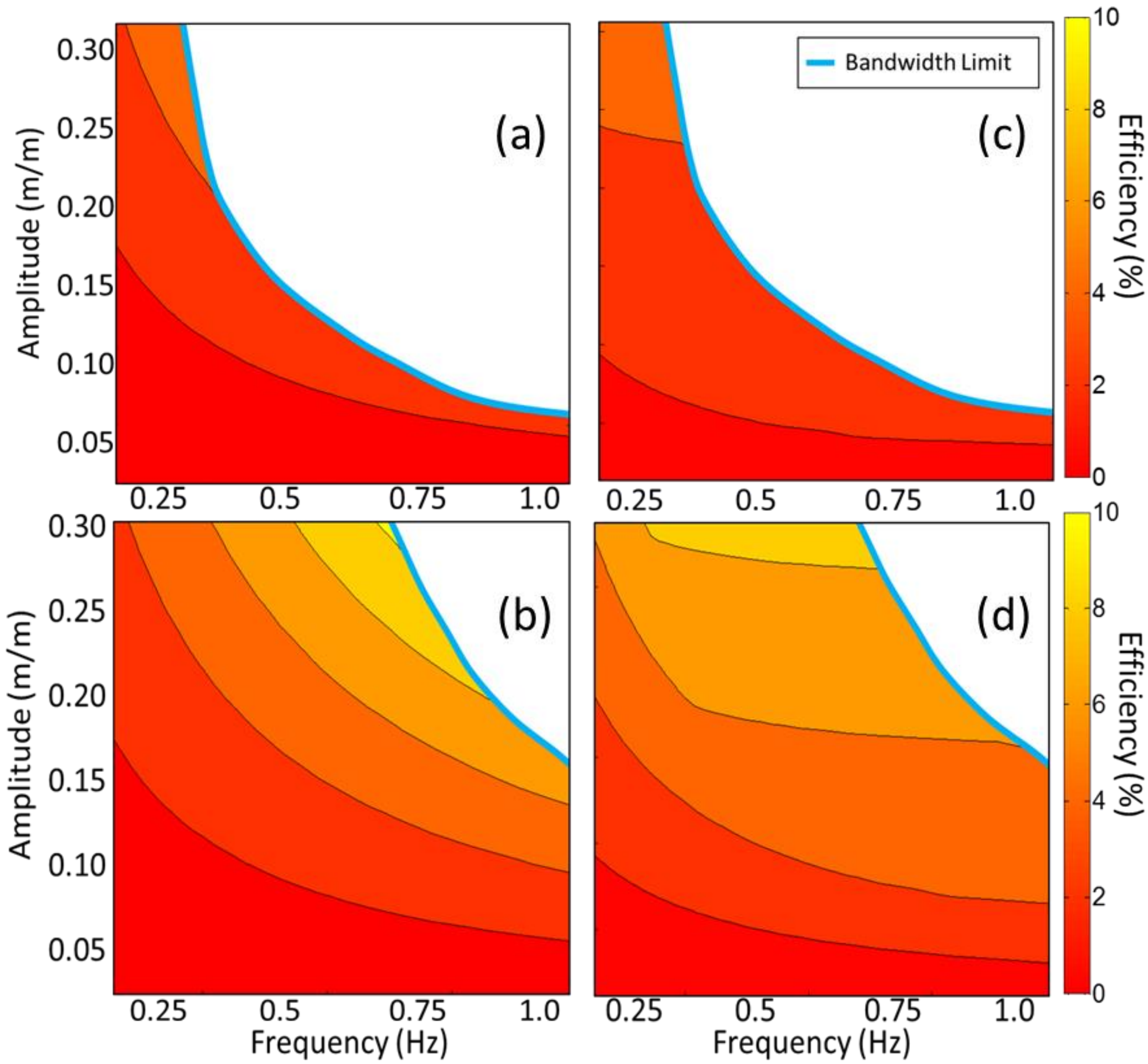

Figure 52: Bandwidth and efficiency dynamic simulation results for a load of mg/F_{bl}=0.035 for a) SEMU and b) AVR bundle with continuous pump operation, and c) SEMU and d) AVR bundle with intermittent pump operation.

f) Conclusion of Electrohydraulic System Design Study

The aim of this study was to model a fully coupled electrohydraulic system with FAM actuators and use that model to garner insight into designing a system for FAM variable recruitment methodologies. This study found, primarily, that while there are bandwidth advantages to using variable recruitment in a continuously operating pump, doing so shows no advantage over a SEMU in efficiency. This bandwidth advantage at lower amplitudes and loads is due to the decreased volume consumption of the AVR bundles when only a single recruitment level is activated. The efficiency advantage of the SEMU over the AVR in the high-amplitude and low-frequency operating regime is minimal, so even with a non-optimal motor-pump operation scheme, there are advantages in variable recruitment. However, it was found that in order take full advantage of the variable recruitment actuation paradigm, it is advantageous to operate the motor and pump to start at the beginning of each cycle and stop when accumulator pressure has been restored. This allows the efficiency advantage of variable recruitment to cascade through the hydraulic system to the electrical operating system and only use electrical energy as needed. The selection of an intermittent method increases the efficiency of AVR bundles, but negatively impacts the SEMU efficiency. It is abundantly clear from the results that the AVR bundle, when paired with intermittent pump operation, outperforms the SEMU with continuous pump operation, both in terms of efficiency and bandwidth.

Furthermore, a steady-state analytic solution for the force and flow limits for a fully coupled electrohydraulic system with FAM actuators was derived and was shown to compare favorably to the dynamic simulation results. This analytic solution takes into account FAM design parameters and kinematics as well as motor and pump dynamics. It represents the upper limit of the capability of a FAM actuated system to conduct ongoing operations and can be used to predict system performance for a variety of load-cases and system operations. It was also used to show the effect of changing pump displacement on the bandwidth and efficiency of a system. As pump displacement was adjusted such that the motor operating speed approached the motor's peak power output, bandwidth likewise reached its peak, but efficiency was decreased.

The results of this system-level study underscore that in order to fully realize the efficiency and bandwidth benefits of variable recruitment FAM actuation, not only the actuators but also the parameters and the mode of operation of the driving electrohydraulic power system must be considered and optimized for the application of interest.

CHAPTER V

Summary of Contributions and Final Conclusions

This work presents three studies which expand the current literature with respect to fluidic artificial muscles, their design and recruitment, and the system which provide their activation energy. This dissertation aims to provide insight into the design and analysis of FAM actuation systems by presenting the following novel contributions to the literature.

a) Contributions from Chapter II: Climbing Robot Study

Chapter Two presents the first fully coupled electrohydraulic system model used to generate the pressure for the fluidic artificial muscle activation. The model is validated using data from an in-house, FAM actuated climbing robot. The chapter explores the effect of FAM design parameters on the operating system efficiency using this model. It illustrates that, when system dynamics are considered, oversized actuators are less efficient, despite the actuator efficiency being higher. This is most clearly illustrated by the final case study which clearly shows that the design parameters for the highest system efficiency is never aligned with the design parameters yielding the highest actuator efficiency.

b) Contributions from Chapter III: Passive Variable Recruitment Study

Chapter Three proposes, models, and tests a novel and biomimetic variable recruitment activation method for fluidic artificial muscles. Inspired by Henneman's Size Principle, this variable recruitment strategy is biomimetic in both control strategy and operating efficiency. In low-load, low-stroke scenarios, the newly conceived passive variable recruitment FAM bundles are more efficient than their larger, single-FAM counterparts, but retain the ability to activate with the same large-load and/or stroke. Whereas less efficient when operating in these high-force regimes than the single equivalent motor units to which they were compared, PVR bundles are more efficient so long as the primary operating regime lies within low-load and stroke schemes with occasional excursions into more burdensome load cases.

c) Contributions from Chapter IV: Electrohydraulic System Design Study

Chapter Four expands upon the fully coupled electrohydraulic model explored in chapter two and provides design guidance for a system using either variable recruitment bundles or single FAMs. It explores the efficiency and performance to changes in pump displacement and actuator recruitment methodology and provides a closed form equation to determine the upper-limit on the frequency response capability of FAM recruitment levels, in both force-limited and flow-limited conditions. This novel study gives tools to design engineers to 1) size FAMs and variable recruitment bundles such that they meet the needs of the system and 2) select a motor and pump such that they complement, rather than restrict, the actuator capabilities.

d) Final Conclusions

Fluidic Artificial Muscles are a promising smart actuator technology whose force to weight ratios make them suitable for climbing and walking robots as well as rehabilitation and prosthetic devices. Presented here are novel methods of analyzing and utilizing them in a variety of operating scenarios. This work initiates the expansion of their use from the laboratory into mobile and potentially wearable technology by exploring the pressurization systems by which they are powered as well as exploring simpler and biomimetic methods to activate them and conserve energy resources. Previous research indicated that designing FAMs with optimal efficiency was sufficient, but this study shows that the whole system must be considered and provides guidance for doing so.

REFERENCES

[1] Anonymous 1958, "More Help for Polio Victims," Buckingham Post, pp. 3.

[2] Tondu, B., 2012, "Modelling of the McKibben Artificial Muscle: A Review," Journal of Intelligent Material Systems and Structures, **23**(3) pp. 225-253.

[3] Kothera, C., Jangid, M., Sirohi, J., 2009, "Experimental Characterization and Static Modeling of McKibben Actuators," Journal of Mechanical Design, **131**(9) .

[4] Meller, M. A., Bryant, M., and Garcia, E., 2014, "Reconsidering the McKibben Muscle: Energetics, Operating Fluid, and Bladder Material," Journal of Intelligent Material Systems and Structures, **25**(18) pp. 2276-2293.

[5] Bryant, M., Meller, M. A., and Garcia, E., 2014, "Variable Recruitment Fluidic Artificial Muscles: Modeling and Experiments," Smart Materials and Structures, **23**(7) pp. 1-12.

[6] Robinson, R. M., Kothera, C. S., and Wereley, N. M., 2015, "Variable Recruitment Testing of Pneumatic Artificial Muscles for Robotic Manipulators," IEEE/ASME Transactions on Mechatronics, **20**(4) pp. 1642-1652.

[7] Tiwari, R., Meller, M. A., Wajcs, K. B., 2012, "Hydraulic Artificial Muscles," Journal of Intelligent Material Systems and Structures, **23**(3) pp. 301-312.

[8] Keisuke Arikawa, and Shigeo Hirose, 2007, "Mechanical Design of Walking Machines," Philosophical Transactions of the Royal Society A: Mathematical, Physical and Engineering Sciences, **365(**1850) pp. 171-183.

[9] Provancher, W. R., Jensen-Segal, S. I., and Fehlberg, M. A., 2011, "ROCR: An Energy-Efficient Dynamic Wall-Climbing Robot," IEEE/ASME Transactions on Mechatronics, **16**(5) pp. 897-906.

[10] Carlo, M., and Metin, S., 2006, "A Biomimetic Climbing Robot Based on the Gecko," Journal of Bionic Engineering, **3**(3) pp. 115-125.

[11] Spenko, M. J., Haynes, G. C., Saunders, J. A., 2008, "Biologically Inspired Climbing with a Hexapedal Robot," Journal of Field Robotics, **25**(4-5) pp. 223-242.

[12] R. T. Pack, J. L. Christopher, and K. Kawamura, 1997, "A Rubbertuator-based structure-climbing inspection robot," Proceedings of International Conference on Robotics and Automation, Anonymous **3,** pp. 1869-1874 vol.3.

[13] Luk, B. L., Cooke, D. S., Galt, S., 2005, "Intelligent Legged Climbing Service Robot for Remote Maintenance Applications in Hazardous Environments," Robotics and Autonomous Systems, **53**(2) pp. 142-152.

[14] Sintov, A., Avramovich, T., and Shapiro, A., 2011, "Design and Motion Planning of an Autonomous Climbing Robot with Claws," Robotics and Autonomous Systems, **59**(11) pp. 1008-1019.

[15] Jenkins, T. E., Chapman, E. M., and Bryant, M., 2016, "Control approach development for variable recruitment artificial muscles," SPIE Smart Structures and Materials Nondestructive Evaluation and Health Monitoring, Anonymous International Society for Optics and Photonics, pp. 979911-979911-10.

[16] Bryant, M., Fitzgerald, J., Miller, S., 2014,"Climbing Robot Actuated by Meso-Hydraulic Artificial Muscles " Proceedings of SPIE: Active and Passive Smart Structures and Imtegrated Systems, Anonymous **SPIE: 9057,** .

[17] Tondu, B., and Lopez, P., 2000, "Modeling and Control of McKibben Artificial Muscle Robot Actuators," Ieee Control Systems Magazine, **20**(2) pp. 15-38.

[18] HP-Tech, 2016, **2016**(10/15) .

[19] Craig, J.J., 2005, "Introduction to Robotics : Mechanics and Control," Pearson Prentice Hall, Upper Saddle River, MJ, .

[20] Norton, R.L., 2004, "Design of machinery : an introduction to the synthesis and analysis of mechanisms and machines," McGraw-Hill Higher Education, Boston, .

[21] Xiang, C., Giannaccini, M. E., Theodoridis, T., 2016, "Variable Stiffness Mckibben Muscles with Hydraulic and Pneumatic Operating Modes," Advanced Robotics, **30**(13) pp. 889-899.

[22] Wang, G., Wereley, N. M., and Pillsbury, T., 2015, "Non-Linear Quasi-Static Model of Pneumatic Artificial Muscle Actuators," Journal of Intelligent Material Systems and Structures, **26**(5) pp. 541-553.

[23] Aschemann, H., and Schindele, D., 2014, "Comparison of Model-Based Approaches to the Compensation of Hysteresis in the Force Characteristic of Pneumatic Muscles," IEEE Transactions on Industrial Electronics, **61**(7) pp. 3620-3629.

[24] Shan, Y., Philen, M. P., Bakis, C. E., 2006, "Nonlinear-Elastic Finite Axisymmetric Deformation of Flexible Matrix Composite Membranes Under Internal Pressure and Axial Force," Composites Science and Technology, **66**(15) pp. 3053-3063.

[25] Sangian, D., Naficy, S., Spinks, G. M., 2015, "The Effect of Geometry and Material Properties on the Performance of a Small Hydraulic McKibben Muscle System," Sensors and Actuators A: Physical, **234**(Supplement C) pp. 150-157.

[26] Pillsbury, T., Kothera, C., and Wereley, N., 2015, "Effect of Bladder Wall Thickness on Miniature Pneumatic Artificial Muscle Performance," Bioinspiration & Biomimetics, **10**(5) pp. 055006.

[27] Ball, E., and Garcia, E., 2016, "Effects of Bladder Geometry in Pneumatic Artificial Muscles," Journal of Medical Devices, **10**(4) pp. 041001.

[28] Tondu, B., 2018, "Inflatable Actuators: An Attempt for a Common Approach Based on Treloar's Rubber Elasticity Theory," Journal of Micromechanics and Microengineering, **28**(1)

[29] Chapman, E. M., Jenkins, T. E., and Bryant, M., 2017, "Modeling and Analysis of a Meso-Hydraulic Climbing Robot with Artificial Muscle Actuation," Bioinspiration & Biomimetics, **12**(6) pp. 066010.

[30] do Nascimento, B. G., Vimieiro, C. B. S., Nagem, D. A. P., 2008, "Hip Orthosis Powered by Pneumatic Artificial Muscle: Voluntary Activation in Absence of Myoelectrical Signal," Artificial Organs, **32**(4) pp. 317-322.

[31] Tondu, B., and Lopez, P., 1997, "The McKibben Muscle and its use in Actuating Robot-Arms Showing Similarities with Human Arm Behaviour," Industrial Robot: An International Journal, **24**(6) pp. 432-439.

[32] Gordon, K. E., Sawicki, G. S., and Ferris, D. P., 2006, "Mechanical Performance of Artificial Pneumatic Muscles to Power an Ankle-Foot Orthosis," Journal of Biomechanics, **39**(10) pp. 1832-1841.

[33] Meller, M., Chipka, J., Volkov, A., 2016, "Improving Actuation Efficiency through Variable Recruitment Hydraulic McKibben Muscles: Modeling, Orderly Recruitment Control, and Experiments," Bioinspiration & Biomimetics, **11**(6) pp. 065004.

[34] Henneman, E., Somjen, G., and Carpenter, D. O., 1965, "Excitability and Inhibitability of Motoneurons of Different Sizes," Journal of Neurophysiology, **28**(3) pp. 599-620.

[35] Henneman, E., Somjen, G., and Carpenter, D. O., 1965, "Functional Significance of Cell Size in Spinal Motoneurons," J Neurophysiol, **28**(3) pp. 560-580.

[36] Chou, C., and Hannaford, B., 1994, "Static and dynamic characteristics of McKibben pneumatic artificial muscles," Robotics and Automation, 1994. Proceedings., 1994 IEEE International Conference on, Anonymous IEEE, pp. 281-286.

[37] Zajac, F. E., Neptune, R. R., and Kautz, S. A., 2003, "Biomechanics and Muscle Coordination of Human Walking: Part II: Lessons from Dynamical Simulations and Clinical Implications," Gait & Posture, **17**(1) pp. 1-17.

[38] Alkjaer, T., Simonsen, E. B., and Dyhre-Poulsen, P., 2001, "Comparison of Inverse Dynamics Calculated by Two- and Three-Dimensional Models during Walking," Gait & Posture, **13**(2) pp. 73-77.

[39] Koopman, B., Grootenboer, H. J., and De Jongh, H. J., 1995, "An Inverse Dynamics Model for the Analysis, Reconstruction and Prediction of Bipedal Walking," Journal of Biomechanics, **28**(11) pp. 1369-1376.

[40] ZAJAC, F., 1989, "Muscle and Tendon - Properties, Models, Scaling, and Application to Biomechanics and Motor Control," Critical Reviews in Biomedical Engineering, **17**(4) pp. 359-411.

[41] Kadaba, M. P., Ramakrishnan, H., and Wootten, M., 1990, "Measurement of Lower Extremity Kinematics during Level Walking," Journal of Orthopaedic Research, **8**(3) pp. 383-392.

[42] Protopapadaki, A., Drechsler, W. I., Cramp, M. C., 2007, "Hip, Knee, Ankle Kinematics and Kinetics during Stair Ascent and Descent in Healthy Young Individuals," Clinical Biomechanics, **22**(2) pp. 203-210.

[43] Roman-Liu, D., and Tokarski, T., 2005, "Upper Limb Strength in Relation to Upper Limb Posture," International Journal of Industrial Ergonomics, **35**(1) pp. 19-31.

[44] Arnold, A. S., Anderson, F. C., Pandy, M. G., 2005, "Muscular Contributions to Hip and Knee Extension during the Single Limb Stance Phase of Normal Gait: A Framework for Investigating the Causes of Crouch Gait," Journal of Biomechanics, **38**(11) pp. 2181-2189.

APPENDICES

Proceedings of the ASME 2015 Smart Materials, Adaptive Structures, and Intelligent Systems
SMASIS2015
September 21-23, 2015, Colorado Springs, Colorado, USA

SMASIS2015-8834

ELECTROHYDRAULIC MODELING OF A FLUIDIC ARTIFICIAL MUSCLE ACTUATION SYSTEM FOR ROBOT LOCOMOTION

Edward Chapman **Marc Macleod** **Matthew Bryant**
North Carolina State University
Mechanical and Aerospace Engineering
Raleigh, NC 27695, USA

ABSTRACT

Fluidic artificial muscles have the potential for a wide range of uses; from injury rehabilitation to high-powered hydraulic systems. Their modeling to date has largely been quasi-static and relied on the operator to adjust pressure so as to control force output and utilization while little work has been done to date to analyze the kinematics of the driving-systems involved in their operation. This paper establishes a combined electro-hydraulic model of a fluidic artificial muscle actuated climbing robot to establish a method for studying the relationships between muscle size, robot size and function, and system design. The study indicates a strong relationship between appropriate system component selection and not only system efficiency but individual component effectiveness. The results of the study show that robot mass, operating pressure, muscle size, and motor-pump selection have noteworthy impacts on the efficiency and thereby longevity of the robot for performing its task.

Keywords: fluidic artificial muscles, hydraulic muscle, McKibben muscles, fluid dynamics, climbing robot, wall climbing, bio-inspired, electro-hydraulic systems

1. INTRODUCTION

The objective of this work is to investigate robot architectures that utilize lightweight hydraulic power to enable efficient walking or climbing robots. Using hydraulic actuation for small climbing or walking robots is an attractive concept due to its well-established operation in industry, but has received little attention to date because the size and weight of current hydraulic systems are prohibitive. Larger hydraulic robots, such as “BigDog” [1] have received a great deal of attention due to their ability to adaptively adjust to rough terrain and maintain a stable gait. However, for smaller applications, a different approach is required for achieving peak efficiencies.
Other climbing robots are either large, like NINJA [2], or are designed specifically for inspection or surveillance and have little to no design-criteria for a change in payload. The majority of the later are actuated using small DC motors at every joint and some have tethers for power supplies to increase their operational longevity [3], [4]. There are several examples of bi-pedal inspection robots which, while effective, have no space

for payload. NINJA and BigDog both show examples of combinations of hydraulics and motors as actuators (in NINJA, the wall-attachment method is a vacuum-driven suction cup), little has been done to study options for actuation methods other than DC motors and standard piston-hydraulics. DC motors have a disadvantage to fluidic artificial muscles in their increased weight, alignment criteria, and the large current draw required for each individual short-burst of leg movement. Traditional hydraulic piston-cylinder assemblies are heavier per force output than Fluidic Artificial Muscles (FAMs) [5], sensitive to alignment, and utilize sliding seals that can leak or degrade over time.

Furthermore, preview studies largely focus on the locomotion and gait analysis for various robots vice an analysis of the efficiency and effectiveness of the system actually driving the actuation of the device itself. By maximizing the efficiency of a walking or climbing robot though a system-level analysis, it is possible to extend the operating endurance of these robots significantly.

FAMs, frequently referred to as McKibben muscles, are known for their high force to weight ratios and inherent compliance. Their construction is simple; a rubber or elastomer inner tube with an outer braid which maintains a near-cylindrical shape upon inflation of the inner tube. They are single acting in contracting and can be installed effectively without precision alignment.[6].

A recent experimental demonstration of a lightweight climbing robot utilizing FAM actuators looked at the feasibility of constructing such a robot for vertical wall-climbing applications [7]. That initial proof-of-concept climbing robot demonstrated the capability of a FAM-actuated robot; this study seeks to characterize each component of the robot systems and find an understanding of their interaction. Before building a light-weight climbing robot for practical applications, it is important to fully understand the kinematics and interdependencies that exist within the power and actuation system. These systems interact in complex ways which have large impacts on the optimized operation and efficiency of a given configuration.

To this end, a fully coupled system model has been created through which the effect of various parameters can be studied on the overall efficiency and effectiveness of the robot at climbing locomotion and carrying load. It is hypothesized that a climbing robot will operate at peak efficiency, and therefore have the most endurance, when operating with a hydro-mechanical system that has been focus-designed to accomplish a set goal and gait-speed. This requires that each part of an integrated system be analyzed and adapted toward a specific goal. The system under study includes a hydraulic power and actuation system consisting of FAM actuators coupled with a return spring, a DC motor/pump combination, an accumulator, and a low-pressure reservoir. Its goal is to gain understanding of the relationship between artificial muscles as actuators and the upstream dynamics of the electro-hydraulic system.

2. ELECTRO-HYDRAULIC SYSTEM MODEL

2.1 System Configuration

Beginning with a study of the FAM kinematics and continuing with the hydraulic actuation system to the pump-motor combination provides an understanding of the interaction of forces acting in the system. We start by considering a simple robot model. In this robot concept, a single DC motor drives a constant volume positive displacement pump to form the hydraulic power source. The output of the pump is connected to a pressure accumulator and a network of valves that direct fluid to the artificial muscle actuators. The FAMs are used as linear tensile actuators to drive the limbs of the robot. Each limb and FAM actuator pair is assumed to have identical parameters, including a general mechanical advantage factor determined by the limb kinematics. The leg design for this study involves unity mechanical advantage for the sake of emphasizing the electro-hydraulic system interaction rather than the robot design kinematics. A visual representation of the basic model is shown in **Figure 1.**

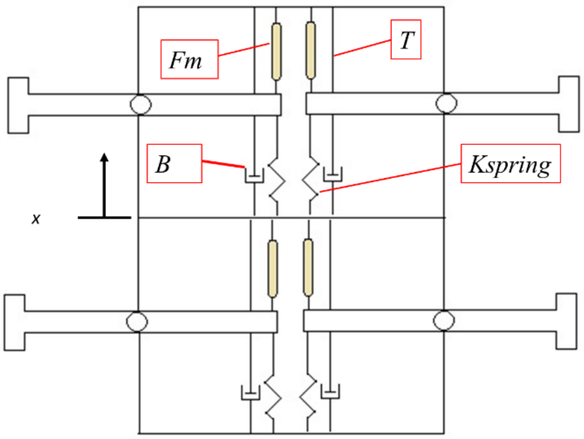

Fig. 53 Four leg robot model with actuation system elements identified.

The FAMs provide only single-acting actuation, therefore, a linear return spring is included to re-extend the muscle during depressurization. The robot achieves climbing locomotion by engaging claws, grippers, or other adhesion mechanisms with the wall on the extended limbs, then inflating the corresponding FAMs with pressurized working fluid from the accumulator and pump. This causes the actuators to contract, moving the grippers relative to the robot body and lifting the robot mass upward. Meanwhile, the previously contacted limbs disengage with the wall during the body motion, and are extended by venting their FAMs to the low pressure reservoir and allowing the return spring to elongate the muscle and raise the limbs.

2.2 FAM Actuator Modeling

First, an accurate model of FAM force-contraction behavior application was selected from the available literature and applied to the system in mind. It is important to be able to approach these equations of motion in such a way as to relate the FAM contraction to system motion. Fluidic artificial muscles are typically analyzed in terms of strain, ε, which is defined as change in muscle length divided by initial muscle length, l_o . This is true in both the Tondu [6] and Meller [8] models. By making the substitution of $\frac{x}{l_0}$ for ε, we are able to relate muscle contraction and robot leg movement and, thereby, height change with the assumption of a no-slip condition with the wall during climbing motion. The key performance-driving mechanical parameters of fludic artificial muscles are initial braid angle, α_o, initial braid radius, r_o, and P_{app}, the pressure applied to the muscle by the working fluid.

FAM output force, F_m, is modeled by Meller et al. [8] as:

$$F_m = P_{app}\pi {r_0}^2 \kappa_F \left[a\left(1 - \kappa_\varepsilon \frac{x}{l_0}\right)^2 - b\right] \tag{1}$$

where:

$$a = \frac{2}{tan^2\alpha_0} \tag{2}$$

$$b = \frac{1}{sin^2\alpha_0} \tag{3}$$

$$\kappa_F = \frac{F_{meas,max}(P)}{(\pi r_0)P_{app}(a-b)} \tag{4}$$

$$\kappa_\varepsilon = \frac{1}{\varepsilon_{meas,max}(P)}\left[1 - \frac{1}{\sqrt{3}\cos(\alpha_0)}\right] \tag{5}$$

and κ_F and κ_ε are the experimentally determined blocked-force and free-strain correction factors, respectively. $F_{meas,max}(P)$

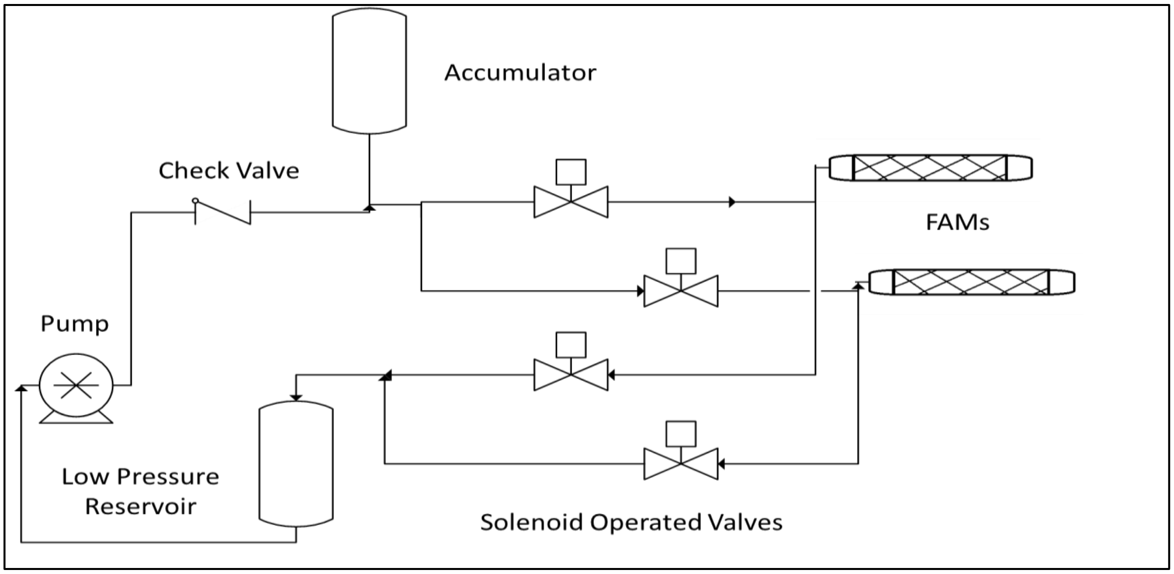

Fig. 54 Hydraulic power subsystem components for two FAM actuator system.

and $\varepsilon_{meas,max}(P)$ are the maximum measured blocked force and free-strain for a given pressure application. These correction factors are empirically determined for a specific muscle and act to correct the differences between calculated and observed force attributed to friction and elastic losses from the construction of the muscle; here we assume an idealized muscle and set $\kappa_F = \kappa_\varepsilon = 1$. The above model is predicated on the assumption that the muscles act as cylinders with changing volumes. This assumption seems to hold true for length to diameter ratios greater than 23 [8].

Volume change of the muscle, V_m, is related to the change in length, radius, and braid angle. Since change in braid angle and radius can be related in terms of a change in length, the volume change of the muscle is determined by equation (6).

$$V_m = \pi {r_0}^2 l_0 \left[\frac{\left(1 - \frac{x}{l_0}\right)}{sin^2\alpha_0} - \frac{\left(1 - \frac{x}{l_0}\right)^3}{tan^2\alpha_0} - 1 \right] \qquad (6)$$

In order to generate a time rate of change of muscle volume so that it can be used for the hydraulic system analysis, we apply the chain rule to equation (6). The result, equation (7), allows us to related volumetric flowrate out of the accumulator and into the muscle, $\dot{V}_m$, and muscle contraction rate, $\dot{x}$, which is also leg velocity. These relationships help determine fluidic motion as well as robot motion.

$$\dot{V}_m = \pi {r_0}^2 l_0 \left[\frac{\left(-\frac{1}{l_0}\right)}{sin^2\alpha_0} + \frac{3 * \left(\frac{1}{l_0}\right)\left(1 - \frac{x}{l_0}\right)^2}{tan^2\alpha_0} \right] \dot{x} \qquad (7)$$

From the equation (7), the next step was to relate FAM actuation to hydraulic flow in our broader hydraulic system. The FAM design used in the initial study has the characteristics included in **Table 1.**

Table 1. FAM parameters.

Parameter	Value
l_o	0.25 m
r_o	0.005 m
α_o	30^o

2.3 Hydraulic Subsystem Modeling

The hydraulic system modeled includes a constant volume positive displacement pump, a check valve, a gas-charged accumulator, a system of solenoid operated valves controlling flow into and out of the FAMs and a low-pressure fluid reservoir. The working fluid analyzed is water due to its relative incompressibility. A diagram of the hydraulic system can be seen in **Figure 1.** The system diagram shows two muscles in operation. One muscle is assumed to be contracting and thereby raising the robot while the other is emptying and being returned to its starting position by the return spring.

A system of equations governing the flow into and out of the accumulator and muscles were developed. The initial pressure of the accumulator, $P_{acc,i,}$, and initial accumulator gas volume, $V_{acc,i}$, were set constants. We modeled the current gas volume in the accumulator, V_{acc}, as a combination of $V_{acc,i}$, V_m, and V_p, which is the volume added to the accumulator by the pump. The ideal gas law is applied with the system assumed to be operating at constant temperature; the resultant equation for the pressure in the accumulator, P_{acc}, is found using equation (8**).**

$$P_{acc} = \frac{P_{acc,i}V_{acc,i}}{V_{acc,i} + V_m + V_p} \qquad (8)$$

Using Bernoulli's equation with a negligible fluid height difference assumption, equation (9) was derived.

$$P_{app} = \frac{P_{acc,i}V_{acc,i}}{V_{acc,i} + V_m + V_p} + \frac{\rho}{2}\left[\left(\frac{\dot{V}_m - \dot{V}_p}{A_{acc}}\right)^2 - \left(\frac{\dot{V}_m}{A_{m,i}}\right)^2\right] - h_l \qquad (9)$$

where $\dot{V}_m$ is the flowrate into the muscle through its inlet as defined in equation (7), $\dot{V}_p$ is the volumetric flowrate into the accumulator from the pump, which is related to pump speed and sizing and is expanded upon in section 2.3. Head loss, h_l, is assumed to be zero, but could be adjusted based on the valve and tubing selection of the system.

The muscle inlet area, $A_{m,i}$, is assumed to be the same as the initial cross sectional area of the muscle, $\pi r_0{}^2$, and A_{acc} is the cross-sectional area of the accumulator. $A_{m,i}$ and A_{acc} are used to related the volumetric flowrate into the muscle and into and out of the accumulator to the average velocity of the flow. Equation (9) is used to determine the pressure actually entering the muscle from the accumulator and the speed at which is does so..

2.4 Electric Motor and Pump Modeling

The hydraulic system described above uses a constant volume pump driven by a brushed DC-motor. Based on first principles, the following differential equations were used to model the electromechanical behavior of the motor as

$$\ddot{\theta} = \frac{k_e I - B_{motor}\dot{\theta} - \tau_p - \tau_{fric}}{J} \qquad (10)$$

$$\dot{I} = \frac{V_{motor} - k_b\dot{\theta} - IR}{L} \qquad (11)$$

$$I = \frac{\tau_p + B\dot{\theta}}{k_e} \qquad (12)$$

where $\dot{\theta}$ is the motor speed, V_{motor} is the applied voltage to the motor, L is the motor winding inductance, J is the motor's moment of inertia, k_b is the motor's back electromagnetic force constant, k_e is the motor's torque constant, and *R* is the motor's winding resistance. The motor and pump torque, τ_p, is related to the attached pump size as well as the accumulator pressure by

$$\tau_p = \frac{P_{acc} D}{2\pi} \tag{13}$$

and the motor speed and flow rate are related by

$$\dot{\theta} = \frac{\dot{V}_p}{D} \frac{2\pi}{rev} \tag{14}$$

where *D* is the volumetric displacement of the pump per revolution. The motor selected for use for the initial study is a 5W Maxon DC Brushed motor [9]. Its characteristics are included in **Table 2.**

Table 2. DC motor parameters.

Parameter	Value
No-load speed	9970 RPM
No Load Current	10.4 e -3 A
k_b	17.1e-3 Nm/A
k_e	17.1e-3 V-sec/radian
J	4.2 e-7 kg-m^2
R	13.8 Ohms
L	0.89e-3 H
V_{motor}	18 V

The motor characteristic curves along with the actual operation curves while operating with the system characteristics in **Tables 1, 2, and 3** are shown in **Figure 4** in section 3**.**

2.5 Combined System Model

The above system models were combined and applied to a simplified climbing robot design. It includes the robot itself of weight, W_{robot}, a McKibben muscle with previously defined parameters, a spring with constant K_{spring}, and a 'gripper' which provides a no-slip assumption for force transmission between the robot system and the climbing surface. Kinematics and mechanical advantages of various leg designs are not discussed in this study.

The equation of motion for this system for a given contraction of a single muscle during a step is given by

$$m\ddot{x} = F_m + T - B\dot{x} - k_{spring}x - W_{robot} \tag{15}$$

where *T* is the tension in the muscle braid required to maintain static equilibrium for cases in which muscle actuation force does not exceed the robot weight, such as prior to pressure being applied to a given muscle. As muscle actuation force, F_m, increases from zero when no pressure is applied to a value sufficient to induce motion, *T* decreases to maintain static equilibrium until motion is induced. *B* is an assumed damping coefficient and was selected to be the critical damping coefficient of the system based on observation the un-damped system model. A constant mechanical advantage of unity is assumed such that a change in muscle length of distance x is equivalent to a change in height of the robot of the same distance, x. As the model for muscle actuation is quasi-static, a true value for muscle damping in the dynamic case will need to be determined in future work.

Once the system state histories are determined, the system efficiency is calculated as

$$\eta_{sys} = \frac{\Delta PE_{robot}}{\int P_{motor}\, dt} \tag{16}$$

where instantaneous motor power input, P_{motor} is calculated as the constant operating voltage multiplied by the instantaneous motor current, and ΔPE_{robot} is the change in robot potential energy following a climbing operation.

3. RESULTS AND DISCUSSION

The combined system of equations (7), (10), (11), (12), and (15) can be solved via a numeric ODE solver in MATLAB. A display of various dynamic states through a five-step climbing sequence is shown in **Figure 3**. The robot parameters used for these calculations are shown in **Table 3** along with the muscle parameters from **Table 1** and the motor and pump parameters from **Table 2.** Figure 3a illustrates the contraction of each fluidic artificial muscle along with the acceleration of the robot as a whole with that contraction. pump starts and comes up to operating speed. This is shown in figure 4c by the current spike. As accumulator pressure cycles up and down, pump and motor torque cycle with it and motor current oscillates slightly which is shown as time goes beyond ~0.1 seconds in figure 4c..

A series of analyses were performed in order to determine the relationships between each system component. The initial study was performed with the conditions listed in **Table 3**, which were selected using reasonable

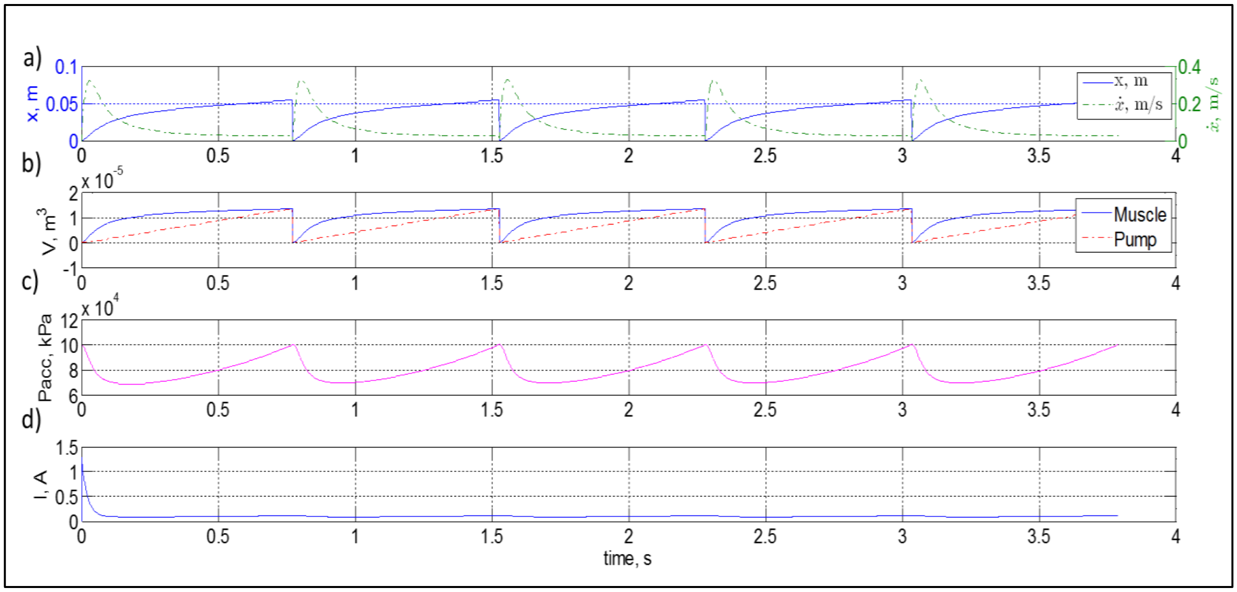

Fig 55 Time histories of robot dynamic variables during five step climbing sequence beginning from rest including, a) x and ẋ, b) Vm and Vp, c) Pacc, and d) motor current, I

Figure 3b and 3c show the interaction between the pump operation, the muscle contraction, and the pressure in the accumulator. As a muscle contracts during a given stride, V_m, increases—initially at a rate faster than the pump can refill the accumulator, resulting in P_{acc} dropping. As muscle contraction slows, as indicated by $\dot{x}$ decreasing, the pump is able to refill the accumulator and P_{acc} is restored. Once accumulator pressure is restored to its initial value, the operating valves are repositioned, draining the previously contracted muscle (and allowing it to be rest by the return spring) and the next muscle is actuated by accumulator pressure. During this cycle, the sizing constraints based on a previous study of FAM use in a climbing robot [7].

Table 3. Robot characteristics for initial study

Parameter	Value
m_{robot}	1 kg
k_{spring}	0.05 N/m/s
Total Accumulator Vol	6.1087 e -5 m^3
$V_{acc,i}$	50% Accum. Vol.
$P_{acc,i}$	99.9 kPa

First, it was noticed that operating speed of the motor had a large impact on the overall efficiency of the system. As can be seen in the blue curve in **Figure 4**, a change in motor speed from 980 rev/s to 1030 rev/s results in a drop in motor efficiency of ~22%. Operation at a speed greater than the optimal-efficiency-speed for the DC motor chosen, a 5 W Maxon DC Brushed motor [9], is shown to result in a rapid fall off in electrical to mechanical transduction efficiency. In order to control the motor efficiency, the accumulator pressure and pump displacements can be adjusted to find the optimal operating pump displacement for a given pressure. This is analogous to the pump-selection process used in large scale fluid power systems and plays a major part in system design for the climbing robot.

The heavy green curve in **Figure 4** shows the migration of the motor operating conditions during the process of the robot taking several steps. As can be seen in the efficiency plot, as pressure drops during operation, the lowered torque leads to an increased motor speed. By selecting an appropriate pump size, it is possible to ensure torque remains high enough that even during the low-end of operation the motor is operating to the left of the precipitous efficiency drop which occurs at greater than approximately 1000 revolutions per minute.

It was found that with a larger pressure drop (that is, the larger the change in V_{acc} relative to the initial value), a higher D allows the system to operate at a slightly higher torque for a given peak pressure. This maintained the operating speed range of the motor in a more efficient speed torque-speed range. However, for lower operating pressures and pressure drops, operating closer to the efficiency drop-point was actually more efficient the inefficient modes as it nears the no-load speed.

The most impactful observation is that, for a given muscle size, there is an optimal P_{init} and V_{init}; the relationship between pressure, volume, and efficiency is less clear-cut than was initially thought. As is noted in equation (2), the force of the muscle is directly proportional to the pressure applied and is also a function of the contraction of the muscle. As peak pressure rises, the muscle is able to contract farther, increasing the potential energy change. This also has two other effects. The increased contraction of the muscle creates a larger volume change in the muscle, and therefore a larger pressure drop in the accumulator. This increased pressure drop causes the pump, which is sized for maximum efficiency during operation, to run for a longer period of time in order to restore system pressure to its peak value.

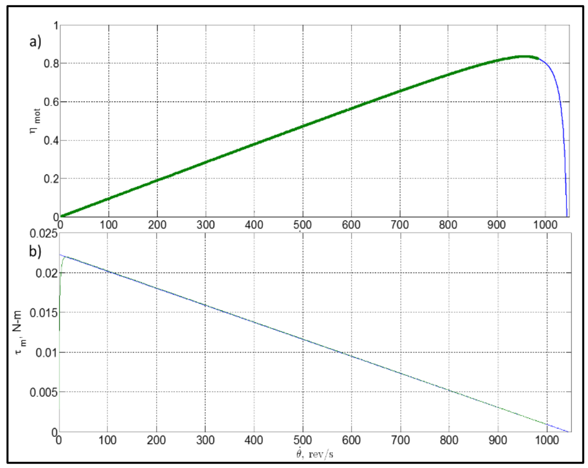

Fig 56 a) Motor efficiency and b) Motor torque as functions of motor speed for selected motor (thin blue line) overlaid with system operation curves (thick green line) with D = 0.093 mL.

As can be seen in **Figure 5**, which shows varying initial accumulator pressures and accumulator initial fill percentages, there is a minimum pressure for which muscle contraction will occur for a given muscle and robot-weight combination. Furthermore, this plot demonstrates that there is an optimal operating pressure for every accumulator fill percentage for a given robot weight. The accumulator size was the same for all calculations, the differences occur in the amount of air initially present in the accumulator. The other effect leading to the higher peak efficiency occurring at higher pressures is the increased robot weight due to the increased fluid volume in the accumulator (and therefore the system). This relationship is indicative of the non-linear relationship between volume change and force application at a given pressure.

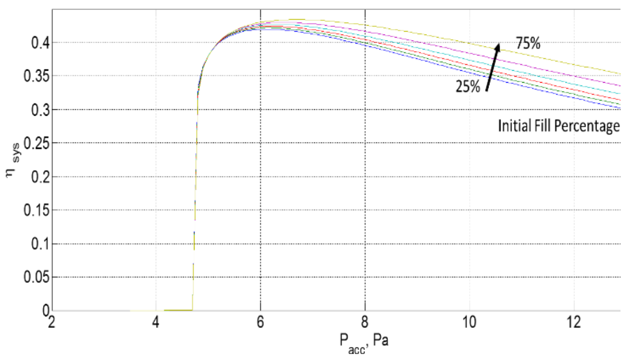

Fig 57 System efficiency variation over five strides with initial accumulator pressure and initial accumulator fill volumes from 25% water-filled to 75% water-filled

Next, we examine the effect of the number of strides taken by the robot on the system efficiency. Since the pump is continuously operating in this analysis, the efficiency increases asymptotically with the number of steps, with a limit of ~43% for the system analyzed here. As can be seen in **Figure 6**, the more steps taken for a given pressure-volume combination, the more efficient the system becomes. This is due to the high motor starting current relative to the fairly constant operating current.

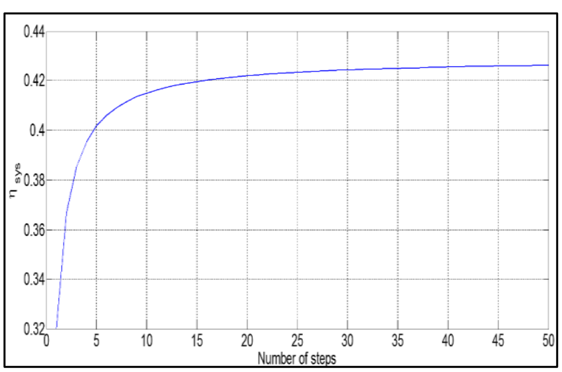

Fig. 58 System efficiency variation with number of strides taken

The sources of efficiency loss in our study are motor efficiency and muscle damping. While the motor is starting up, it is operating far below the peak operating efficiency speed and therefore, while the system operates near the optimal efficiency point for much of its operation, it still incurs losses during start-up. The other cause for the increased efficiency as weight of the robot increases is that, as mass goes up, the rate of acceleration for a given force input goes down, resulting in decreased velocity. Since damping is directly tied to velocity, the damping losses go down. The losses due to the assumed damping are substantial in this analysis and further study is required to determine their effect on FAM operation in practical application.

4. CONCLUSIONS

This paper has presented an operating system model of a light-weight climbing robot using fluidic artificial muscles as its motive force. The results gathered from the analysis of several parameters of the system emphasize how important proper component selection is to the efficiency of operation of a climbing robot of this sort. This occurs at every phase of design; robot size drives FAM selection and operating pressure; both of which are strong indicators of the proper motor and pump sizing. The motor and pump selection in turn determine accumulator refill time and thereby are the largest single input to efficiency of the system.

The intended function of the robot should be considered first and foremost in system selection and analysis at all ranges of operating conditions should be performed prior to part selection and manufacturing. A robot which is required to operate only at low pressures due to its light weight and long-term operation could have a smaller motor-pump combination and accumulator than a robot whose range of operation required it to carry and drop off large loads. By examining each facet of design it is possible to minimize inefficiencies and prolong operational time. While mechanical advantage was not analyzed in this study, the results of the study indicate that proper leg design and gait analysis should also be performed to ensure optimal operation for the greatest period of time.

REFERENCES

[1] Raibert, M., Blankespoor, K., Nelson, G., 2008, "BigDog, the Rough-Terrain Quadruped Robot," Proceedings of the 17th World Congress The International Federation of Automatic Control Anonymous pp. 10822-10823-10825.

[2] Nakagakubo, A., and Hirose, S., 1994, "Walking and Running of the Quadruped Wall-Climbing Robot," 1994 IEEE International COnference on Robotics and Automation, Anonymous **2,** pp. 1005-1006-1012.

[3] Provancher, W. R., Jensen-Segal, S. I., and Fehlberg, M. A., 2011, "ROCR: An Energy-Efficient Dynamic Wall-Climbing Robot," IEEE/ASME Transactions on Mechatronics, **16**(5) pp. 897-906.

[4] La Rosa, G., Messina, M., Muscato, G., 2002, "A Low-Cost Lightweight Climbing Robot for the Inspection of Vertical Surfaces," Mechatronics, **12**(1) pp. 71-96.

[5] Tiwari, R., Meller, M. A., Wajcs, K. B., 2012, "Hydraulic Artificial Muscles," Journal of Intelligent Material Systems and Structures, **23**(3) pp. 301-312.

[6] Tondu, B., 2012, "Modelling of the McKibben Artificial Muscle: A Review," Journal of Intelligent Material Systems and Structures, **23**(3) pp. 225-253.

[7] Bryant, M., Fitzgerald, J., Miller, S., 2014, " Climbing Robot Actuated by Meso-Hydraulic Artificial Muscles " Proceedings of SPIE: Active and Passive Smart Structures and Imtegrated Systems, Anonymous **SPIE: 9057,** .

[8] Meller, M. A., Bryant, M., and Garcia, E., 2014, "Reconsidering the McKibben Muscle: Energetics, Operating Fluid, and Bladder Material," Journal of Intelligent Material Systems and Structures, **25**(18) pp. 2276-2293.

[9] Maxon Motor, 2015, "Maxon Motor Company," **2015**(April/16) .

Bio-inspired passive variable recruitment of fluidic artificial muscles

Edward M. Chapman, and Matthew Bryant

Department of Mechanical and Aerospace Engineering, NC State University, Raleigh, NC, 27695, USA

E-mail: emchapma@ncsu.edu, mbryant@ncsu.edu

Abstract

This paper explores the modeling and analysis of the effect of minimum actuation pressure previously observed in literature. This minimum pressure is similar in kind to the minimum amplitude of the signal for muscle actuation seen in mammalian muscles. This minimum actuation, or "threshold" pressure is used a method of mechanically encoding the control of FAM engagement and the actuation efficiency of a group, or 'bundle' of muscles with differing threshold pressures is compared with a single muscle of equivalent force and strain. The results of this analysis indicate the efficacy of using this design and control method; it is advantageous in cases where a range of displacements and forces are necessary.

Keywords. Fluidic Artificial Muscle, McKibben Muscle, Hydraulic Artificial Muscle, Bio-Inspired, Efficiency.

1. INTRODUCTION

Fluidic artificial muscles (FAMs) were created by Joseph McKibben [1] as an upper limb assistive device for polio victims. FAMs are lightweight, inherently compliant, have high force-weight ratios, and do not require precision alignment in many applications [2]. When inflated, an elastic bladder expands into a helically braided sheath, causing a contractile force to be generated. This is biomimetic of mammalian muscles in that both FAMs and animal muscles are single acting and require antagonistic muscles to be dual acting.

Previous studies have modeled FAM contractile force output [3, 4] using idealized models and empirically derived correction factors to account for nonlinearities in experimental results. One study focused on the efficiency of an electrohydraulic system with FAM actuators and how showed the effect of FAM design parameters on the overall system efficiency. [5]. Bryant, et al. first proposed the use of FAMs bundled together and showed that there were efficiency gains to be had by only actuating sufficient FAMs to apply the force needed for the system [6]. These results were expanded by others, applying the use of servo-actuated control valves for FAM operation. Borrowing terminology from mammalian muscles again, groups of muscles actuated together are called 'motor units.' Using a single valve for each motor unit is called 'active variable recruitment' (AVR) and has advantages over using a single, larger FAM. This has been improved by continued improvements in control-schemes and; researchers have designed and characterized intelligent FAM online variable recruitment switching scheme [7] and experimentally showed online variable recruitment control and efficiency improvements in a robot arm using a recruitment logic state machine [8]. These studies show that when recruiting FAMs, it is more efficient to use smaller muscles when smaller output forces and displacements are required and to only engage more or larger FAMs when an increased force or displacement is necessary [9].

These AVR studies illustrate the efficiency gains possible through selective recruitment control in FAM actuation systems. But we wanted to further explore the bio-mimetic nature of FAMs and determine if there might be insight to be found in physically programming the orderly recruitment behavior in the FAM itself. In mammalian muscle recruitment, motor units with larger muscle fibers tend to have larger motor neurons; these larger motor neurons in turn have larger minimum amplitude of stimulation required for recruitment [10]**.** This is known as Hennemen's size principle and motor units are generally engaged from smallest to largest due to this principle. The activation is therefore regulated by a common signal from the central nervous system by the motor neurons and their associated axons [11]. The elasticity of FAM bladders can, depending on thickness and material, cause the FAM to exhibit a minimum pressure for actuation to occur seemingly emulating this size principle. Thicker or stiffer elastomeric bladder materials tend to require larger applied pressures before output force or significant contraction are generated [12]. We have observed this minimum pressure for actuation in many studies [3, 12, 13] and, in this research, explore whether this effect can be made use of in such a way as to increase actuator efficiency. This minimum actuation pressure, or 'threshold pressure,' P_{th}, has also been called 'deadband pressure' and is defined as the minimum pressure required to overcome radial stresses and apply an axial, tensile force [12] [13]. This threshold pressure has generally been considered a loss, since it prevents working fluid from applying force to the braid and thereby lowers the work done by the FAM. This study presents a method by which the threshold pressure effect can be used to create a simplified passive variable recruitment (PVR) control scheme which uses only a single throttle valve to control the actuation of multiple FAM motor units.

We first discuss the modelling of fluidic artificial muscles and discusses threshold pressure, including some design challenges involved in grouping muscles with different threshold pressures and elastic properties in parallel and potential solutions to these challenges. It then compares PVR bundles with a single equivalent motor unit (SEMU) and concludes with a comparative efficiency analysis.

2. FLUIDIC ARTIFICIAL MUSCLE MODELING

Idealized FAM models begin with the virtual work model and setting

$$Fdx = PdV \tag{1}$$

where P is the pressure applied to the muscle, F is the tensile actuation force applied by the muscle, dV is the change in the volume of the muscle and dx is the linear change in length of the muscle along its center-line. Idealized muscle geometry has been well established by Tondu, et al. [2] and others as

$$\frac{l}{l_0} = \frac{\cos\alpha}{\cos\alpha_0}\text{, and} \tag{2}$$

$$\frac{r}{r_0} = \frac{\sin\alpha}{\sin\alpha_0} \tag{3}$$

where l is the FAM length, r is the FAM radius, and α is the braid angle of the fiber sheath. The initial values of these parameters are designated as l_0, r_0, *and* α_0. By performing a series of geometric substitutions, the volume of a muscle, V_m, in terms of strain, ε, and initial construction characteristics is

$$V_m = \pi l_0 r_0^{\,2}\,\frac{(1-\varepsilon)-(1-\varepsilon)^3\cos^2\alpha_0}{\sin^2\alpha_0}\,. \tag{4}$$

The change in volume as strain changes is shown to be

$$\frac{dV_m}{d\varepsilon} = \pi l_o r_0^{\,2}\,\frac{(-1)+3(1-\varepsilon)^2\cos^2\alpha_0}{\sin^2\alpha_0}\,. \tag{5}$$

Therfore, force as a function of strain is

$$F_{m,ideal} = P_{app}\pi R_0^{\,2}\left[a(1-\varepsilon)^2 - b\right] \tag{6}$$

where P_{app} is applied pressure and

$$a = \frac{3}{tan^2\alpha_0}\text{, and} \tag{7}$$

$$b = \frac{1}{sin^2\alpha_0}\,. \tag{8}$$

This model is effective at predicting blocked force, but shows experimental mismatches in many cases. For this reason, Tondu, et al. and Meller, et al. [3, 4] corrected for these losses using empirical blocked force and free-strain correction factors, κ_F and κ_ε. The ideal model also doesn't take into account the 'threshold pressure,' P_{th}, which is likewise experimentally determined. We include this combination of parameters into the relationship

$$F_m = P_{eff} \kappa_F \pi r_0^{\,2} \left[a\left(1-\kappa_\varepsilon \varepsilon\right)^2 - b \right] \tag{9}$$

where P_{eff} is the pressure transmitted to the braid above threshold pressure, defined as

$$P_{eff} = P_{app} - P_{th}, \tag{10}$$

3. PASSIVE VARIABLE RECRUITMENT

As discussed previously, FAM threshold pressure through elastic energy storage is normally considered a loss, but by learning to utilize difference in threshold pressure [3], we can apply the mammalian muscle principle of orderly recruitment to the actuation of FAMs in a way which actually increases overall actuation efficiency. Doing so allows us to generate simultaneous advantages in reducing control valves and simplifying the control algorithm. We can combine a so-called, "low threshold pressure muscle" with a "high threshold pressure muscle" in a bundle and compare them with single muscle which has the same peak output force and free strain, called a "Single Equivalent Motor Unit" to determine the actuation efficiency gains. The hydraulic and actuation set up of both a SEMU and a PVR bundle are shown in figure 1.

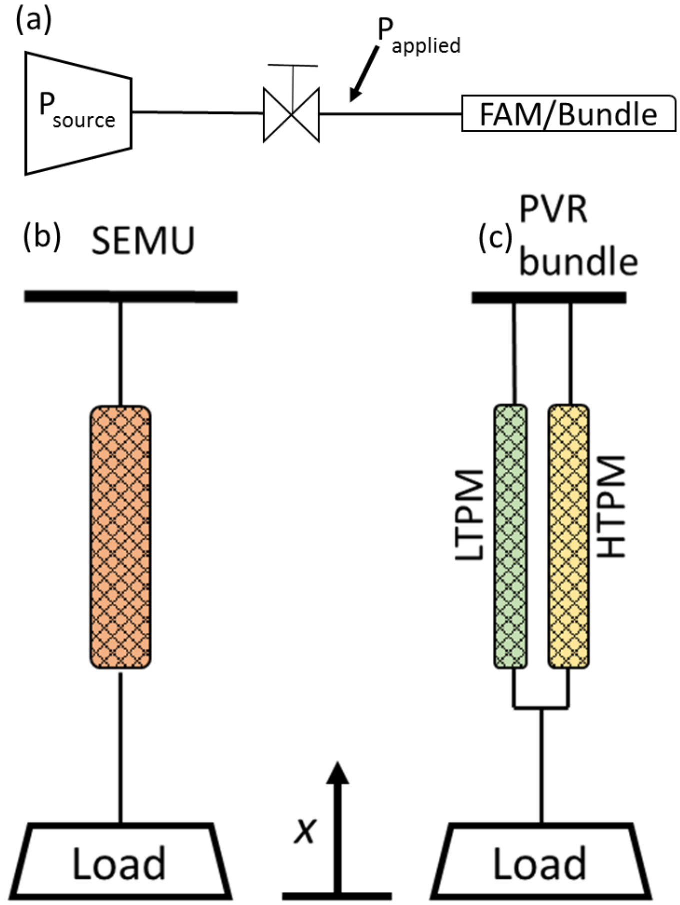

Figure 59: a) Hydraulic system and constant force and actuation setup of b) SEMU and c) PVR bundle

In order to compare a bundle made up two or more muscles to a SEMU, we define a SEMU as having the same blocked force and free strain as the PVR Bundle. Since blocked force is a function exclusively of initial braid radius and effective pressure, we can calculate the radius of the SEMU using

$$(P_{source} - P_{th,SEMU}) r_{0,SEMU}^{\;2} = (P_{source} - P_{th,\mathrm{LTPM}}) r_{0,\mathrm{LTPM}}^{\;2} + (P_{source} - P_{th,\mathrm{HTPM}}) r_{0,\mathrm{HTPM}}^{\;2} \tag{11}$$

when the correction factors are assumed to be unity. The actuation efficiency of the SEMU and the PVR Bundle were defined as

$$\eta_{SEMU} = \frac{\int F_{SEMU}\,dx}{P_{source}\int dV} \tag{12}$$

$$\eta_{bundle} = \frac{\int F_{bundle}\,dx}{P_{source}\int dV} \tag{13}$$

where P_{source} is the highest system pressure available, here assumed to be 500 kPa, and F_{bundle} and F_{SEMU} are the stroke-and-pressure dependent output force of the PVR bundle and the SEMU, respectively.

4. PVR-SEMU COMPARISON

Having established a method for setting equivalent operating characteristics and defined efficiency, we can now compare SEMU's and PVR bundles composed of one LTPM and one HTPM. The parameters of the FAMs considered for this analysis are shown in Table 1**.**

Table 1: PVR and SEMU FAM construction characteristics

	LTPM	*HTPM*	*SEMU*
l_0 *(m)*	0.08	0.08	0.08
$r_{0,braid}$ *(m)*	0.005	0.005	0.0061
P_{th} *(kPa)*	0	250	0
α_0 *(deg)*	28	28	28

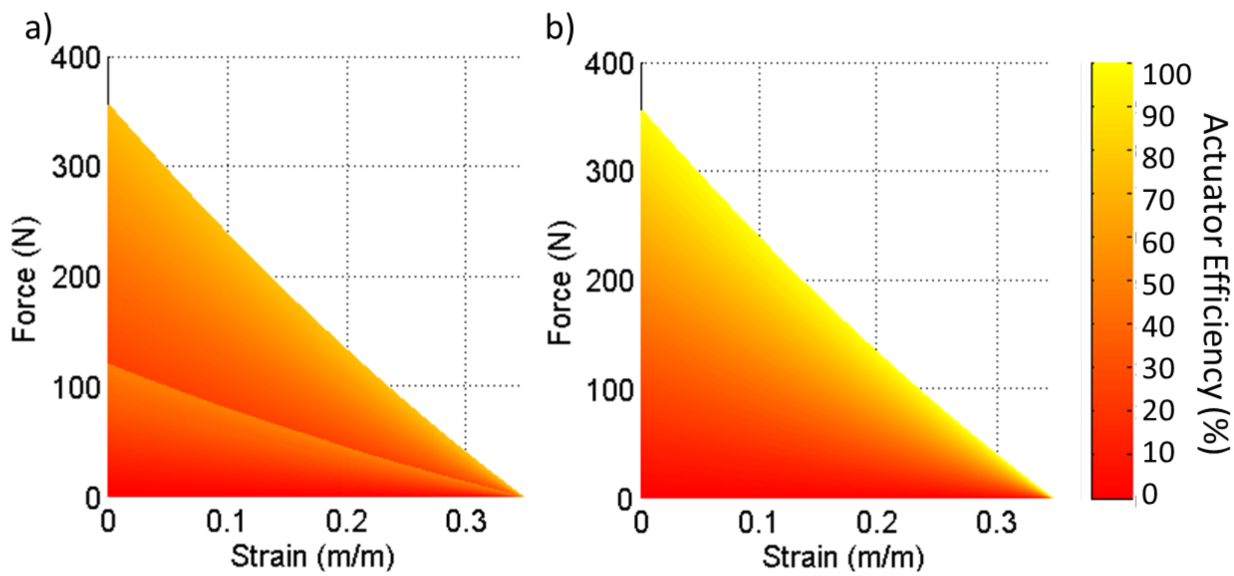

Figure 60: Muscle Efficiency for the Force-Stroke characteristics of a) a PVR Bundle with two muscles and b) a SEMU with a peak pressure of 500 kPa. These plots show the equal blocked force and free stroke, as defined. Note the area of decreased efficiency in the PVR bundle corresponding to the area between $P_{th,\,HTPM}$ and P_{lag}

As shown in figure 2, the PVR bundle operates in the low-force portion of the force-strain space with a higher efficiency than the SEMU. However, as applied pressure goes above the threshold pressure the HTPM begins to consume working fluid and the efficiency of the PVR bundle decreases. These results suggest that for lightly loaded (less than ~100 N) primary modes of operation, the PVR bundle is more efficient. In the event that the system were required to operate in a given region for 100% of the time, it stands to reason that a variable recruitment bundle should not be selected and that the FAM chosen should be selected for the force and strain required.

5. PVR BUNDLES AND SEMU ACTUATION WITH A CONSTANT LOAD

In order to further compare actuation efficiencies of a PVR bundle to a SEMU we simulated their activation through 15% strain at for three different loads. Those loads selected correlated to 10%, 20%, and 40% of the peak output force of the bundle. These loads are illustrated on a force-strain plot in figure 3.

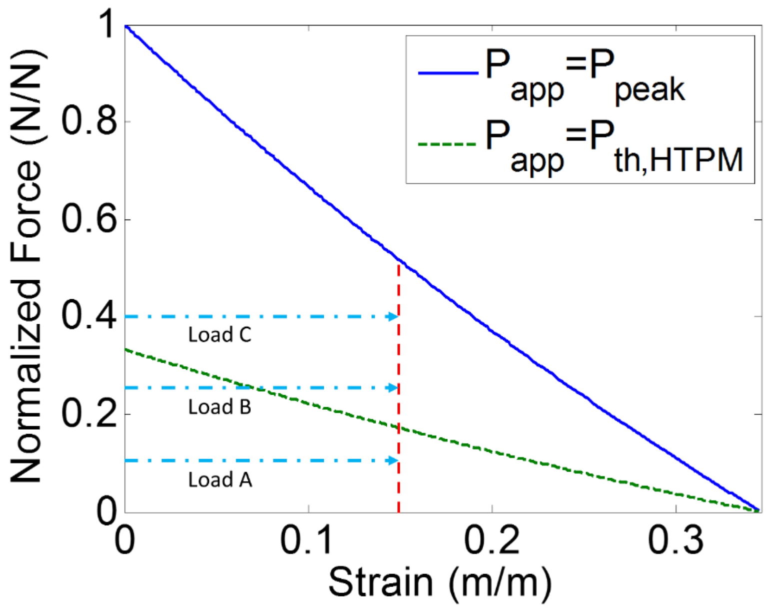

Figure 61: Force output of PVR bundle when applied pressure is source pressure, HTPMU threshold pressure, and lag pressure

Plots of the required applied pressure, threshold pressure, and working fluid volume consumption of both the PVR bundle and the SEMU were generated for each of these loads. They are shown in figure 4**.** As can be seen, at the lowest load (Load A), the bundle never engages the HTPM and, therefore, the fluid volume consumption is always lower. At the highest load (Load C), the HTPM is always engaged and, therefore the fluid volume consumption is always higher. At the moderate load (Load B), the LTPM bears the load until the necessary applied pressure surpasses threshold pressure of the HTPM, at which point the PVR bundle working fluid volume consumption increases as the HTPM begins to contribute to the actuation force of the bundle.

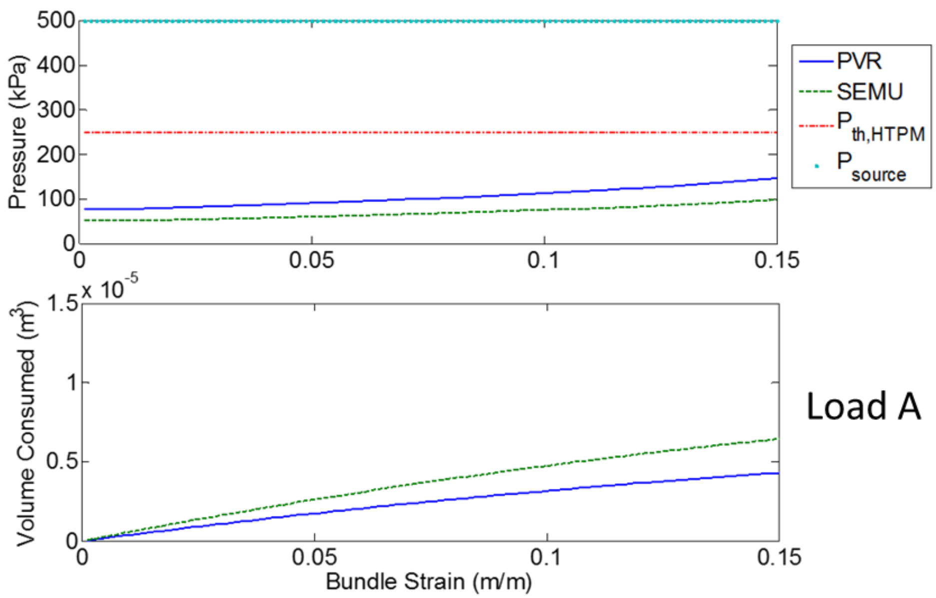

Pressure (kPa)
PVR
SEMU
$P_{th,HTPM}$
P_{source}
Volume Consumed (m^3)
x 10^{-5}
Bundle Strain (m/m)

Load A

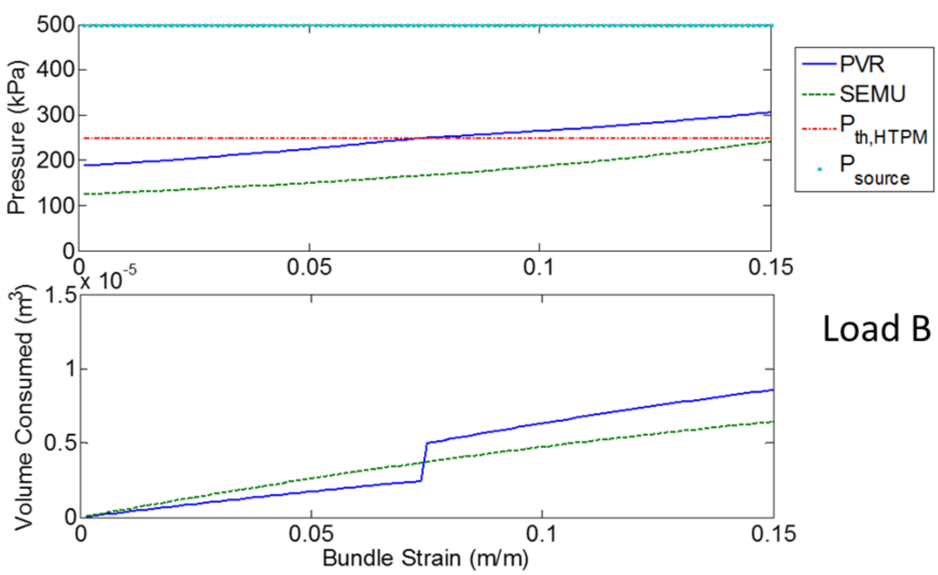

Pressure (kPa)
PVR
SEMU
$P_{th,HTPM}$
P_{source}
Volume Consumed (m^3)
x 10^{-5}
Bundle Strain (m/m)

Load B

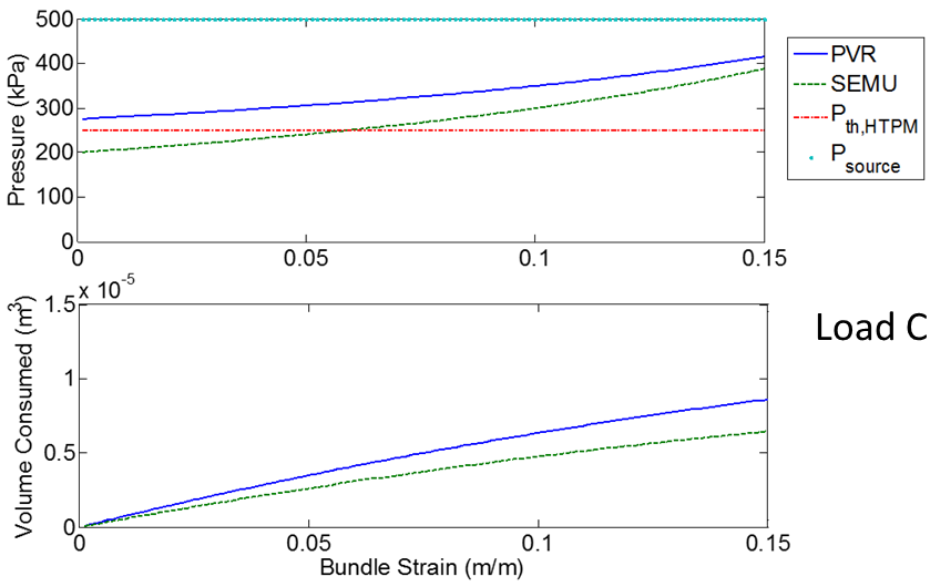

Figure 62: Applied pressure and volume consumed by the PVR bundle and SEMU for Load A, Load B, and Load C. The SEMU always consumes more working fluid at the heaviest load and the bundle consumes more at the heaviest. When a moderate load is require, the SEMU consumes more working fluid below threshold pressure of the HTPM and more at above.

6. CONCLUSIONS

A preliminary comparison of PVR Bundles and their SEMU counterparts indicates that employing PVR bundles in certain scenarios may be beneficial. Such scenarios include those in which the normal operation of the system actuation would be in the low-force, low-strain regime of the force-strain space but which include some excursions from this regime into either high-force or high-strain regimes. It is of note that, should the operating regime be 100% in any given portion of the force-strain regime, it would be beneficial to design a single FAM such that it exactly meets the needs of the operation. However, as shown here, there are efficiency gains to be had when the system operates in more than one regime. We have presented a preliminary analysis of the passive variable recruitment methodology and its potential improvement to control methodology and hydraulic system simplification. Further analysis of the details of the design consideration of these biomimetic actuators using this bio-inspired control methodology bears consideration.

REFERENCES

[1] Anonymous 1958, "Paralyzed Given Help by Artificial Muscle: Device Developed with March of Dimes Aid Permits Quadruplegic to Feed Himself," Los Angeles Times (1923-Current File), pp. B8.

[2] Tondu, B., 2012, "Modelling of the McKibben Artificial Muscle: A Review," Journal of Intelligent Material Systems and Structures, **23**(3) pp. 225-253.

[3] Meller, M. A., Bryant, M., and Garcia, E., 2014, "Reconsidering the McKibben Muscle: Energetics, Operating Fluid, and Bladder Material," Journal of Intelligent Material Systems and Structures, **25**(18) pp. 2276-2293.

[4] Tondu, B., and Lopez, P., 2000, "Modeling and Control of McKibben Artificial Muscle Robot Actuators," Ieee Control Systems Magazine, **20**(2) pp. 15-38.

[5] Chapman, E. M., Jenkins, T. E., and Bryant, M., 2017, "Modeling and Analysis of a Meso-Hydraulic Climbing Robot with Artificial Muscle Actuation," Bioinspiration & Biomimetics, **12**(6) pp. 066010.

[6] Bryant, M., Meller, M. A., and Garcia, E., 2014, "Variable Recruitment Fluidic Artificial Muscles: Modeling and Experiments," Smart Materials and Structures, **23**(7) pp. 1-12.

[7] Jenkins, T. E., Chapman, E. M., and Bryant, M., 2016, "Control approach development for variable recruitment artificial muscles," SPIE Smart Structures and Materials Nondestructive Evaluation and Health Monitoring, Anonymous International Society for Optics and Photonics, pp. 979911-979911-10.

[8] Meller, M., Chipka, J., Volkov, A., 2016, "Improving Actuation Efficiency through Variable Recruitment Hydraulic McKibben Muscles: Modeling, Orderly Recruitment Control, and Experiments," Bioinspiration & Biomimetics, **11**(6) pp. 065004.

[9] Robinson, R. M., Kothera, C. S., and Wereley, N. M., 2015, "Variable Recruitment Testing of Pneumatic Artificial Muscles for Robotic Manipulators," IEEE/ASME Transactions on Mechatronics, **20**(4) pp. 1642-1652.

[10] Henneman, E., Somjen, G., and Carpenter, D. O., 1965, "Excitability and Inhibitability of Motoneurons of Different Sizes," Journal of Neurophysiology, **28**(3) pp. 599-620.

[11] Henneman, E., Somjen, G., and Carpenter, D. O., 1965, "Functional Significance of Cell Size in Spinal Motoneurons," J Neurophysiol, **28**(3) pp. 560-580.

[12] Pillsbury, T., Kothera, C., and Wereley, N., 2015, "Effect of Bladder Wall Thickness on Miniature Pneumatic Artificial Muscle Performance," Bioinspiration & Biomimetics, **10**(5) pp. 055006.

[13] Sangian, D., Naficy, S., Spinks, G. M., 2015, "The Effect of Geometry and Material Properties on the Performance of a Small Hydraulic McKibben Muscle System," Sensors and Actuators A: Physical, **234**(Supplement C) pp. 150-157.

Appendix C: Strain limitation studies performed in climbing robot analysis

Effects of Prescribed Contraction Limit and Initial Braid Angle on System Performance

In all the previous case studies, muscle contraction in each step is allowed to increase until either the full range of motion of the leg is reached, or the robot comes to an equilibrium position. This sets the robot stride length to the maximum achievable value for the given parameters. In this section, we consider the effects of prescribing a step-length by intentionally limiting muscle contraction. Initial braid angle is swept from 25-40 degrees for prescribed muscle contraction limits from 5-14% strain. The resultant effects on system efficiency and average velocity are shown in the figure below.

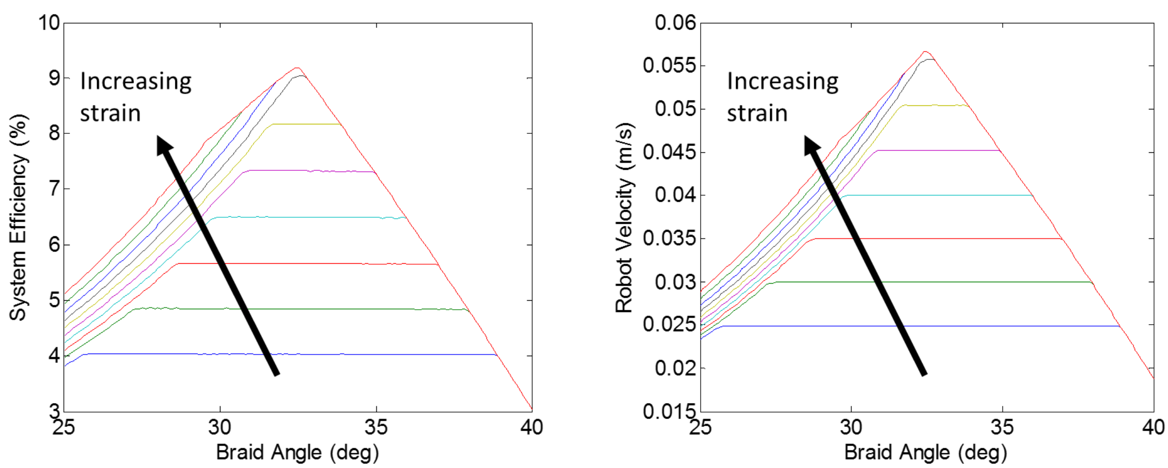

Efficiency and velocity as a function of braid angle for allowable strains from 5-14%

As demonstrated by these outputs, limitations on strain cause the most negative effect at optimal braid angles. When the braid is allowed to contract to 14%, the efficiency is maximized at 9.2% while if limited to 5% strain allowed efficiency peaks at 4.03%, representing a 56.2% change in system efficiency at peak values. At smaller braid angles, this percent change is smaller only 26.3% drop from 5.16% at near full contraction to 3.8% at the minimum contraction studied, where strain is maximized in comparison to higher braid angles. At the highest braid angles, there is no difference between system efficiencies; this is because the FAMs are underpowered and don't contract fully under the particular robot mass considered. Allowing FAMs to contract more and, thereby, do more work, generates the highest system efficiencies and velocities for any FAM with sufficient braid angle. At sufficiently low braid angles, the output force is such that the strain limitations are less impactful—FAMs generate their largest output forces at blocked force. Significantly, limiting strain limits the braid efficiency and velocity of system operation are limited to the value associated with that contraction. This implies that selecting a FAM which can fully contract in the mechanical space allotted it is advantageous in system design.

Effects of Prescribed Contraction Limit and Initial Braid Radius on System Performance

Again, as with braid angle, braid radius is swept through its range (2.5-5 mm) for a range of mechanical strain limitations from 5-14%. The efficiency and velocity outputs are shown in the figure below.

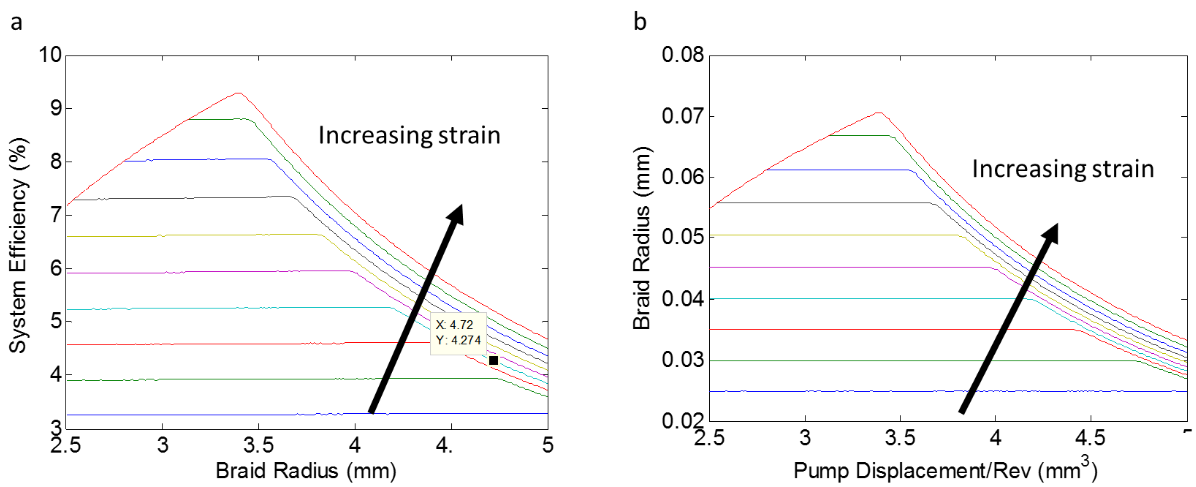

Braid radius vs efficiency and velocity for a variety of allowable strains

As with the braid angle sweep, the effect of limiting strain is least effective in the highest force output ranges; here the highest braid radii. When allowing the highest contraction, peak efficiency is 9.29% and occurs at a braid radius of 3.4mm while the highest efficiency shown for the 5% strain is 3.36—a 63.8% change from the peak available efficiency at full contraction. As with the braid angle study, underpowered FAMs fail to contract to the mechanically limited strain allowed and have the same efficiency and velocity as the muscles which have a larger strains allowance as can be seen in the figure above, At muscle radii which can provide sufficient output force to reach their mechanical strain limitations, there is an upper limit to efficiency and velocity, based on the fluid volume consumption and output force. At large braid radii, the accumulator refill time becomes limiting and prevents high velocities and efficiencies. This confirms the previous assertion that a FAM should be sized and selected such that full contraction is possible without excess loss from over-sizing

Appendix D: Analysis of Passive Variable Recruitment as part of a fully coupled electrohydraulic system

Passive variable recruitment (PVR) muscle bundles were shown in Chapter III to be advantageous over single equivalent motor units in scenarios in which the operational requirements of the bundle were normally in the low-load, low-stroke regime with occasional dalliances into the higher load or stroke regimes. However, their increased volume consumption once the HTPMU is engaged over either SEMU's or AVR bundles make them less advantageous once the full system is considered. Coupling this with little or no advantage of AVR bundles when coupled to either a continuously or intermittently operating pump show that PVR bundles are less advantageous in terms of both force and flow bandwidth limitations. Figure D-1 shows the bandwidth-efficiency plots for an AVR bundle compared to a PVR bundle and the clear advantage in both performance and efficiency of the AVR bundle of the PVR bundle. Figures D-2 and D-3 are the simulated system performance plots for both the continuous and intermittent pump operation cases.

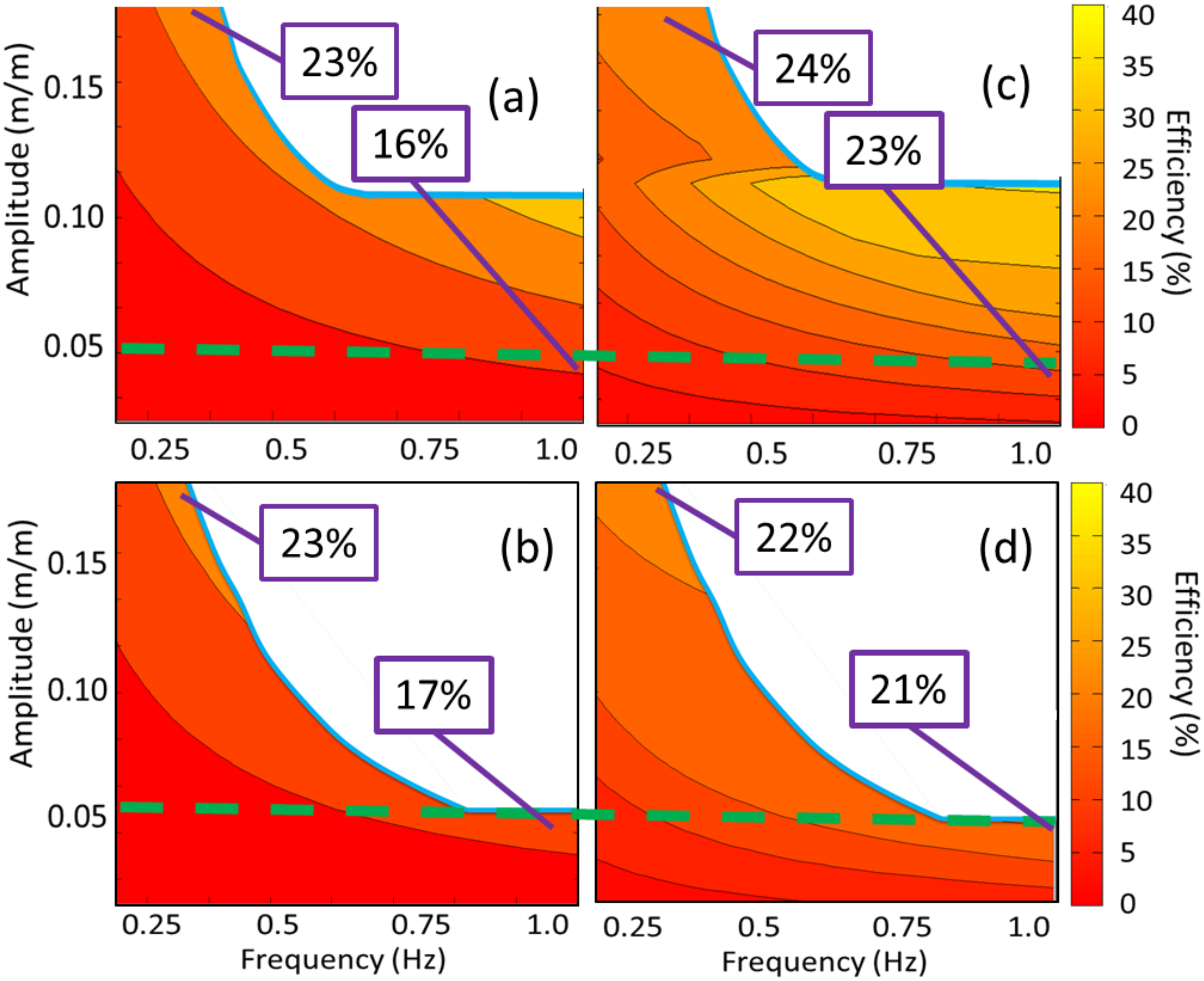

Figure D-1: Bandwidth and efficiency plots for an AVR bundle (a and c) and a PVR bundle (b and d) for both continuous (a and c) and intermittent (b and d) pump operation. Green dashed line represents engagement threshold for the PVR bundle. Labeled efficiencies are the highest efficiencies for the PVR bundles and the efficiencies at the same points for the AVR bundles. Note that the AVR bundles have a more robust bandwidth as well as higher operating frequencies for these bandwidths.

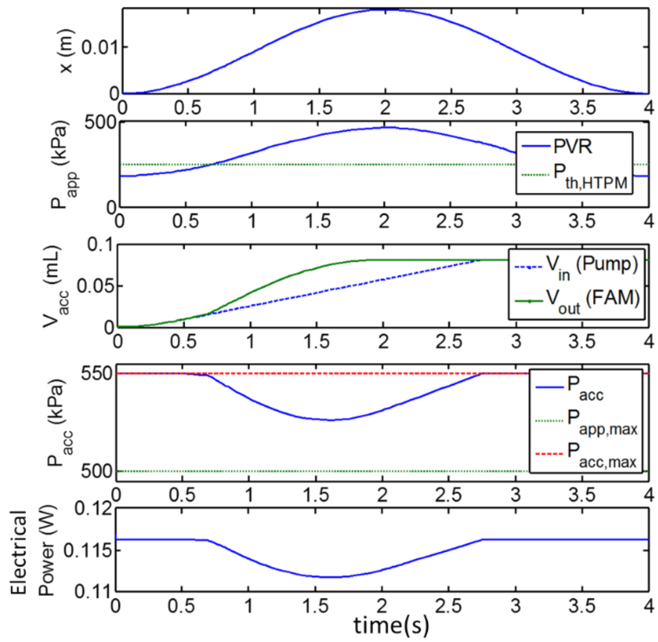

Figure D-2: System response to prescribed path with frequency = 0.25 Hz, x_{max} = 0.018 m, and mg/F_{bl} = 0.24 for PVR with continuous pump operation.

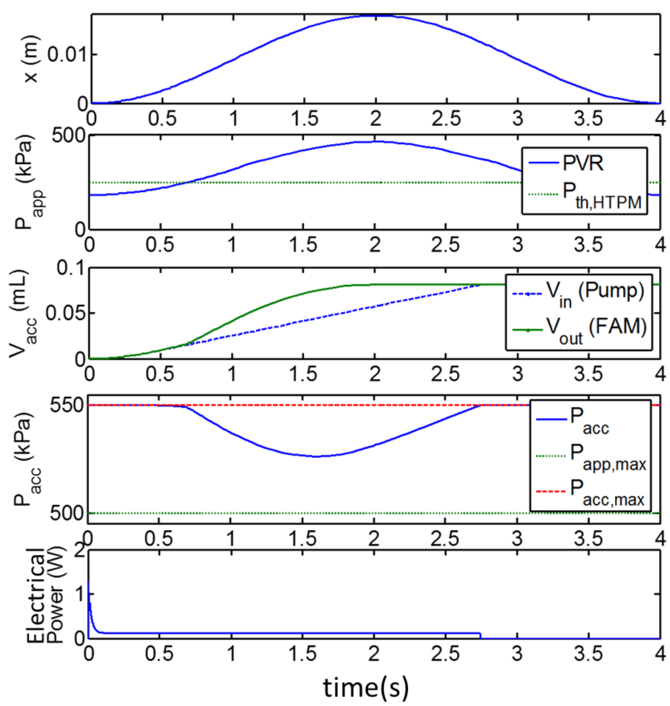

Figure D-3: System response to prescribed path with frequency = 0.25 Hz, x_{max} = 0.018 m, and mg/F_{bl} = 0.24 for PVR with intermittent pump operation.